implementation and study of the impact of membrane viscoelasticity on the deformability of red blood cells

Pascal Matteoli

THÈSE POUR OBTENIR LE GRADE DE DOCTEUR
DE L'UNIVERSITE DE MONTPELLIER

En Mathématiques et Modélisation

École doctorale : Information, Structures, Systèmes

Unité de recherche : Institut Montpelliérain Alexander Grothendieck

Implémentation et étude de l'impact de la viscoelasticité de membrane sur la déformabilité des globules rouges

Présentée par Pascal Matteoli

Le 06/12/2022

Sous la direction de Simon Mendez et Franck Nicoud

Devant le jury composé de

Marc Léonetti	Directeur de recherche CNRS, CINaM, Aix-Marseille Université	Rapporteur
Anne-Virginie Salsac	Directrice de recherche CNRS, BMBI, Université de Technologie de Compiegne	Rapporteur
José-Maria Fullana	Professeur des Universités, ∂'Alembert, Université de la Sorbonne	Président du jury
Manouk Abkarian	Directeur de recherche CNRS, CBS, Université de Montpellier	Examinateur
Simon Mendez	Chargé de recherche CNRS, IMAG, Université de Montpellier	Directeur
Franck Nicoud	Professeur des Universités, IMAG, Université de Montpellier	Co-directeur

UNIVERSITÉ DE MONTPELLIER

Remerciements

Quand on y pense, il n'est pas courant dans la vie d'avoir un moment dédié aux remerciements de ses proches. Je compte donc bien profiter de cette opportunité.

Je remercie d'abord les membres du jury pour le temps passé à évaluer ce travail, ainsi que pour leurs retours et leurs bienveillances. Je voudrai ensuite remercier mes directeurs de thèse pour leur accompagnement tout le long de ce travail. J'aurais un millier d'anecdotes à raconter, mais je les résumerais en disant qu'on s'est quand même bien marrés. Merci pour tout.

J'en profite également pour remercier quelques personnes qui m'ont inspiré et inculqué des leçons humaines qui ont façonné ma vision du monde aujourd'hui et qui me donne espoir. Donc Simon, Franck, M.Ryaux et M.Chrysochoos, merci pour tout.

Ensuite naturellement, mes camarades du laboratoire. Je commencerai donc par les membres de l'équipe YALES2BIO aka "la team sang" ou encore "le granini" pour les intimes. Un groupuscule d'énergumènes peu recommandable si vous voulez mon avis, qui ont eu la gentillesse de m'intégrer pour le meilleur et pour le pire. Je vous dois quelques remerciements. Tout d'abord, le "bureau du haut", à savoir à mon arrivé Dorian, Pierre et Thomas. Combien de fois j'ai toqué à votre porte pour vous dire "et les gars, j'ai une question..." ? Pour tout ça je vous en remercie. D'autres victimes de ces harcèlements sont Gautier et Rodrigo. Je vous ai tellement pourri vos fins de thèses respectives. J'espère que vous ne m'en tenez pas rigueur.
Il y a aussi Christophe et Julien, de véritables légendes du labo que j'ai eu la chance de côtoyer. En effet, avant de les rencontrer, j'en avais entendu parler sous le nom "du cœur de Christophe" et "du mec qui a le titre d'article le plus classe de l'histoire". Tant de graninis et de discussions à rallonge. Merci pour tout les gars. Le temps passe, et la relève du granini est déjà là en la présence de Bart et Morgane. J'espère avoir pu dispenser un peu de la "sagesse" que m'avaient inculqué mes pères. En tout cas sachez que votre soutient a été pour moi très important,

et mon passage dans votre bureau sur la fin pour débriefer, une véritable bouffée d'air frais. Merci.
Qu'il est mignon ! Il pensait que je l'avais oublié ! Non Alain, t'inquiètes pas. Déjà, que les choses soient bien claires, je t'ai battu au ping pong. C'est maintenant écrit noir sur blanc. T'as été mon gars mec, un modèle. J'ai trop de blagues tu vois, je ne pourrai pas toutes les mettre. Donc je trouve approprié, à l'instar de Simon et Franck, de synthétiser notre aventure par : on s'est bien marré. Quand tu veux pour la revanche. De l'amour mec, beaucoup.

Qu'aurait été cette aventure sans monGars (attaché, avec un G), Monsieur Robert ! Merci pour tout mec, pour tous les passages au bureau avec Abdoul' et Gwennael et tous ces bons moments.
Zaïnouba ! On a réussi ! On aura bien rigolé quand même, je n'aurais qu'une chose à dire pour résumer tous ces : sa7a ! Un grand merci aux Mamans du labo aussi, à savoir Radia et Thiziri ! Comme disait Zaïneb, combien de fois vous êtes venu pour transformer le bureau en café ? Merci pour tous ces bons moments. Nathan. Je sais que tu vis comme un échec de pas avoir pu obtenir un sponsor d'Ovomaltine. Je conserve précieusement ton rubicube de la carte de NYC. Merci pour toute nos petites discussions quand je passais t'empêcher de trop travailler. J'en oublies bien sûr, tant l'IMAG m'a bien accueilli. Donc de Julien à Tom en passant par Alan et autre GodinT, merci à tous d'avoir été là. J'adresse un remerciement particulier pour le personnel administratif qui, en plus de m'avoir accompagné dans toutes les démarches faisant partie du parcours classique du doctorant, m'a aussi tellement soutenu. Même au plus mal, vous aviez toujours le petit mot qui me faisait avoir le sourire. Donc un grand merci Nathalie, Bernadette, Brigitte et enfin Carmela.

J'aimerai également remercier les nombreuses personnes, hors laboratoire, qui m'ont soutenu durant ces années de thèse. Et comment ne pas commencer par Julien, le mec avec qui on a trop de points communs dans nos parcours à tel point que c'est flippant, aka "mon ami". Pour le coup toi t'as tout vécu avec moi, les moments les plus durs, t'étais la première personne que j'appelais. Tu m'as relevé dans les pires moments, tout ça pour qu'on ai un jour l'opportunité de finir cette carrière à FIFA. Merci mec.
Qu'aurait été ma thèse sans ce "mec qui fait du théatre", Félix. Pour les gens qui ne savent pas, cette personne a réalisé un court-métrage nommé "Bronchite", à

voir vraiment. Tu sais que j'ai trop de chose à dire mais pas la place de le faire. T'as toujours été là, au point de devenir mon colloc' durant le confinement et mon cobureau durant la dernière ligne droite. Trop d'amour sur toi pour le traduire de manière synthétique. Merci copain.
J'ai hésité à pas mettre Cyril dans mes remerciements. Il ne m'aurait jamais mis lui, il aurait remercié personne, en bon ingras qu'il est. Mais bon, Déjà qu'on a un groupe de discussion qu'avec Tim et Ana, après il va être bougon. Donc Merci camarade. De même Tim, t'as pas fait de remerciements quand t'as eu ton CAPEPS. Pourtant j'ai été le premier à te le dire (le plus gros spoil de l'histoire), j'aurai mérité un petit merci donc bon. Mais au final je vais te remercier, ne serait-ce que parce que les Bucks ont été champion avant les C's. Un énorme merci également à Marie et Ana. J'aurai pu vous définir comme les compagnes des deux énergumènes précédemment mentionnées, mais ce serait réducteur tant vous avez pris de la place dans ma vie. Vous êtes essentiel au bon déroulement de nos week-end de moins en moins productifs. C'est pourquoi je voulais vous dire, merci pour tout les amies.

Paragraphe obligé dédié aux personnes qui m'ont accompagné toute ma vie. Vous avez fait de moi celui que je suis aujourd'hui, je vous dois tellement mes yougos. Du coup je voulais vous offrir ce que j'ai fait de mieux durant mes études, et c'est cette thèse. Je n'ai rien de mieux. C'est trop important pour moi que vos noms accompagnent cette fin de parcours. Axel, Chrys, Dylan, Rachid, Steeven, Mota, Yanis et Zak. Je vous remercie pour tout. On est ensemble depuis le tout début, et je sais qu'on sera ensemble jusqu'à la toute fin. Je vous aime mes frérots.

J'aimerai remercier également ma famille, mes parents, mes deux frangins, mes grands-parents qui me parlait dès qu'ils entendaient parler de globule rouge à la télé ou à la radio. C'est évident que vous avez toujours été là, et je ne saurai jamais assez-vous remercier.
Un grand merci également à ma belle-famille au complet qui a été là pour me soutenir, allant jusqu'à être présent le jour j. Merci beaucoup.

Comment ne pas finir avec la personne qui a encore plus pleuré pour cette thèse que moi. Celle qui m'a accompagné dans le plus dur, celle qui partage ma vie, Camille. Merci de m'avoir supporté pendant cette épreuve. Tu sais à quel point cela a été dur. Tu m'as toujours relevé. C'est grâce à toi tout ça, je n'aurai pas réussi sans toi. Pour tout ça je te remercie. Longue vie à nous ma chérie.

"PPCQA"

André Chrysochoos

Résumé

Les globules rouges (GR dans ce résumé ou RBC en anglais, pour Red Blood Cell) sont les cellules les plus nombreuses dans le sang des vertébrés [151]. Dans le cas particulier du sang humain, les GRs représentent environ 45% du volume sanguin chez l'homme et 35-40% du volume sanguin chez la femme.
Dans le sang, les cellules sont en suspension dans le plasma, qui occupe la majeure partie du volume restant. Le plasma est principalement composé d'eau (à approximativement 90%) et contient jusqu'à 10% de protéines, et d'autres molécules jusqu'à 1 ou 2%. Enfin, environ 1% du volume sanguin est occupé par d'autres cellules sanguines, les globules blancs et les plaquettes.

Le volume sanguin moyen pour un adulte est d'environ 5 L. A raison d'environ 50 milliards de GRs par litre de sang, le nombre de GRs est d'approximativement 25×10^{12} chez l'adulte, ce qui fait du globule rouge la cellule la plus présente (de l'ordre de 80-90%) dans l'organisme.

Un GR sain a la forme d'un discocyte (Fig. 1). C'est la forme au repos du GR, *ie*

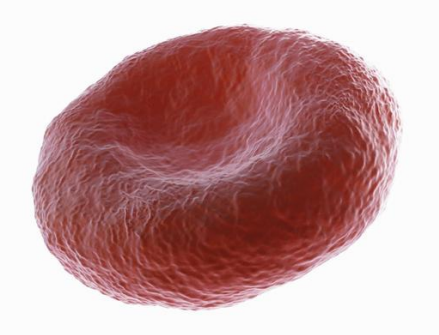

Figure 1: Un globule rouge dans sa forme en discocyte. Crédit : Science Picture Co Collection Mix: Subjects Getty Images.

lorsque la cellule sanguine n'est pas sous flux. Il s'agit typiquement d'une forme biconcave à symétrie de révolution. En 1972, Evans et Fung [45] ont caractérisé la géométrie des GRs sur un échantillon de 50 GRs, à l'aide d'un microscope interférentiel. En moyenne, ils ont trouvé que les GRs ont un diamètre de $7,82$ μm pour un volume de 94 μm^3, dans des conditions isotoniques. La surface de la membrane mesure environ 135 μm^2. Cette géométrie varie en fonction du globule

rouge étudié, de la personne dont il est issu, mais également en fonction du milieu extérieur dans lequel les GRs sont suspendus.

Les globules rouges jouent de nombreux rôles dans l'organisme. Leur rôle principal est bien sûr le transport de l'oxygène et du dioxyde de carbone dans l'organisme. Ce transport s'effectue grâce au liquide interne enfermé dans le GR, contenant de l'hémoglobine, une molécule transportant un ion de fer permettant de capter et de restituer l'oxygène. Les globules rouges transportent également le dioxyde de carbone des tissus aux poumons.

Les globules rouges ont par ailleurs un rôle majeur dans le processus de margination des leucocytes, ou globules blancs [52] et des plaquettes [92]. La margination est le phénomène qui tend à pousser les cellules contre les bords des vaisseaux pour augmenter leur densité près des parois auxquelles elles sont nécessaires pour participer aux réponses inflammatoires ou de coagulation, par exemple. Enfin, les globules rouges jouent également un rôle important dans les processus de thrombose et d'hémostase [92].

La manière dont se déforme le GR, plus précisément la manière dont la membrane se déforme, est essentielle afin de permettre au GR de jouer son rôle dans l'organisme, car les échanges gazeux ont lieu dans la microcirculation, où le diamètre des capillaires est de quelques microns seulement, inférieur donc à celui des GRs au repos.

Un exemple illustrant les niveaux importants de déformation que les GRs peuvent subir au sein de l'organisme est le cas du passage des GRs dans la rate. Une expérience visant à reproduire ces niveaux de déformations a été réalisée par Gambhire *et al.* 2017, et est illustrée Fig. 2.

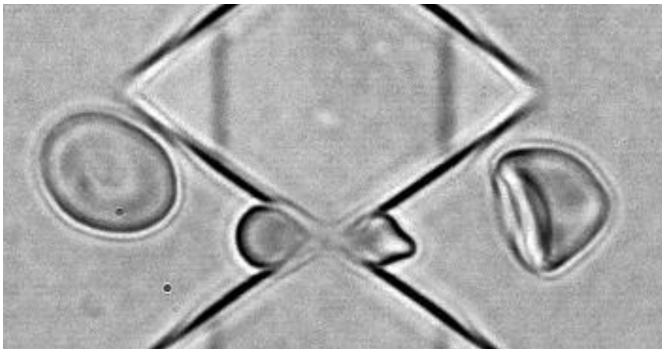

Figure 2: RBC passant à travers un dispositif mimant le passage à travers la rate. Image reproduite de Gambhire *et al.* 2017 [64]. Les différentes cellules représentent le passage d'une seule cellule à différents moments.

En effet, la rate est un organe contenant des micro-ouvertures pour le passage des GRs, générant ces niveaux de déformations. Le passage dans la rate peut être vu comme un test de la bonne santé des GRs. En effet, les GRs ne pouvant pas se déformer suffisamment pour passer la rate restent bloqués dans la rate et sont consommés par les macrophages.
Le fait que les GRs ne peuvent pas se déformer suffisamment peut provenir de plusieurs phénomènes. Les GRs ont une durée de vie d'approximativement 120 jours. Les GRs en fin de vie sont plus rigides, et sont ainsi triés grâce à la rate.
De même, de nombreuses pathologies altèrent la déformabilité des GRs. C'est le cas par exemple de la drépanocytose, où la polymérisation de l'hémoglobine désoxygénée peut déformer les GRs jusqu'à prendre la forme une faucille rigide. C'est aussi le cas de la sphérocytose qui altère certains GRS qui deviennent de forme quasi-sphérique, ce qui en limite la déformabilité. Il y a donc un lien fort entre déformabilité des GRs et la santé. Il convient donc d'étudier la manière dont les GRs se déforment et comment les différentes pathologies altèrent les propriétés de circulation des GRs.

L'étude de la déformations des GRs a d'abord été expérimental. Ainsi, de nombreuses expériences visant à solliciter les GRs selon certains modes de déformation ont été développés. Pour n'en citer que quelques-uns, il existe par exemple l'expérience de micropipette visant à aspirer une partie de la membrane d'un GR [45, 46]. Il est possible de relier la force d'aspiration à la quantité de membrane aspirée, et ainsi obtenir des informations sur le comportement élastique de la membrane. L'essai de traction par pinces optiques permet également de mesurer des propriétés élastiques du GR à grande échelle (cellule complète) [75]. Il existe également des expériences visant à étudier le comportement du GR dans un écoulement fluide cisaillé. C'est le cas de l'ektacytométrie qui quantifie la déformabilité des cellules par un indice de déformation moyen des GRs dans un fluide visqueux, avec ou sans variation de l'osmolarité [12, 17].
Depuis les années 70, s'est développée la simulation numérique de la déformation et de la dynamique des GRs. Elle a permis de donner accès à beaucoup d'informations inaccessible avec une approche expérimentale. Cette approche a été permise grâce aux mesures expérimentales permettant d'en apprendre plus sur le comportement du GR. Cette approche permet d'enrichir les outils disponibles et de pallier certaines limitations des mesures expérimentales liées, entres autres, à l'échelle du problème. Les modèles actuels permettent l'étude de GR isolés ou d'effets de groupes liés à la présence de plusieurs GR dans l'écoulement dans le

cas des suspensions (voir Fig. 3). L'étude des effets collectifs permet d'aborder les questions de circulation, de margination, d'hémorhéologie, etc.

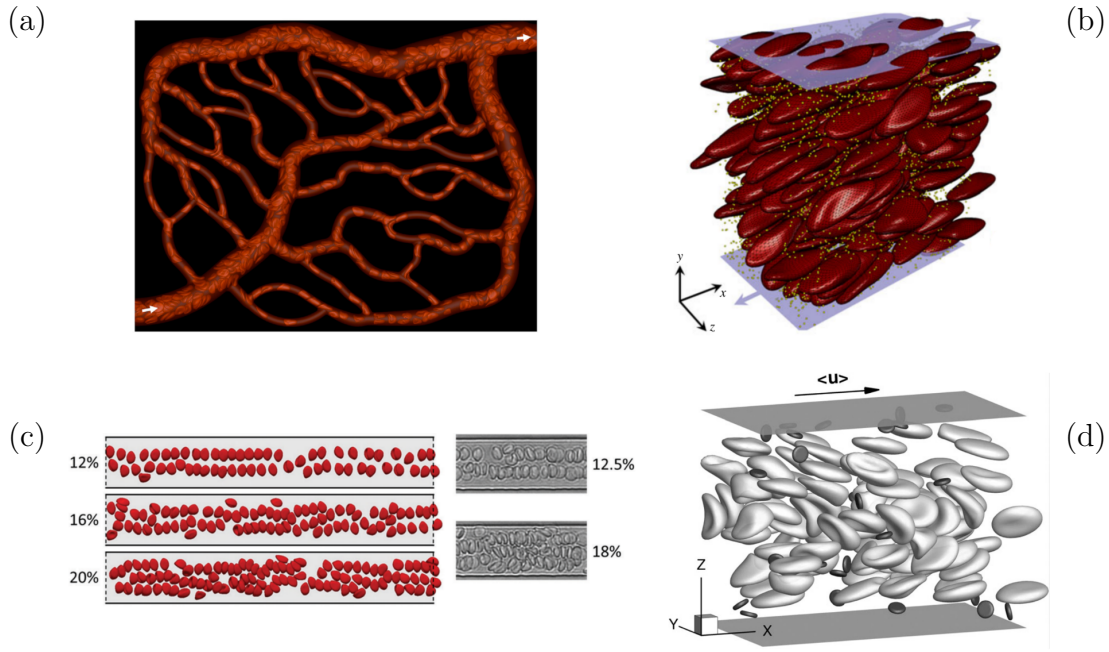

Figure 3: Différentes images montrant illustrant les effets collectifs dans les suspensions de globules rouges. (a) Simulation du passage des GRs dans un réseau représentatif de la microcirculation, images de Balogh *et al.* (2017) [8]. (b) simulation des GRs et des plaquettes dans un flux cisaillé. Images tirées de l'ouvrage concernant la diffusion effective de microparticules dans le sang de Liu et al 2019 [97]. (c) Simulation du train de globules et comparaison avec la photo expérimentale. Image extraite du travail d'Iss et al 2019 [81]. (d) Simulation de l'écoulement de globules rouges et des plaquettes entre les parois d'un canal plan. Image tirée des travaux sur la margination de Zhao et al 2012 [166].

Cependant, les modèles numériques utilisés doivent être suffisamment pertinents pour pouvoir interpréter des résultats expérimentaux, voire d'être aussi fiables que l'approche expérimentale. Cela nécessite d'étudier l'ensemble des aspects du comportement de la membrane dans le but d'améliorer des modèles numériques et d'augmenter leur domaine de validité.

Parmi les comportements mécaniques de la membrane de GR classiquement observés, un phénomène reste sous-représenté parmi les modèles théoriques et numérique : la dissipation dans la membrane elle même. La viscosité de membrane est associée à comme la dissipation interne provoquée par le frottement interne de

la membrane lorsque celle-ci se déforme à une certaine vitesse. Ce phénomène a pourtant été observé expérimentalement depuis les années 70, notamment grâce à des expériences utilisant la micropipette pour mesurer le retard entre l'application d'une force et l'atteinte de l'état d'équilibre de la membrane [46, 79]. Plus récemment, des mesures de la dissipation ont été réalisées en fixant une microbille ferromagnétique à la membrane de GRs et en appliquant un champ magnétique oscillant afin de solliciter périodiquement la membrane des GRs [135]. Enfin, des écarts significatifs entre les simulations et les mesures expérimentales ont été trouvés lors de la reproduction de certains comportements numériquement, et ont été justifiés par la non prise en compte de la viscosité de membrane dans les simulations [38]. Il est certain que si la viscosité de membrane des GRs impacte les comportements du GR isolé, elle peut aussi influencer les phénomènes collectifs en suspension. C'est l'ensemble de ces éléments qui a motivé ce travail de thèse.

La problématique de cette thèse est donc la modélisation de la viscosité de membrane dans les simulations numériques et l'impact de sa prise en compte sur la dynamique des GRs dans des cas élémentaires pour lesquels des mesures expérimentales sont disponibles.

Dans un premier temps, une présentation plus complète du cadre scientifique de cette étude est faite dans le chapitre 1. Il sera détaillé dans ce chapitre plus d'informations concernant la nature du GR, les différents types de mesure que l'on retrouve dans la littérature ainsi que les différents types de modèles numériques existants.

Dans le **chapitre 2** sera présenté le cadre physique, introduisant les différents modèles physiques utilisés dans cette étude. Nous y discuterons à la fois de la modélisation de partie élastique, classique dans les travaux de modélisation et de la modélisation de la viscosité de membrane.

Le cadre numérique de cette étude sera présenté dans le **chapitre 3**. Il s'agira ici de détailler le modèle utilisé pour les simulations durant cette étude, à savoir le modèle présent dans le code de calcul YALES2BIO. C'est aussi dans cette partie que l'implémentation et la validation du modèle numérique de la viscosité de membrane seront présentées.

Le **chapitre 4** regroupe deux études numériques réalisées dans le cadre de cette thèse utilisant le modèle de viscosité de membrane développé. La première étude concerne la modélisation d'un comportement particulier du GR dans un écoulement cisaillé, à savoir le tank-treading. Cette étude purement numérique

est basée sur des mesures expérimentales provenant des travaux de Fischer et al [54, 56]. Ce travail a permis la mise en lumière d'un fort impact de la viscosité de membrane sur le comportement en tank-treading du GR. Elle a également permis de montrer une reproduction possible des mesures expérimentales en supposant un modèle de membrane rhéofluidifiante, hypothèse déjà présente dans la littérature. Cette étude a abouti à la publication d'un article dans le journal Physical Review Fluids en 2021 [102].

La seconde étude concerne la conception d'une expérience en flux dédiée à la mesure du comportement visqueux de la membrane des GRs. Il s'agit de l'étude de l'élongation des globules dans un dispositif d'écoulement en croix. Cette étude a été réalisée en collaboration avec l'entreprise HORIBA Medical ainsi que le Centre de Biochimie Structurale (CBS) de Montpellier. Ce travail a permis de mettre en lumière l'impact important de la viscosité de membrane sur le comportement des GRs dans ce type de dispositif. Il a permis également la mise en place de la chaîne de simulation ainsi que les différents outils de traitement nécessaires à la compréhension du comportement du GR en extension.

Enfin, le dernier **chapitre 5** récapitule les résultats majeurs, présente les limitations du travail et propose plusieurs ouvertures possibles.

Contents

Contents **xiii**

Chapter 1 Introduction **1**

1.1 Red blood cell's presentation 1
1.1.1 General presentation 1
1.1.2 Geometry 3
1.1.3 Role 4
1.1.4 Membrane 5
1.1.5 RBC's deformability and link with health 6
1.2 Mechanics and rheology 8
1.3 Sensitivity of red blood cell dynamics to mechanical parameters . 17
1.4 Motivations 20
1.4.1 Experimental highlighting 20
1.4.2 Impact of the membrane viscosity on the RBC's dynamics: What do we know? 23
1.4.3 Goal and presentation of this work 24

Chapter 2 Physical framework **27**

2.1 Introduction: a multiphysics problem 28
2.2 Fluids 29
2.2.1 Fluid model 29
2.2.2 Flow regime 29
2.2.3 Inner fluid properties 30
2.3 Red blood cell membrane model 31
2.4 Modeling the inviscid behavior of the RBC membrane 33
2.4.1 In-plane behavior: Hyperelasticity 33
2.4.2 Curvature forces 33
2.4.3 Stress-free shape 34
2.5 Membrane Viscoelasticity 35
2.5.1 Physical meaning of the viscoelasticity 35

2.5.2 Introduction to rheological representation and small strain viscoelastic model . . . 37
2.5.3 Viscoelastic model for the membrane . . . 40
2.6 Non dimensional numbers . . . 43

Chapter 3 Numerical framework **47**
3.1 Introduction . . . 48
3.2 Flow solver . . . 49
3.2.1 The Navier-Stokes equations and their time advancement . . . 49
3.2.2 Space discretization method: Finite Volume Method . . . 50
3.2.3 Variable viscosity . . . 54
3.3 Fluid-structure interaction: Immersed Boundary Method . . . 55
3.3.1 Coupling: General algorithm . . . 55
3.3.2 Coupling: Interpolation and Spreading . . . 56
3.3.3 In-plane stress: Hyperelasticity . . . 59
3.3.4 From element stress to nodal forces . . . 60
3.3.5 Curvature forces . . . 62
3.4 Implementation of the membrane viscosity . . . 63
3.4.1 Implementation . . . 63
3.4.2 Validation: small strain cases . . . 66
3.4.3 Convergence Zener to Kelvin-Voigt . . . 69
3.5 Validation: capsule under shear flow . . . 70

Chapter 4 Application **75**
4.1 Introduction . . . 76
4.2 Effect of membrane viscosity on tank-treading red blood cells . . . 77
4.2.1 Introduction . . . 77
4.2.2 Numerical setup and operating points . . . 77
4.2.3 Non-dimensional study . . . 80
4.2.4 Dimensional study . . . 83
4.2.5 Shear-thinning model . . . 86
4.3 Strain experiment: RBCs in an extensional flow . . . 89
4.3.1 Introduction . . . 89
4.3.2 Design of the extensional flow . . . 90
4.3.3 Numerical setup and operating points . . . 94
4.3.4 Initial state of the RBC in the crossflow device . . . 99

4.3.5 Experimental case's preliminary results using tank treading initial shape and outcomes 100

Chapter 5 Conclusion and perspectives **107**

5.1 Main Results 107

5.2 Perspectives 109

5.2.1 Study at the micro scale of the membrane 109

5.2.2 Study at the macro scale of the membrane 110

Chapter 6 Appendix **113**

6.1 Appendix 1: Discretization of operators 114

6.1.1 Laplacian operators 114

6.1.2 Divergence operators 115

6.1.3 Gradient operator 116

Bibliography **119**

Chapter 1

Introduction

Chapter contents

1.1 Red blood cell's presentation 1
1.1.1 General presentation 1
1.1.2 Geometry 3
1.1.3 Role 4
1.1.4 Membrane 5
1.1.5 RBC's deformability and link with health 6
1.2 Mechanics and rheology 8
1.3 Sensitivity of red blood cell dynamics to mechanical parameters . 17
1.4 Motivations 20
1.4.1 Experimental highlighting 20
1.4.2 Impact of the membrane viscosity on the RBC's dynamics: What do we know? 23
1.4.3 Goal and presentation of this work 24

1.1 Red blood cell's presentation

1.1.1 General presentation

Red blood cells (RBCs in this study) are the most common cells in the blood of the vertebrates [151]. A representation of the different components in human blood

is presented Fig. 1.1. In the specific case of the human blood, RBCs represent approximately 45% of the blood volume for men and 35-40% of blood volume for women. Those levels of RBC volume concentration called the hematocrit, are representative of many species [159]. In the following, the term blood will be used to refer to human blood *et al.*l RBC characteristics will refer to human cells. In blood, cells are suspended in plasma, which occupies most of the remaining volume. Plasma is mainly composed of water (at approximately 90%) and contains up to 10% of proteins, and other components up to 1 or 2%. Finally, approximately 1% of the blood volume is occupied by other circulating cells, the white blood cells and the platelets. The average number of RBCs per liter of blood in an adult is 5.4×10^{12} for men and 4.8×10^{12} for women. RBCs are the most present cells in the organism. Red blood cells are generated in the bone marrow during a process called erythropoiesis. This process lasts approximately 5 days. During this process, the red blood cell goes through different phases with each different shape before reaching the discocyte form. Also, red blood cells are ejected from the bone's narrow to the circulation before they reach their well-known mature shape of a discocyte, a biconcave disk. It takes about 2 days to reach the discocyte shape once in the circulation [111]. During this phase, in comparison with the cell present in the bone narrow, they lose their nucleus. Two important specificities of the red blood cell are that it does not have a nucleus and it is able to deform to reach all the irrigated areas of the body.

The RBC lifespan is approximately 120 days. Along their lifespan, RBCs age and progressively rigidify. At some point, they become unable to go through the spleen, which acts as a filter to remove old/rigid cells from the circulation. Once stuck in the spleen, cells are ingested by the body to evacuate toxins and to recycle RBC's component as well as possible. Some of the RBC degradation products are stored in the spleen for reuse. Another part of this waste, such as iron, is sent to the liver to then transmit to the bone marrow to produce hemoglobin, the internal fluid of RBCs, carrying oxygen [157]. This lifespan corresponds to about 2.5 million blood cells dying every second. To replace dead cells, the same number is produced by the body at the same time.

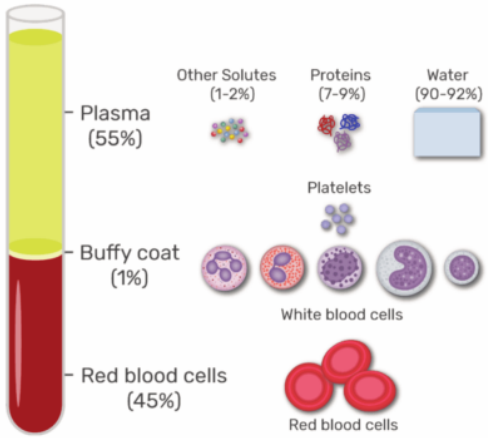

Figure 1.1: Representation of the result of a centrifugation of blood. This process enables to separate the different elements of the blood composition. Picture taken from Taraconat [154]

1.1.2 Geometry

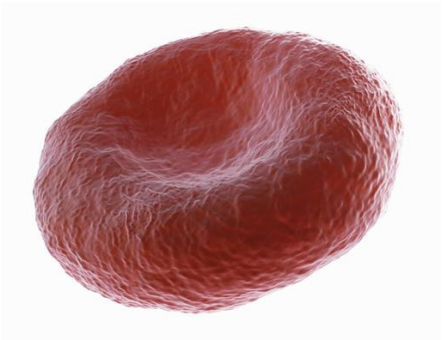

Figure 1.2: The discocyte shape of a RBC. Credit: Science Picture Co Collection Mix: Subjects Getty Images.

A healthy RBC has a discocyte shape (Fig. 1.2). It is the resting form of the RBC, *ie* when the blood cell is not under flow. It is typically a biconcave form with symmetry in revolution. In 1972, Evans and Fung [45] characterized the RBC geometry on a sample of 50 RBCs, using an interference microscope. On average, they found that RBCs are 7.82 μm in diameter for a volume of 94 μm^3, in isotonic conditions. The area of the membrane measures approximately 135 μm^2. However, those characteristics depend on the individual and can change with the external medium. For example, the Evans and Fung (1972) highlight the impact

of the osmolarity of the external medium, as it can be seen Fig. 1.3.

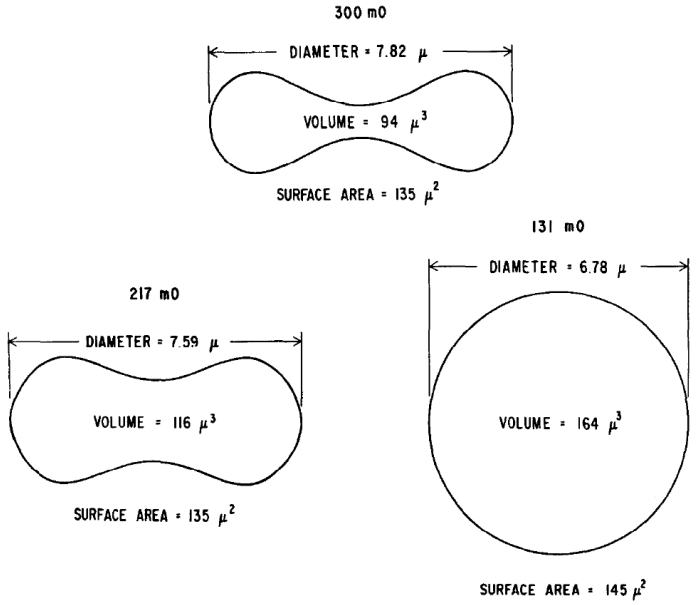

Figure 1.3: Drawing of the RBC average geometrical characteristics for different osmolarities, from Evans and Fung 1972 [45].

1.1.3 Role

RBCs play many roles in the body. Their main role is of course the transport of oxygen from the lungs to the various tissues and organs of the body on carbon dioxyde on their way back. This transport is performed thanks to the internal fluid enclosed in the RBC, containing hemoglobin, a molecule transporting an iron ion, making it possible to catch and release oxygen. To ensure the good oxygen distribution throughout the body, recent research also highlights their role as chemical sensors-regulators [41, 60]. Indeed, the red blood cells, by releasing adenosine triphosphate (ATP), a molecule that dilates blood vessels, plays a fundamental role in meeting local oxygen needs in the body.

RBCs also have a major role in the process of margination of leukocytes, or white blood cells [52], and platelets [92]. Margination is the phenomenon that tends to push cells against the edges of vessels to increase their density near walls where they are needed to participate to inflammatory or coagulation responses, for instance. Finally, RBCs also play a significant role in the processes of thrombosis and hemostasis [92]. The deformability of the membrane is essential to allow the RBC to play its role in the body.

1.1.4 Membrane

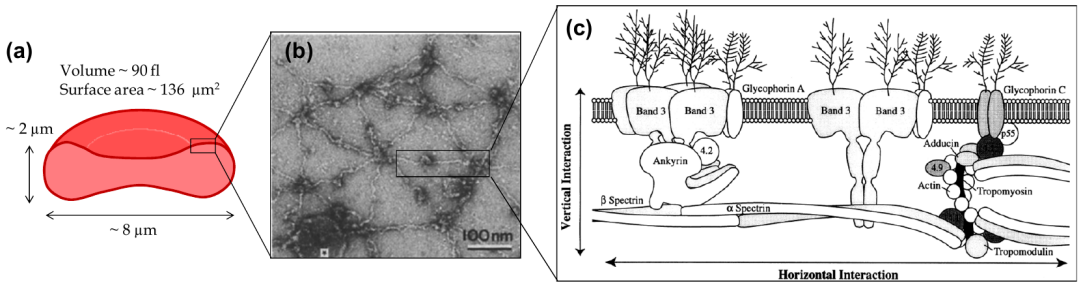

Figure 1.4: Pictures taken from Kim *et al.* [86]. (a) Cross-sectional view of a red blood cell with a zoom on the membrane shown in (b), showing the spectrin network. (c) Schematic of a red blood cell membrane model.

The membrane of RBCs is composed of multiple elements, as it can be seen in Fig. 1.4 [86]. First, a lipid bilayer at the surface of the RBC ensures the sealing between the internal medium and the external environment of the RBC. However, exchanges of water are enabled and controlled by the osmotic pressure. Thereby the membrane ensures a selective permeability. Its thickness is of approximately 4 nm. However, the external glycocalyx, which regulates the membrane permeability, can extend to a size of 10 nm [73]. The lipid bilayer is also crossed by proteins that form little channels inside the bilayer to enable communication between the two environments. Below this bilayer and linked to it is the cytoskeleton of the membrane.

The spectrin network, which is linked to the bilayer thanks to multiple proteins that are anchored in the bilayer, gives rigidity to the membrane. Its organization can be seen in Fig. 1.4 (b) and (c). The spectin monomers measure 5 nm and the spectrin molecule is present at approximately 2^5 copies for a single RBC. The thickness of the spectrin network is approximately 40 nm [73]. However, those orders of magnitude of the spectrin network thickness is highly depending on the membrane deformation [73].

The membrane has multiple roles. First, it ensures that the hemoglobin does not circulate freely in the body, thanks to the lipid bilayer. Indeed, to catch oxygen, the hemoglobin contains an iron ion that is harmful for the body.
Then the membrane has for main constraint to ensure the supply of the oxygen inside every area of the organism. To do so, the cell has to be deformable enough. In the human body, the circulation network is composed of large vessels where

RBCs can freely circulate (like the aorta, of a diameter of approximately 2.5 cm), but also narrow channels. Indeed, capillaries are only a few micrometers large, which means that RBCs must circulate inside vessels smaller than their diameter at rest.
Even larger deformations are undergone by the RBCs when they circulate in the spleen. Indeed, during their passage, the RBCs must be able to deform sufficiently to pass through openings with an order of magnitude of less than one micrometer. [61]. Moreover, all RBCs must pass through the spleen multiple times during their lifespan. A visualization of RBCs passing through devices that mimic the passage through the spleen can be found in Fig. 1.5, from the work of Gambhire *et al.* (2017) [64].
At the end, an RBC undergoes very large deformations, and without its great deformability, it cannot reach every area in the body and cannot fuel the tissues with oxygen or being filtered by the spleen.

1.1.5 RBC's deformability and link with health

The word deformability is an important keyword in the study of the RBC behavior. However, even if definitions have been given in the literature [23, 115], the concept is vague. Indeed, we may call deformability the capacity of a body (here a RBC) to change its shape in response to a stress. The nature of this deformation can vary (change of area, curvature, shear ...) and it is important to note that in the literature the term deformability encompasses all these forms of deformation, but also mixes different types of stresses.
In hemorheological studies, the term deformability is generally associated with the deformation measured using ektacytometry, by measuring the relative lengthening of RBCs under shear [16, 17, 120]. The quantity measured is well defined, but the differences in deformability may come from the cytoplasm or the membrane of the RBCs, for instance. Another example is the use of the deformability term are study using Laser Assisted Optical Rotational Cell Analyzer (LORCA) [71]. Indeed, in this context, deformability refers to measurements of the elongation index and of the mean cell transit times in the device. This shows that, depending on the context, this term may or may not have a precise meaning.
However, even if the definition of the term is not clear from a mechanical/physical point of view, RBC deformability (its ability to change its shape) is so important that the body tests it as a criterion for RBC capability to fulfill its role in the

circulation, when the RBCs pass through the spleen. Indeed, one of the functions of the spleen is to eliminate RBCs that cannot circulate normally inside the organism due to an altered deformability.

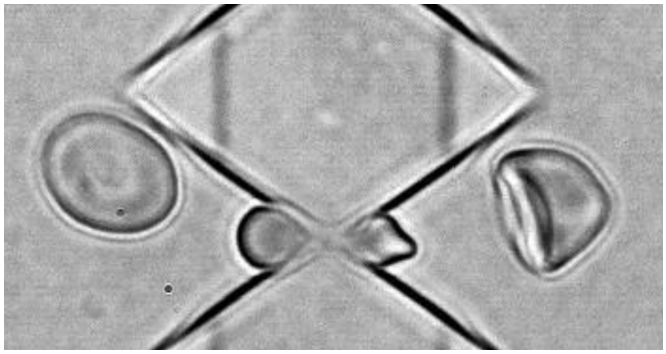

Figure 1.5: RBC passing through a biomimetic splenic slit from Gambhire *et al.* (2017) [64]. The different cells represent different times during the passage of the cell through the device.

Indeed, the deformability of the RBCs can be altered. As already mentioned, aging changes the cell deformability. The aging of an RBC changes its shape [132, 158]. Indeed, during its lifetime, the RBC loses up to 30% of its initial volume and gradually loses its membrane in the form of small vesicles. By increasing the enclosed volume with respect to the membrane area, this leads the aged RBCs to become less deformable than the younger healthy ones [31, 77, 134]. In addition, the cytoplasm of old cells has a higher concentration in hemoglobin than young cells, which increases the cytoplasm viscosity [25]. However, changes seem to be more pronounced in the first week of the cell, as shown by joint measurements of volume and hemoglobin content of population of red blood cells [77].

Finally, some diseases alter the shape of RBCs, such as sickle cell anemia, which is characterized by the presence of RBCs in the form of a rigid sickles [13, 43], or spherocytosis, characterized by RBCs in the form of small barely deformable spheres, and elliptocytosis [32, 111], to name a few. Those are genetic diseases, but other pathologies like type II diabetes or COVID-19 also alter RBC deformability [4, 116]. We therefore also have a strong link between the deformability of the RBC and health.

These examples show that the deformability of the RBCs can be altered in different ways. They also show that the RBC deformability can be used as a health-o-meter, to identify some diseases. However, in diagnostics, deformability generally refers to a behavior through a deformability score, which is specific to the

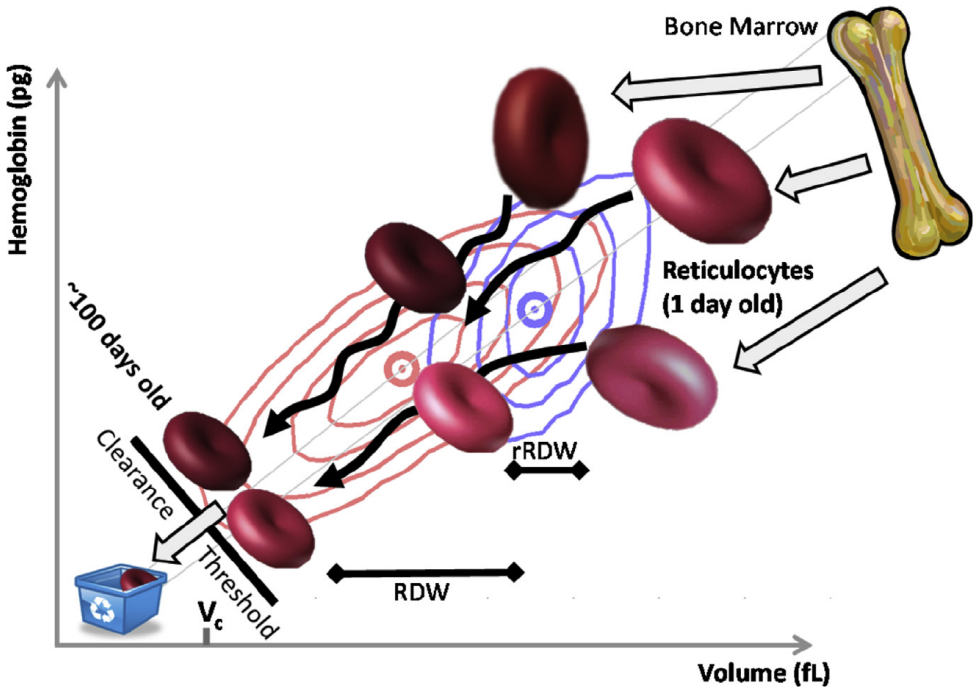

Figure 1.6: Graph showing the different volume and amount of hemoglobin of red blood cells over their lifetime. Red contours represent the probability density for volume and hemoglobin in the total RBC population of a healthy adult. The blue contours represent the same probability density for reticulocytes. Contours enclose respectively 90%, 75%, 50% and 25% of cells. The gray lines are lines of constant hemoglobin concentration. From Higgins (2015) [77]

.

context or test undergone by the RBCs. To go further in the understanding of RBC mechanics in health and disease, a more precise definition of what deformability means is needed: for instance, a reduced deformation index in ektacytometry may come from a higher cell viscosity, a stiffer membrane or a change in the cell aspect ratio. If RBC deformability is sensible to many pathologies, its lack of specificity limits its use as a true diagnostic index. We will see that we need to separate the deformability into several elementary aspects, for which mechanical characteristics may be defined.

1.2 Mechanics and rheology

To define more precisely the meaning of the deformability in the RBC's framework, it is necessary to make an inventory of the different membrane mechanical behav-

iors that has been observed experimentally. The membrane is composed of a lipid bilayer on which is anchored a cytoskeleton. Each of these elements contributes to the overall mechanics of the membrane in a different way. The bilayer limits the area change of the RBC membrane and bursts if a change of area of more than a few percents is imposed [45, 91]. At ambient temperature, this corresponds to a membrane area modulus of 450 mN.m^{-1} [78]. It is this very small change in area

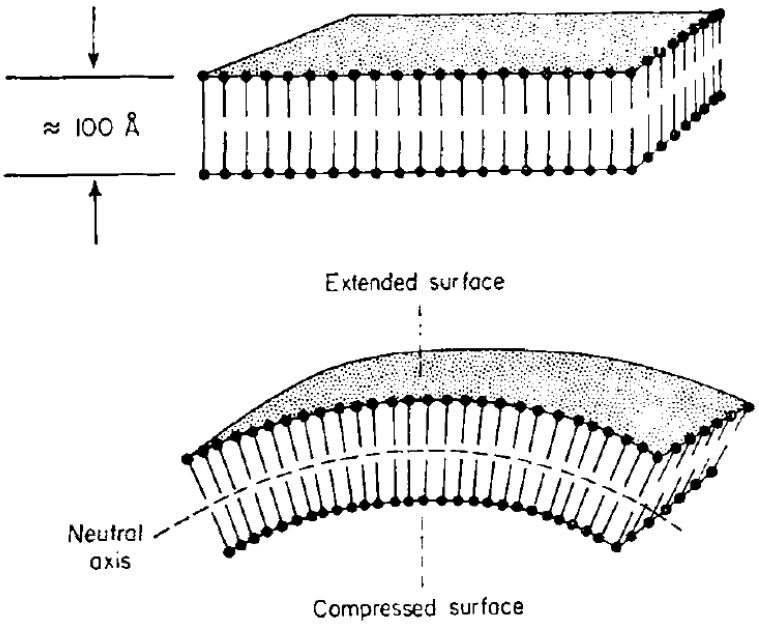

Figure 1.7: Figure showing the physical link between the compressibility and the ability to bend of a biological membrane: bending is only possible if different local changes of area are possible for the two layers of lipid. From Canham (1970) [20].

that the bilipidic layer allows, which results in a significant curvature modulus [20, 78, 143]. This curvature modulus is of the order of 10^{-19} N.m. The physical link between compressibility and bending is illustrated in Fig. 1.7.

The cytoskeleton is responsible of the shear resistance of the membrane. The order of magnitude of the shear modulus of the cytoskeleton is 2.5μ N.m^{-1}. Its area change modulus, on the other hand, is of the same order of magnitude as the shear modulus (typical twice as large) and thus much lower than that of the bilipidic membrane, by five orders of magnitude [75]. This low area change modulus implies that its resistance to bending is negligible compared to the resistance provided by the bilipid layer.

All those observations are relevant of an elastic behavior of the membrane. The elastic behavior means that the material has a reference state, which is the config-

uration to which the material will return geometrically as soon as it is freed from the external forces. Thus, for a material said to be purely elastic, it is possible to directly link its deformed state to its internal stress by only knowing its reference state[1].

This behavior was first demonstrated using an experimental device called a

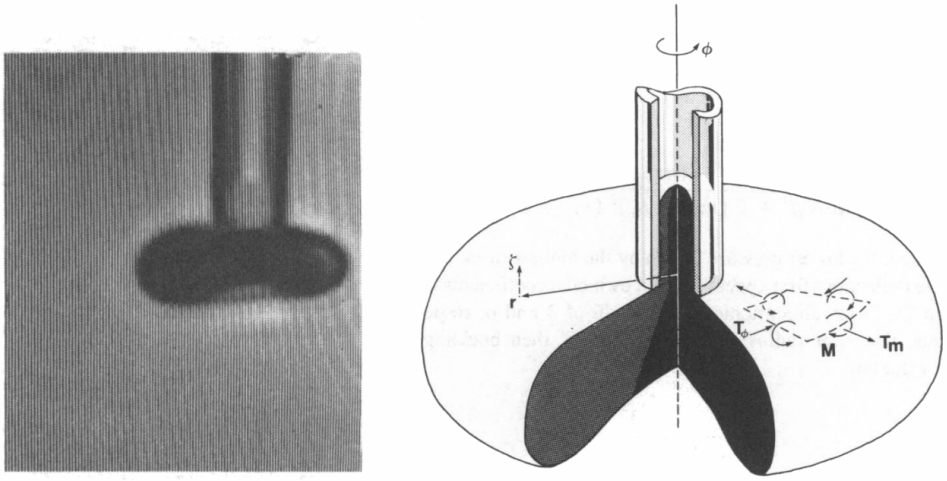

Figure 1.8: Photo and diagram of a micropipette experiment on a RBC. From Evans (1983) [44]

.

micropipette, illustrated in Fig. 1.8. The idea of this experiment is to impose a suction on a part of the membrane of the RBC. By measuring the amount of membrane sucked into the pipe for a given suction, it is possible to trace the stress that is imposed in the material and therefore its elastic properties. These works have been widely put forward by Evans and Hochmuth, among others, and have allowed a first understanding of the deformability of the membrane [45, 46]. Generally, by removing the pressure applied, we notice that the aspirated membrane retracts, and that the RBC regains its initial shape, which accounts for the elastic behavior.

Similarly, another experimental means of highlighting the elastic aspect of the behavior of the RBC membrane is by using optical tweezers, represented in Fig. 1.9. Indeed, this technique makes it possible, by fixing beads of silica on the membrane

[1] This reference state can be a stress-free configuration or can be considered as a stress-free configuration without the knowledge of the stress field on the material. In the case of the RBC, the problem of the reference shape of a RBC corresponding to the problem of knowing the prestress field on a RBC in discocyte shape. This aspect is presented later in this part.

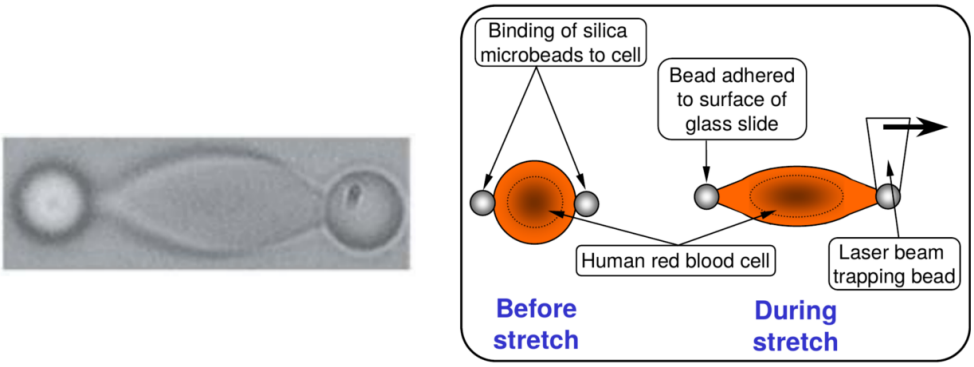

Figure 1.9: Photo and diagram of a stretching of a RBC using optical tweezers. Taken from Dao et al. (2003) [34]

.

of the RBCs and exert a force on the membrane. This technique therefore allows to measure the elastic character of the RBCs [75], in a similar way to the technique of micropipette.

Another way to measure the elastic properties of RBCs is ektacytometry, illustrated in Fig. 1.10. Ektacytometry is the process of studying the deformation of RBCs in a liquid medium where a shear is imposed. The measurement of this deformability is done using a laser which, by crossing the moving solution, generates a diffracted image characteristic of the deformation of the RBCs in the flow [12]. Thus, if no shear rate is imposed in the sample, the image produced is circular. Once the shear rate is imposed, the diffracted image caused by the passage of the deformed cells in front of the laser is an ellipsoid, as cells elongate in the direction of the flow. The characteristics of this ellipsoid are related to the deformation of the RBC shape in the imposed flow. Classically, the information measured during ektacytometry experiments is linked to an elongation index $EI = \frac{L-l}{L+l}$ with L and l respectively the major and minor axis of the elliptix diffraction image. It has been shown that this elongation changes depending on the age of the RBCs as well as the pathologies present such as sickle cell disease or spherocytosis [12, 17]. The ektacytometry experiment has become the gold standard when it comes to testing RBC's deformability [11] in the clinical context. This elastic behavior means that a membrane with a very high elastic modulus will stiffen the RBC, while conversely a RBC with a low elastic modulus can deform easily. However, as already said, ektacytometry measurements may be affected by a change of deformability due to other aspects of the cell, notably cell

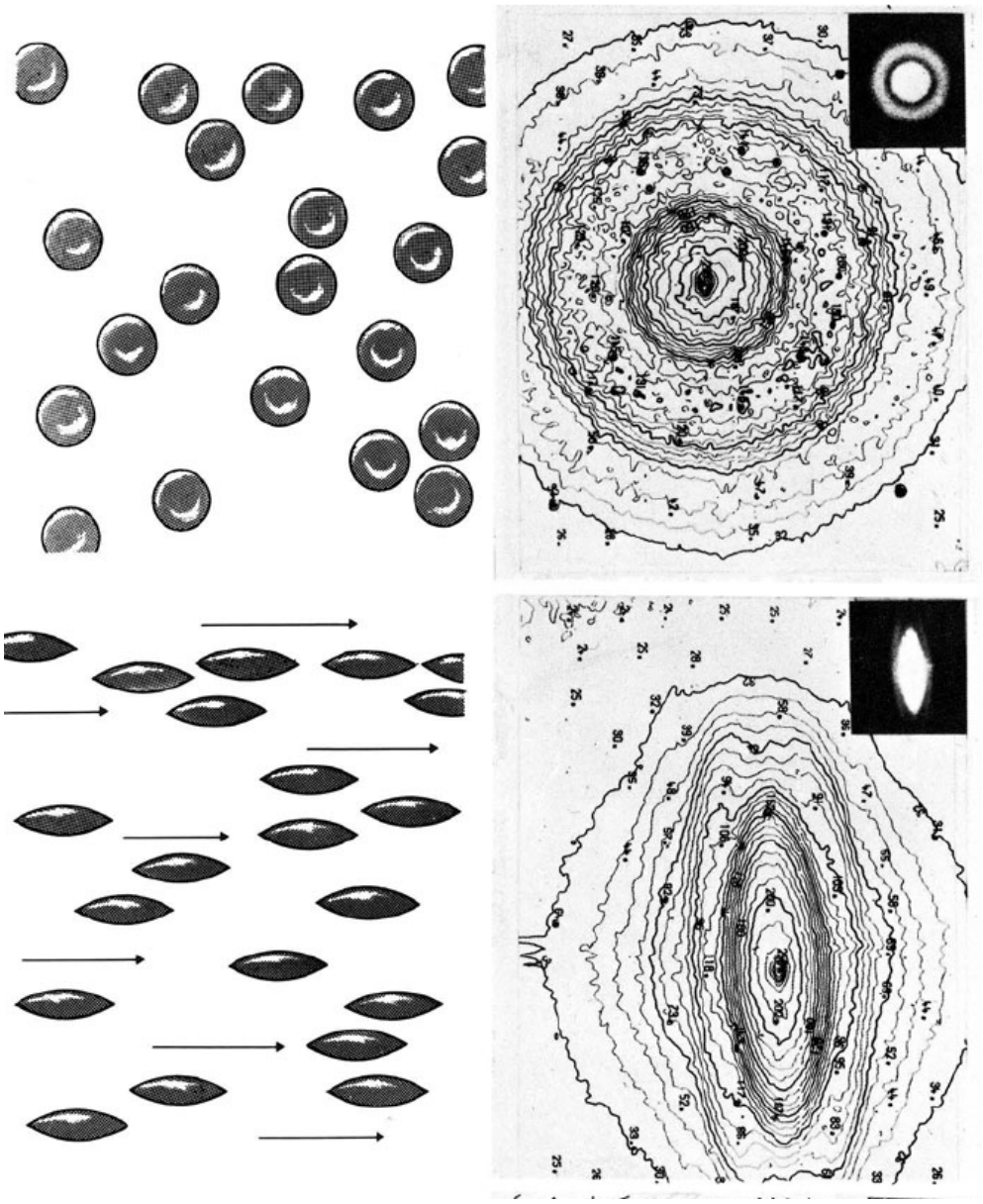

Figure 1.10: Diagram representing RBCs during a measurement using ektacytometry (left) and resulting diffracted images (right). From Bessis et al. (1981) [12]

.

viscosity, which is not the case of static techniques.

A second parameter governing the RBC deformability is the surface-volume ratio of the RBC. The aspect ratio (or isoperimetric quotient) is the ratio between the surface S of the membrane of the RBC and the volume V it contains to

obtain a non-dimensional number. It is calculated as $\frac{S^3}{V^2}$. It gives us information about the shape of the RBC. The lowest area-to-volume ratio, for a given volume, is obtained for a sphere. Average measurements allowing indirectly to measure the aspect ratio of an RBC are available in [45]. By using ektacytometry as a measure of the deformability of RBCs, and by subjecting these RBCs to different chemical treatments as well as to different osmotic pressure values, the impact of the surface/volume ratio has been highlighted [138]. It has therefore been shown that a low aspect ratio tends to stiffen the RBC.

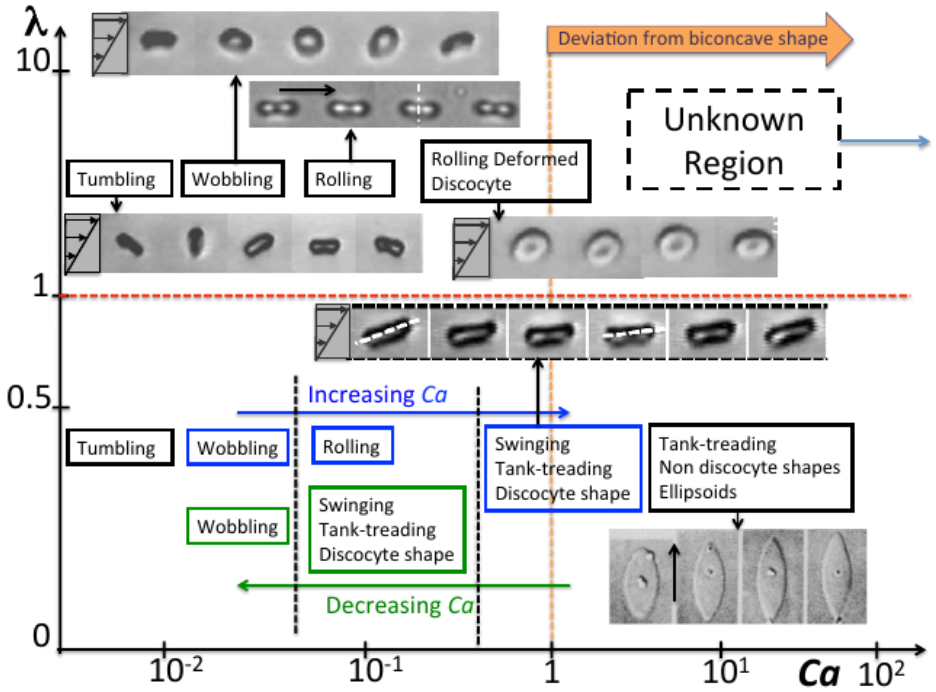

Figure 1.11: Diagram representing different RBC's behaviors as a function of the viscosity ratio between the cytoplasm and the external fluid and of the capillary number, which represents a ratio between the shearing viscous forces applied on the RBC and the elastic restoring forces of the membrane. From Abkarian and Viallat (2016) [3]. The 'Unknown Region' of the diagram has been investigated more recently in [87, 103, 105].

.

Finally, the third essential aspect which has an impact on the deformability of the RBC is its viscosity. Viscosity is linked to the friction between the particles of a material during its deformation. The expression 'RBC viscosity' is not precise enough because the RBC has different sources of viscosity. Indeed, the internal fluid of the cell is a viscous fluid which strongly impacts the deformability of

the RBC. Indeed, it has been demonstrated that viscosity plays a major role in the behavior of RBCs under flow. This is beautifully illustrated in Fig. 1.11, where Abkarian and Viallat [3] have gathered the different dynamics of a single red blood cell in pure shear flow as a function of the viscosity ratio between internal and external fluids and the non-dimensional stress applied. Clearly, the stress applied is a major parameter in terms of dynamics. Large stresses (large capillary numbers in Fig. 1.11) yield visible deformations of the cell. However, the internal viscosity also controls the type of dynamics of the RBC. The diagram was gathered in 2016. Since then, the 'Unknown Region' in the diagram, for large viscosity ratios and large capillary numbers, has been investigated, with the identification of specific dynamics (stomatocyte, trilobe and polylobes under flow, see [87, 103, 105]). Some of those configurations will be detailed later in this work.

Different measurements of the viscosity of hemoglobin solutions can be found in the literature [25, 112, 113]. However, it has been shown experimentally that the RBC's membrane was not only elastic but also viscous [46]. Thus, a membrane with a high viscosity will tend to stiffen the RBC. The impact of membrane viscosity on the deformability of the RBC as well as the measurement of the membrane viscosity value are precisely at the center of this research work.

It can therefore be seen that there are several components of RBC deformability, which are involved or not in the RBC deformation depending on the type of stress it is subjected to. The notion of deformability of the RBC brings together several mechanical behaviors. In general, it is not possible to link a measurement of the deformation to a unique component of the membrane mechanics. Therefore, to allow the study of the deformation behavior of the RBC, it is necessary to model the deformability of the RBC by proposing a 3D mechanical model accounting for the internal fluid and the membrane.

There are several approaches to model these different mechanical properties to obtain a RBC model with a deformability like what is observed experimentally. One type of approach is to directly model the molecular chains of the different components of the RBC. Thus, by modeling the different interactions, we obtain a similar behavior as the experimental deformations observed, and we are therefore able to identify what is the role of each aspect presented previously, and therefore to learn more about the deformability of the RBC. This method also makes it possible to identify the role of each component of the RBC during the local deformation of the membrane. This type of model has the advantage of representing physics

at the molecular level. The direct consequence of working at this scale is that it is difficult to calibrate, most of the experiments measuring properties at the RBC scale and not at the scale of the spectrin network. Finally, this type of model is also more cumbersome to set up [89, 123]. Note that the model by Peng *et al.* [121, 122, 126] is an elaborate multi-scale model which has been applied for simulations of red blood cells under flow, but such models are generally not used for large-scale simulations.

Another type of approach is to consider the membrane of the RBC as a continuous material and thus use the equations of continuum mechanics to translate the different behaviors observed experimentally. The main advantage is to use the mechanical modules that can be estimated from experimental measurements at the cellular level as input parameters. It is therefore easy with this type of model to inspect different behaviors by directly varying the physical parameters used as input. However, the continuity of the membrane is a strong hypothesis. This assumption precludes the identification of local membrane properties, unlike the micro-scale model presented previously. These models are for example used in the works of Bagchi *et al.* [8, 30, 161], Shaqfeh *et al.* [117, 166], Mendez *et al.* [81, 87, 104], Krüger *et al.* [42], among others [36, 61].

Finally, some models choose an intermediate scale, such as the model used in the works of Karniadakis *et al.* and Fedosov *et al.* among others [49, 53, 123, 133, 136]. The idea here is to model the RBC as a binding set of particles with different properties aiming to model the properties of a set of spectrin chains for example. We are therefore on a larger scale than the molecules constituting the membrane, a bond representing a multitude of molecular bonds of the membrane, while not considering the membrane as a continuous material. This type of model is obviously very malleable and adapts to many configurations, although it needs to be recalibrated according to the stresses.

The first interest of having such model is to support experiments in parameter identification. The example of the optical tweezers is interesting in this respect. For small deformations, interpreting the experimental results is rather simple and provides the mechanical moduli of the membrane. However, for large deformations, a model of the RBC is essential for inverse analysis of the data [34, 109]. However, depending on the model used, one may obtain quite different values of mechanical moduli from large-deformation behaviors [35, 109, 146]. The accuracy of the mechanical model is thus essential to use it to support experiments in the context of parameter identification. Another example of the need for numerical simulation

is the question of reference shapes. It is classical in the literature to find the stress-free shape mention concerning the membrane of the RBC [1, 39, 57], which knowledge is required to model the prestress field on the membrane of the RBC. The search for this prestress field leads to finding a shape where the RBC membrane is not constrained, hence the reference shape term. Investigating the impact of different forms of references can only be done through numerical simulation. This makes it possible to sort the different models to choose the most suitable for the study of the deformability of RBCs.

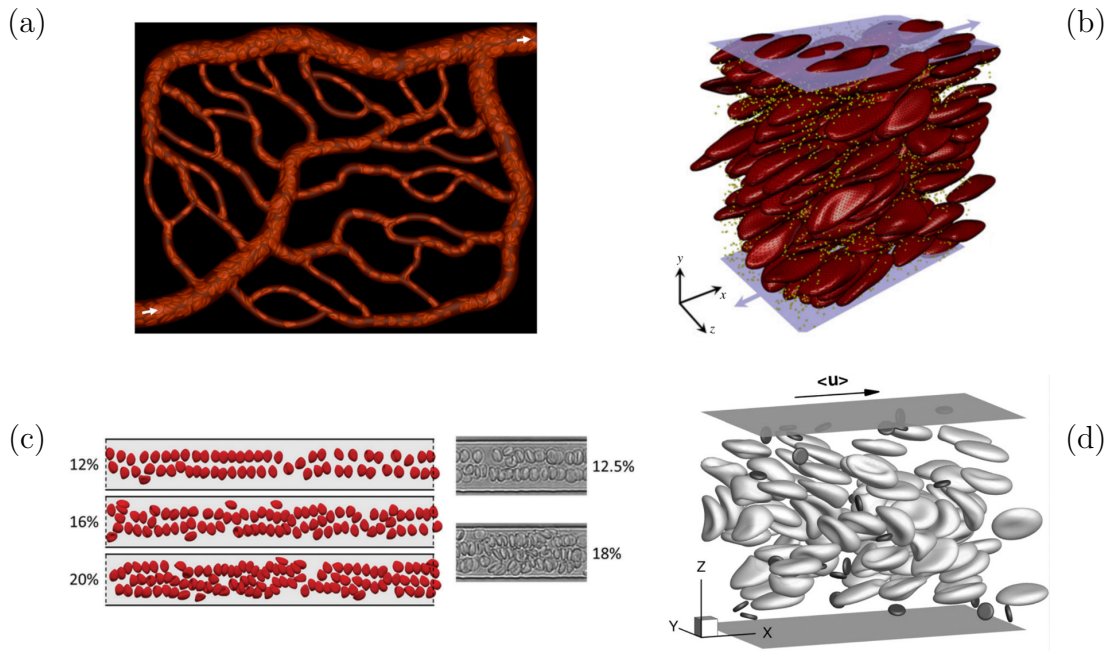

Figure 1.12: Different images showing illustrating collective effects in suspensions of RBCs. (a) Simulation of the passage of RBCs within the microcirculation, images from Balogh *et al.* [8]. (b) simulation of RBCs and platelets within a sheared flow. Images taken from Liu *et al.* [97]. (c) Simulation of globule train and comparison with experimental photo. Image taken from Iss *et al.* [81]. (d) Simulation of RBCs and platelets within a flow. Image taken from Zhao *et al.* [166].

The mechanical models allowing to reproduce the mechanics of the membrane of the RBCs is the central point of the studies concerning the blood on larger scales. Indeed, many phenomena that make blood so special mechanically are linked to the fact that blood is composed of red blood cells that deform during circulation. Examples of the deformations that red blood cells can undergo during blood circulation are visible on Fig. 1.12.

We can cite as an example the phenomenon of margination between platelet and white blood cell [137], globule train dynamics that are no longer present when the RBCs are stiffened [81], shear-induced diffusion phenomena changing the trajectory of RBCs depending on how they deform [166] or even the phenomena of cell free layer and RBC lift, which are highly dependent on the way in which the cells are deformed [67, 165]. Apparent blood viscosity is also a consequence of RBC deformation [87]. Indeed, the apparent viscosity changes with stiffened RBCs compared to deformable RBCs [22, 53]. Of course, transport in networks and the consequences in terms of oxygenation are also determined by red blood cells behavior and can be explored numerically [8, 42].

It can therefore be seen that the search for fine identification of RBC model parameters is dependent on experiment but also on numerical simulation. Simulation is vital to translate experimental measurements into elementary parameters usable in RBC models. Moreover, it is obviously necessary to have a model as complete as possible to be able to fully rely on numerical simulations when exploring blood flow phenomena.

1.3 Sensitivity of red blood cell dynamics to mechanical parameters

In this section, we illustrate more specifically how red blood cell dynamics depends on the membrane characteristics and how dynamics under flow may be used for mechanical characterization.

An excellent configuration to study the relationship between RBC mechanics and dynamics is the single RBC under shear flow. Indeed, it enables to highlight the contribution of different parameters of the membrane according to the established regime. It therefore constitutes an entire section of hemorheology and is still the subject of active study [2, 3, 87, 103, 104, 105, 130].

At low shear rates, the red blood cell in the form of a discocyte starting to have a rigid rotational movement. This rotation of the cells is done by following an orbit. The shape of this orbit is of course dependent on the shear rate and the properties of the red blood cell [40]. This dynamics is called tumbling. In this configuration, it is shown that the dynamics is mainly controlled by the stress-free shape of the cytoskeleton [104].

In external fluid of large viscosities such as dextran solutions, when the shear

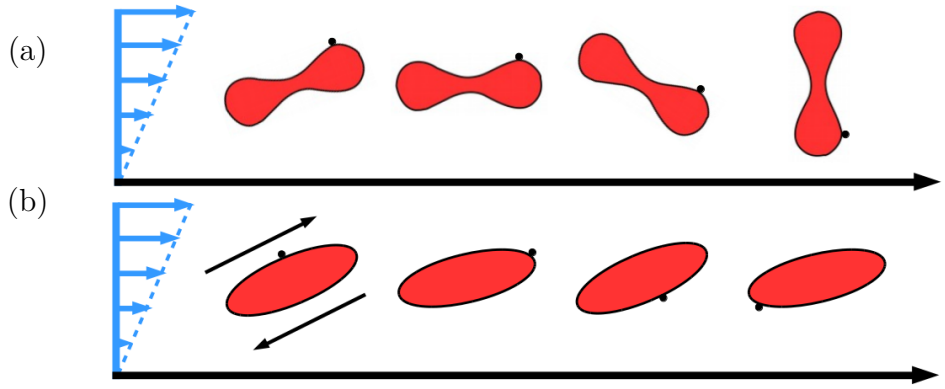

Figure 1.13: Representation of the (a) tumbling and (b) tank-treading motions at different times. Small black circles represent a bead fixed to the membrane to illustrate the circulation (in the case of tank treading) of the membrane around the cell.

rate is high enough, the globule enters a dynamics called tank treading. Under these conditions the membrane circulates around the cell (like tank caterpillars, hence the name). Moreover, the general orientation of the cell takes an angle of inclination with the direction of the flow and oscillates slightly. Tank treading is mainly defined by the frequency at which the membrane circulates around the cell, the angle of inclination that the cell takes with the flow and its deformation index. Here, the dynamics is controlled by viscous phenomena, related to either the external fluid, the internal fluid, or the membrane viscosity [56]. The impact of membrane viscosity on tank treading motion is of one of the objectives of this thesis and will therefore be detailed later in this work.

There is also an intermediate dynamics, where deformations are negligible, membrane circulation exists as in tank-treading, but the orientation angle strongly oscillates around an average position. This dynamics is called swinging and is mainly influenced by viscous effects related to external and internal fluids. It also depends on the elastic parameters of the membrane [1], such as the energy barrier associated with the non-spherical stress-free shape.

The transition regimes are particularly interesting, with intermittent regimes and hysteresis [1, 29, 40, 104, 108]. An example of transition between swinging and tumbling, is illustrated on the Fig. 1.14. Moreover, these transitions are also dependent on other parameters such as the confinement of the channel in which

the globule evolves [82]. Nevertheless, these transitions are also dependent on the mechanical parameters linked to the membrane, like the stress-free shape. Indeed, an RBC modeled with a spherical stress-free shape would always tank-tread if sheared in a viscous fluid due to the absence of energy barrier associated with membrane circulation. This leads to the conclusion that the values of the parameters allowing these transitions are not easy to quantify *et al.*so require investigations by experiment and simulation [58, 150].

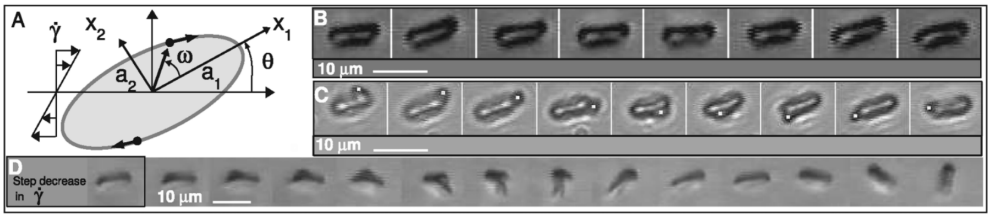

Figure 1.14: (a) Representation of the tank treading motion on a ellipsoid. (b) Images of swinging RBCs at different times. (c) Images of a bead that circulates with the membrane around the cell during the swinging motion. (d) Representation of the transition between the swinging motion and the tumbling motion of the RBC by imposing a step to the shear rate.

The ratio of the internal to the external fluid viscosities also controls the RBCs dynamics. In physiological conditions of viscosity, where the viscosity of the cytoplasm is typically 5 to 10 times higher than that of the external fluid, a sheared discocyte never tank-treads. Increasing the shear rate, the tumbling discocyte transitions to rolling[14, 40], then to the rolling stomatocyte (form displaying only one lobe and not two as for the discocyte) or even more complex forms such as trilobes and multilobes [87, 103]. It is important to understand that these forms are encountered in vitro but are also present in physiological conditions.

Although partial, diagrams representing the dynamics of RBC submitted to shear can be found in the literature [3, 103], the most complete one being presented by Mendez and Abkarian (2019) [105]. Indeed, the many parameters, of the RBC as well as of the external environment, lead to a very large number of possible situations and therefore potentially a large number of different dynamics [70].

These dynamics are observed on individual blood cells, but it is important to note that they have an impact on all phenomena related to blood, the most salient and known examples being the effect of cell properties on blood apparent viscosity

[23, 87]. For example, the self-organization of red blood cells in confined flows does not exist if the blood cells are rigidified [81]. The size of the cell-free layer, which represents the layer in a flow where there is no cell, is also dependent on the phenomenon of migration of the red blood cells, which is itself very dependent on the way in which the blood cells deform [51]. This leads also to different hematocrit profiles in small tubes depending on the viscosity ratio considered [142]. The alteration of the deformability of the blood cells can also have an impact on the rheology at the scale of the blood, as in the case of sickle cell disease [7, 127].

It is therefore well known that understanding the different dynamics of blood cells, due to the great diversity of observable behaviors and their impact on all blood-related phenomena, is one of the major challenges of hemorheology. To carry out this investigation, it is necessary to have a model allowing the fine measurement of the properties of red blood cells, and therefore to use numerical simulation in addition to the experimental approach. The interest of having a red blood cell model that can be manipulated under the different conditions mentioned in the literature is also highlighted.

1.4 Motivations

In this part, we will focus on the different observations that motivated this work on the viscous behavior of the red blood cell membrane, as well as its impact on the behavior of the complete red blood cell.

1.4.1 Experimental highlighting

Historically, the first attempts to characterize a viscous behavior concerning the membrane of RBCs date from the 1970s. These measurements were carried out using the micropipette technique, by observing the aspiration of the membrane in the micropipette as well as the relaxation of the membrane sucked in the micropipette until the cell returns to its initial configuration, after the membrane goes out of the pipette [24, 46]. This process is illustrated in Fig. 1.15. These measurements made it possible to obtain a first order of magnitude of a membrane surface viscosity, of the order of 10^{-3} cP.m. They also demonstrated that this viscosity value is much higher than the value measured on a simple bilipidic layer,

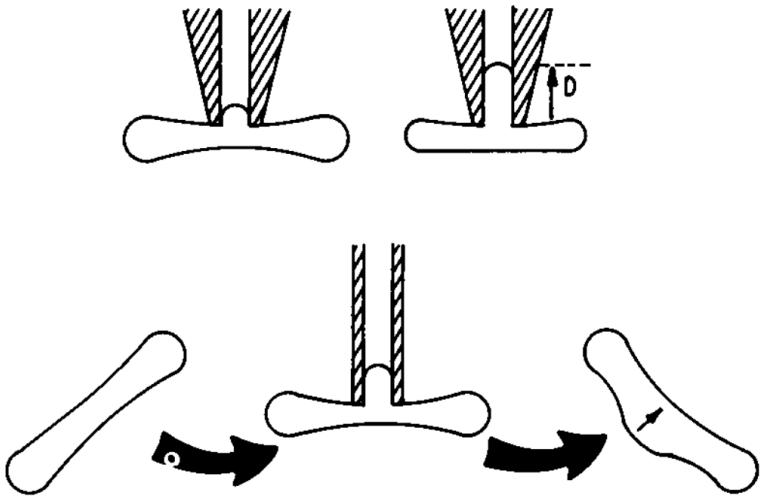

Figure 1.15: Figure showing the process of measurement of the membrane viscosity of the RBC's membrane using micropipette. Sketch from Evans and Hochmuth (1976) [46].

with a value of approximately 10^{-5} cP.m. That means that the source of the viscosity in the membrane involves the cytoskeleton.

Tran-Son-Tay *et al.* (1984) used a rheoscopy method to observe red blood cells tank-treading in shear flow. From data of elongation and tank-treading frequency, they estimated membrane viscosity by an inverse analysis [155], using the simplified model of a tank-treading ellipsoid of Keller and Skalak (1982) [84], resulting in a membrane viscosity between 10^{-4} cP.m and 10^{-3} cP.m. Similarly, this order of magnitude of viscosity was also confirmed in 2007 by the work of Liu *et al.* using a technique like ektacytometry [95]. These different measurements of the membrane viscosity, made at different times and using different methods, make it possible to give a confidence interval of the value representing the membrane viscosity of the red blood cell of the order of 10^{-4} cP.m to 10^{-3} cP.m.

The rheoscopy measurements used in the work of Tran-Son-Tay *et al.* (1984), in addition to confirming the order of magnitude measured during the micropipette experiments, found a notable impact of RBC age on the measured viscosity. Finally, these estimates of the membrane yielded a shear-thinning behavior (the viscosity tends to decrease as the shear increases), as illustrated on the results reproduced from Tran-Son-Tay *et al.* (1984), in Fig. 1.16.

This result constitutes, together with the work previously published by Chien *et al.* in 1978 [24], the first measurements showing a non-Newtonian behavior

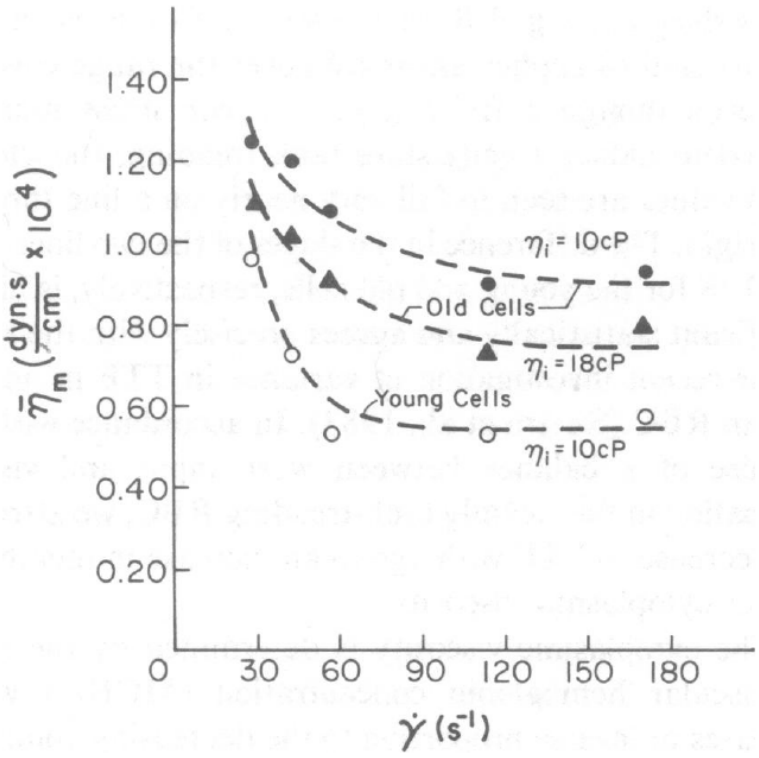

Figure 1.16: Plot of the different surface viscosity values measured on RBCs by Tran-Son-Tay *et al.* as a function of the shear rate. Membrane viscosity is estimated by matching the measured tank-treading frequency of red blood cell and values predicted by the model of Keller and Skalak [84].

of membrane viscosity. However, these results were obtained using a simplified analytical model [84], which features some assumptions whose impact on the results is impossible to assess (for instance, membrane elasticity is neglected, the shape of the cell is supposed to be an ellipsoid, the velocity field is simplified...).

However, another work concludes in favor of a more complex behavior of RBC membrane viscosity. This is the work of Puig de Morales Marinkovic *et al.* in 2007: by attaching ferromagnetic beads to red blood cells and plunging the assembly into an oscillating magnetic field (see Fig. 1.17), they measured the complex modulus of the RBC membrane. However, like the work previously carried out by Tran-Son-Tay *et al.*, many assumptions must be made before directly deducing a viscosity model from these measurements. Nevertheless, they highlight a potential complex behavior of membrane viscosity and point to a lack in the literature concerning this characteristic of RBC.

It has therefore been observed in the literature that membrane viscosity is

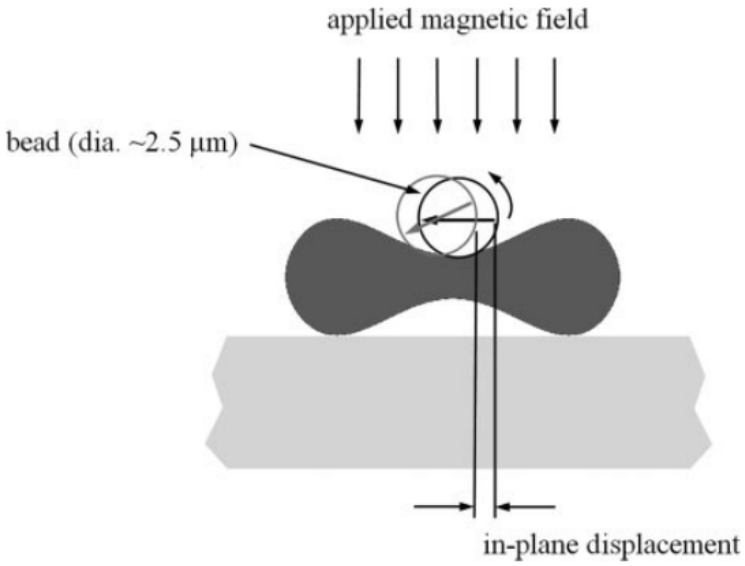

Figure 1.17: Sketch representing the experimental setup for the measurement of the complex modulus of the membrane. Image taken from Puig de Morales Marinkovic *et al.* (2007) [135].

indeed a measurable characteristic of RBCs, with 10^{-4} cP.m to 10^{-3} cP.m the plausible range. We have also been able to observe that it is difficult to accurately measure this quantity on red blood cells, due to the difficulty of disentangling geometrical, elastic and viscous effects, or membrane dissipation from internal fluid dissipation. We can even see that on simpler objects than red blood cells, namely capsules (droplets of liquids enclosed in polymer membranes), it was also very complex to measure this characteristic of the membrane. [80]. However, in addition, this quest for determining the 'exact' RBC membrane viscosity value is questioned by the studies suggesting a non-Newtonian behavior of the membrane.

1.4.2 Impact of the membrane viscosity on the RBC's dynamics: What do we know?

There are estimates of membrane viscosity in the litterature. But what do we know of its specific role in red blood cell dynamics? First, until recently it was often considered that membrane viscosity had a similar impact as internal fluid viscosity [100, 138]. Furthermore, a study on the tank treading behavior by Dodson & Dimitrakopoulos in 2010 suggest that the membrane viscosity can slow down tank-treading frequencies by a factor 2 [36]. Currently RBC's models rarely

considered membrane viscosity [66]. It leads that results on the specific role of membrane viscosity on RBC dynamics are sparse, and only date from the very last years [68, 102]. Moreover results on systems simpler than RBCs, such as capsules and vesicles, suggest possible trends for RBCs [6, 27, 150, 160]. A capsule is a drop of liquid surrounded by a deformable membrane. Works concerning the impact on the impact of membrane viscosity on different behaviors of capsules exist, in pure shear flow. It has been shown that the membrane viscosity has a significant impact on the orientation and the deformability of the capsules in shear flow [10, 118, 162]. An idea of the difference in shape that can cause the presence of membrane viscosity is shown Fig. 1.18. We see that the difference in shape is

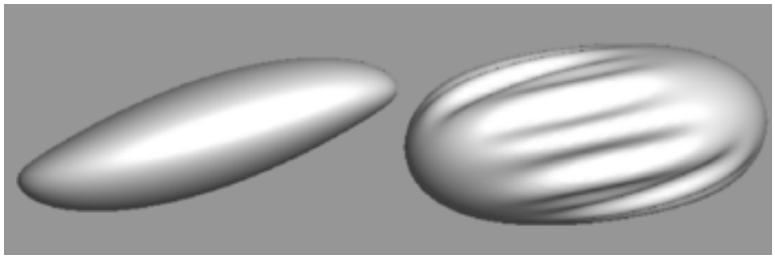

Figure 1.18: Two different simulated capsules in a shear flow, at the same shear rate, from Yazdani *et al.* (2013). On the left, the capsule is without membrane viscosity and on the right, the capsule membrane is viscous.

significant. There is therefore a real interest in clarifying this gray zone in the behavior of the RBC which is the impact of the viscosity of the membrane on the different dynamics and classic forms that it can encounter. This trend has been confirmed by the works that are currently coming out, dealing with the subject [68].

1.4.3 Goal and presentation of this work

The general objective of this thesis was to develop a computer code to model RBC dynamics, considering membrane viscosity. Obtaining such a model also amounts to reinforcing the realism and the robustness of the simulations by giving access, using the simulations, to new configurations, not accessible without considering the viscosity of the membrane. It also opens the way to simulations of more diverse pathological cases, by making it possible to model the impact of the diseases on the mechanical parameters of the membrane. In parallel to this, the idea is also to highlight the gaps in the literature concerning the models of viscosity

of the membrane of red blood cells and to enrich these models with the help of comparison between simulations and experimental works. Thus, thanks to a numerical model, we aim at learning about the behavior of the red blood cell by exploiting the combination with experimental results, which is expected in an improvement of the models.

At the root of all the applications and motivations listed above, there is the necessity to implement a model of membrane viscoelasticity in simulations of RBC dynamics. Numerous studies have been performed with YALES2BIO, the in-house flow solver developed at IMAG (http://imag.umontpellier.fr/~YALES2BIO) on the dynamics of single RBCs under shear [87, 103, 104, 105] or in hematological analyzers [153, 154], on the deformation of RBCs by optical tweezers [146] and on collective dynamics of RBCs in confined channel flows [81]. However, all those simulations neglect membrane viscosity. To implement membrane viscoelasticity in YALES2BIO, we chose a phenomenological approach to answer this problem. We first studied the existing rheological models and selected one of them for implementation in YALES2BIO. Then, we validated the implementation of the model using specifically designed elementary test cases. Finally, we studied different configurations of red blood cells under flow to assess the impact of membrane viscosity on the RBC behavior.

Chapter 2 will thus present the **physical framework** of the present work. In this part, we will detail the different fluid models, the behavior models of the membrane. In additional, physical modeling of the membrane viscosity will be detailed, as well as the important dimensionless numbers.

Subsequently, the **numerical framework** will be detailed in the **chapter 3**. Fluid solvers, discretization methods, as well as the management of fluid-structure interactions will be detailed. The general resolution algorithm will be presented and the implementation for passing from the mechanical law to the discretized law of the viscoelasticity of the membrane will be detailed. Finally, the validation case to test the good implementation of the membrane viscoelastic behavior will also be presented in this chapter.

Chapter 4 will be devoted to the different **applications**. This part will be separated into two applications: the study of strain configurations and the study of tank treading behavior. The first application studies in more detail the impact of membrane viscosity on a particular behavior of the red blood cell: tank-treading. The second part aims to show the interest of considering the membrane viscosity in the design phases of experimental devices for testing on RBCs. In this chapter

we aim at answering to the membrane viscosity's impact on the RBC's behavior on different setups.

Finally, **chapter 5** will gather the conclusions and perspectives of this work.

Chapter 2

Physical framework

Chapter contents

2.1 Introduction: a multiphysics problem 28
2.2 Fluids 29
2.2.1 Fluid model 29
2.2.2 Flow regime 29
2.2.3 Inner fluid properties 30
2.3 Red blood cell membrane model 31
2.4 Modeling the inviscid behavior of the RBC membrane 33
2.4.1 In-plane behavior: Hyperelasticity 33
2.4.2 Curvature forces 33
2.4.3 Stress-free shape 34
2.5 Membrane Viscoelasticity 35
2.5.1 Physical meaning of the viscoelasticity 35
2.5.2 Introduction to rheological representation and small strain viscoelastic model 37
2.5.3 Viscoelastic model for the membrane 40
2.6 Non dimensional numbers 43

2.1 Introduction: a multiphysics problem

The study of the behavior of the RBC involves the study of several elements, with, in the first place, the membrane of the RBC. This object has many mechanical properties that must be reproduced to predict the dynamics of the RBCs under flow, such as the resistance to curvature, the in-plane elasticity or the prestress distribution, determined by the reference shape of the RBC. All this makes the membrane alone a complex object to model, resulting in a combination of mechanical models, which will be presented in this part.
In addition, RBCs always evolve in a fluid and have their own internal fluidic cytoplasm, with their own density and viscosity parameters. These elements are obviously involved in the RBC deformation process and must be modeled. It is also not uncommon to experimentally study RBCs in different external fluids, having different viscosities, to allow access to a wider range of dynamics. The study of the deformation of RBCs is therefore a multiphysics problem leading to fluid-structure modeling.
Finally, all the elements that we have introduced here, once modeled, involve their own mechanical parameters. One of the challenges of modeling RBCs is the quest for representative values of these parameters, given the disparity of measurement methods and resulting values in the literature. This disparity in parameters has several sources. First, there is a disparity linked to the difficulty of measuring some mechanical parameters. Indeed, when we study the membrane of RBCs, we are talking about an object about 8μm in diameter and a thickness of a few tens of nanometers. The measurement of mechanical parameters in this context cannot be done on a dedicated sample, as for macroscopic materials, and must be done on the whole of the red blood cell [86]. The main idea is so to calibrate values of local parameters from non-local measurements. This may result in inaccuracies, depending on the assumptions made.
It is necessary to add to discrepancies the natural dispersion of the properties of the RBCs. Indeed, two RBCs do not have the same properties.

This is why the choice of parameter values is a major issue in the modeling of RBCs. The idea here is to have an idealized model, with parameter values that are representative and that give access to the different observable dynamics. In this part, the main idea is to describe each element that must be considered when studying RBC behavior. We will start by describing how the external and internal fluid are modeled. Then, we will describe the different models that are combined

to describe the membrane behavior. Finally, we will describe the membrane viscous behavior and detail choices that lead to the selection of the model used in this work.

2.2 Fluids

2.2.1 Fluid model

In this part, we will give the physical framework linked to the fluid model used in the study to model the external and internal fluids. First, the fluids are incompressible viscous fluids. This assumption is possible thanks to the Mach number $M_a = \frac{V}{a}$ with V the representative velocity of the considered object, here the RBC, and a the sound celerity in the medium considered (and at the given temperature). Of course, in every study considered the RBC velocity is infinitesimal compared to the sound velocity, so that compressibility effects are negligible. The fluid flows can thus be represented by the classical incompressible Navier-Stokes equations:

$$\begin{aligned} \frac{\partial \boldsymbol{u}}{\partial t} + \boldsymbol{\nabla}.(\boldsymbol{u} \otimes \boldsymbol{u}) &= -\frac{1}{\rho}\boldsymbol{\nabla} P + \boldsymbol{\nabla}.(\nu \boldsymbol{\nabla} \boldsymbol{u}) + \boldsymbol{\nabla}.(\nu (\boldsymbol{\nabla} \boldsymbol{u})^T) \\ \boldsymbol{\nabla} \cdot \boldsymbol{u} &= 0 \end{aligned} \tag{2.1}$$

with ρ the fluid density in kg.m^{-3}, $\boldsymbol{u}$ the velocity of the fluid in m.s^{-1}, p the pressure in Pa, $\boldsymbol{\nabla}$ the gradient operator, P the pressure in Pa and ν the fluid kinematic viscosity in m^2.s^{-1}.

2.2.2 Flow regime

Classically, to describe flow regimes in the literature, the Reynolds number is used. The Reynolds number is a non-dimensional number representing the ratio between inertial forces and viscous forces in a flow and it is classically expressed as:

$$Re = \frac{UL}{\nu} = \frac{\rho UL}{\mu} \tag{2.2}$$

with U a representative speed of the flow in m.s^{-1}, L a representative length in m, ν the fluid kinematic viscosity (or μ the dynamic viscosity in Pa.s). In this study and commonly in the RBC framework, the Reynolds number at the scale of the RBC is expressed as a function of the shear rate $\dot{\gamma}$ or the strain rate $\dot{\varepsilon}$ both in s^{-1}

and a the characteristic size of the RBC in m, to build a characteristic velocity difference at the scale of cell. As a characteristic size, one often uses the radius of the sphere having the same volume as that of an RBC. Using those parameters, the Reynolds number is expressed as:

$$Re = \frac{\rho\dot{\gamma}a^2}{\nu}; Re = \frac{\rho\dot{\varepsilon}a^2}{\nu} \tag{2.3}$$

The most relevant version of the Reynolds number depends on the configuration of interest. In general, when flows at the scale of the RBC are studied, the value is generally much smaller than unity, which means that viscous forces dominate at the scale of the cell, except for very fast flows that may be found in some biomedical devices [153]. The numerical method to solve those equations is presented in the chapter 3.

2.2.3 Inner fluid properties

RBC is filled by a inner fluid referred to as the cytosol. The dry content of the cytoplasm is mainly hemoglobin, to which oxygen may bind to be transported into the circulation and delivered to the organism. This hemoglobin solution has a concentration that varies among individuals and among cells, with the age of the cells [132]. The cytoplasm has a density ρ_{in} and dynamic viscosity μ_{in}. The goal of this part is to describe the model used in this study to consider the impact of the internal fluid on the RBC's behavior. Indeed, the inner fluid is known to play a major role in the RBC's behavior, as discussed in the introduction [3].

The density of the cytoplasm depends on its concentration in hemoglobin content, which is used to separate RBCs by their density. The typical density of the RBC is about 10% larger than that of water. First, the fact that densities are different is neglected in this study. It is important to note that, for some specific RBC's behavior such as sedimentation, this parameter is crucial. Generally, this hypothesis is made when short-time phenomena are studied, as in this work and is motivated by the fact that external viscous fluid increases the drag forces that leads to a decrease of the impact of the internal fluid [105]. In addition, many experiments use a suspending fluid with a higher density to limit sedimentation effect, such as Optiprep (iodixanol solution, Axis-Shield) [110, 140]. However, internal viscosity has to be taken into account to reproduce the full spectrum of the RBC's behaviors [3, 87, 105]. The value of internal fluid viscosity is dependent on the temperature and on the hemoglobin concentration [83, 112].

Concerning the impact of temperature, the cytosol viscosity decreases as the temperature increases [83]. It is important to note that in this work, every simulation is made to simulate behavior at temperature between 20°C and 25°C. In this range, the viscosity does not vary a lot. However, because of the major impact of the temperature on the inner fluid viscosity, it must be considered before simulating a case [19].

Hemoglobin concentration for a human RBCs is inside the range 320g.l^{-1} to 350g.l^{-1} and often taken as 330g.l^{-1} as a typical value. Literature values of viscosity as a function of the concentration of hemoglobin can be seen in Fig. 2.1. Using the earlier presented range leads to find an internal viscosity range between 5cP and 12cP. The discrepancies between different measurements shows that it is uncertainties remain regarding cytoplasm viscosity, which should be kept in mind when analyzing simulations with respect to experimental results.

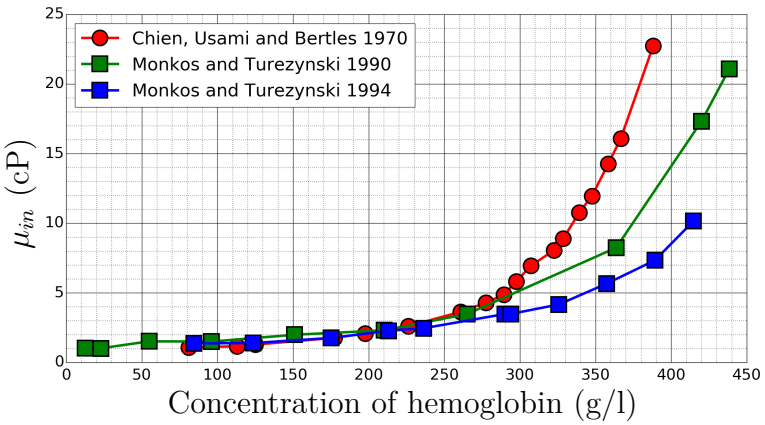

Figure 2.1: Plot of different RBC internal fluid viscosity as a function of the hemoglobin concentration curves found in the literature at 20°C for data from Chien *et al.* work, and 25.°C for Monkos *et al.* works.

2.3 Red blood cell membrane model

The RBC's membrane is a composite membrane composed by a lipid bilayer and a cytoskeleton attached together. Mechanically, the lipids of the bilayer may circulate, but the bilayer strongly resists any change of area: the lipid bilayer is thus responsible for the resistance to area changes of the membrane, but also to membrane bending [44]. In this bilayer is anchored the cytoskeleton, a spectrin network that gives the elastic shear resistance to the RBC membrane [3].

A way to model all the internal membrane mechanisms is to model every membrane component and to model RBCs as a multilayer model and multiscale computation [121, 125], or more simply to allow sliding between the lipid bilayer and the cytoskeleton [98]. One of the main interests of those kind of model is the multiscale aspect that enable to link macro-scale behavior with internal mechanisms. For example, it enables to identify the role of each part of the membrane for each behavior. In addition, it may be possible to quantify the detachment between the membrane and the cytoskeleton. Such approaches are certainly more realistic but more involved in terms of model complexity

A most common approach in the literature is to design a monolayer membrane that reproduces the RBC behavior at the macroscale. It is this kind of model that was used in this study. Their main advantage, in comparison with the multiscale approach, is that they are easier to use and calibrate. However, they do not allow relating macroscopic dynamics to protein/lipid behaviors. A common approach to model the membrane of a RBC suspended in a fluid is to assimilate the full membrane as a single surface and give to this infinitely thin object mechanical properties to reproduce the behavior of the whole membrane. The membrane is thus represented as an interface between two viscous fluids, with specific rheology linking its stress state to its deformation. Generally, stress from deformation is obtained as the sum of several sub-models accounting for different mechanical properties of the membrane [30, 36, 50, 62, 105, 123]. Here, we use and extend such a continuum framework, in which a hyperelastic model accounts for the in-plane resistances in the membrane while a curvature resistance is implemented separately. The model used in this study has been presented and validated in several publications [87, 107, 146], in cases without membrane viscosity.

In this chapter, the properties of the membrane will be described. In the numerical approach used in this thesis, RBC membrane used to be modeled as hyperelastic surfaces. This modeling level, which implementation was performed before the present thesis, is first described, in section 2.4. The non-dissipative behavior is first introduced, with the in-plane hyperelastic model (section 2.4.1) and the curvature model used (section 2.4.2), respectively. Then, the choice concerning the stress-free shape is presented in section 2.4.3. The stress-free shape is essential because it is necessary to compute the stress field of the membrane. Contrary to the non-dissipative behavior, membrane viscosity modeling was developed during this work. Membrane viscoelasticity is discussed in Section (2.5).

2.4 Modeling the inviscid behavior of the RBC membrane

2.4.1 In-plane behavior: Hyperelasticity

In this work, in-plane elastic resistances are modeled using the Skalak hyperelastic law [149]. This law controls the membrane shear and area change resistances. In the local strain eigen basis, it is expressed as:

$$\begin{aligned}
\sigma_{11} &= \frac{G_s}{\lambda_1\lambda_2}\left[\lambda_1^2(\lambda_1^2-1) + C(\lambda_1\lambda_2)^2\left[(\lambda_1\lambda_2)^2-1\right]\right] \\
\sigma_{22} &= \frac{G_s}{\lambda_1\lambda_2}\left[\lambda_2^2(\lambda_2^2-1) + C(\lambda_1\lambda_2)^2\left[(\lambda_1\lambda_2)^2-1\right]\right] \\
\sigma_{12} &= \sigma_{21} = 0
\end{aligned} \tag{2.4}$$

with σ_{ij} the components of the Cauchy stress tensor $\boldsymbol{\sigma}$ on the surface (in Pa.m), λ_i the eigenvalues of the transformation gradient tensor $\boldsymbol{F}$ expressed as $\boldsymbol{F} = \frac{\partial x(t)}{\partial x(0)}$, with $x(t)$ the current state and $x(0)$ denotes the stress-free state. G_s is the Skalak shear modulus (in Pa.m) and C the ratio between the area change modulus and the shear modulus. Because only in-plane behaviors are modeled here, the curvature behavior is modeled separately, the stress tensor here has only two dimensions. It means that, for a single element, stress and strain are considered in-plane. The membrane is generally considered as incompressible, due to the strong resistance to area change of the lipid bilayer. To ensure area incompressibility, a large value of C may be imposed. A value of the order of 100 is often found [6, 163], but higher values may be necessary in cases involving high stresses [153].

2.4.2 Curvature forces

The Skalak law only models in-plane changes. Resistance to bending is modeled separately, using a specific curvature law. The free-energy functional used in this study is the Helfrich energy [74, 167], expressed as:

$$W_b = \frac{E_b}{2}\int_S (2\kappa - c_0)^2 dS, \tag{2.5}$$

with W_b the bending energy of Helfrich in J, E_b the bending modulus in Pa.m, κ the mean curvature, c_0 the spontaneous curvature and S the membrane surface,

in m^2. Curvature forces generally prevent the formation of small folds on the RBC membrane, and of course determine the shapes of the RBC at rest [91].

2.4.3 Stress-free shape

As the cytoskeleton is seen as an elastic surface, local stresses in the membrane depend on its deformation with respect to a stress-free state. For the whole cell, a stress-free shape has thus to be imposed. Note that the resting shape of the red blood cell is not stress-free, as the equilibrium shape results from a balance between elastic forces and bending forces, which are non-zero for a discocyte. Of course, the level of membrane stress in the equilibrium configuration depends on the stress-free shape.

The stress-free shape of an RBC is not possible to measure directly. Consequently, it is generally inferred from simulation results and may be seen as a free parameter to needs to be adjusted to reproduce experimental results. However, shape memory of the RBC membrane has been demonstrated by Fischer [55], which means that the stress-free shape of the membrane is not a sphere, either the membrane elements differ spatially. In the model, the former assumption is made: the membrane mechanical moduli are supposed to be uniform, and shape memory associated with the stress-free shape.

The choice of the stress-free configuration has a major impact on the dynamics of current RBC model. An interesting example is the transition to the tank treading behavior of a RBC. Briefly, the tank treading behavior is a configuration where the RBC membrane circulates around the RBC (see chapter 4 for more information). It happens when the external viscosity is low enough and shear rates high enough [1]. For lower shear rates, flipping-like dynamics are observed [65, 104, 110]. The fact that the transition from flipping to tank-treading is shear-dependent [1] shows the role of elasticity. As a consequence, a spherical stress-free shape is not possible, as the RBC would never flip. When taking the discocyte's configuration as the stress-free shape, the transition to tank treading is obtained higher shear rates than those measured experimentally [124]. It shows the stress-free shape matters, especially in regimes where it controls the circulation (or not) of the membrane). The choice of the stress-free shape to choose has been a massive debate in the community. However, it seems that the literature on the subject converges, and leads to choose the stress-free shape as an oblate ellipsoid (ellipsoid with two of the three axis equals and the third axis smaller than the

two others) [30, 103, 124] of reduced volume higher than 0.95. Such values allow to reproduce the behaviors of RBCs under shear and are notably consistent with the stress-free shape inferred to predict the Stomatocyte-Discocyte-Echinocyte sequence of shapes at rest with different spontaneous curvature [91]. Such shapes are often characterized by the aspect ratio or by the reduced volume. The aspect ratio is the ratio between the smaller and the bigger axis of the oblate ellipsoid. The reduced volume V_0 is computed as $V_0 = \frac{V_{obl}}{A_{RBC}^{3/2}/3\sqrt{4\pi}}$, with V_{obl} the volume of the oblate ellipsoid and A_{RBC} the surface area of a normal RBC. We will now present the stress-free shape taken for all simulation presented in this work. It is an oblate ellipsoid with an aspect ratio of 0.9 and a reduced volume at $V_0 = 0.997$.

2.5 Membrane Viscoelasticity

The former section introduced classical models used in the RBC framework which constitute the basis of the current work, which consisted in complementing the model with membrane viscoelasticity. First, generality on the viscoelastic behavior will be presented to introduce vocabulary and general ideas. Then, the membrane viscous model used is this work will be described using a rheological model framework.

2.5.1 Physical meaning of the viscoelasticity

Viscoelasticity is the simplest dissipative behavior in the continuum mechanics framework. Where pure elasticity is only linked to the material strain and its state at a given moment, viscoelastic behavior is also dependent of the strain changes in time. This dependency is also exposed by the dimensions of the elastic and viscosity parameters: while the classical Young elastic modulus E is expressed in Pa, dynamic viscosity modulus η is expressed in Pa.s. Physically it could be seen as internal friction during the deformation of the material [101] that leads to energy dissipation. This dissipation can also be associated to a delay, or a phase shift between an input into the material (stress or strain) and the reaction of the material (the complementary of the input).

The link between the delay due to viscoelasticity and the energy dissipated by the viscous behavior can directly be highlighted on the simple case of sinusoidal stress imposed on an ideal viscoelastic material and by observing the stress-strain graph Fig. 2.2. Fig. 2.2(a) illustrates that, without dissipation, the input stress and

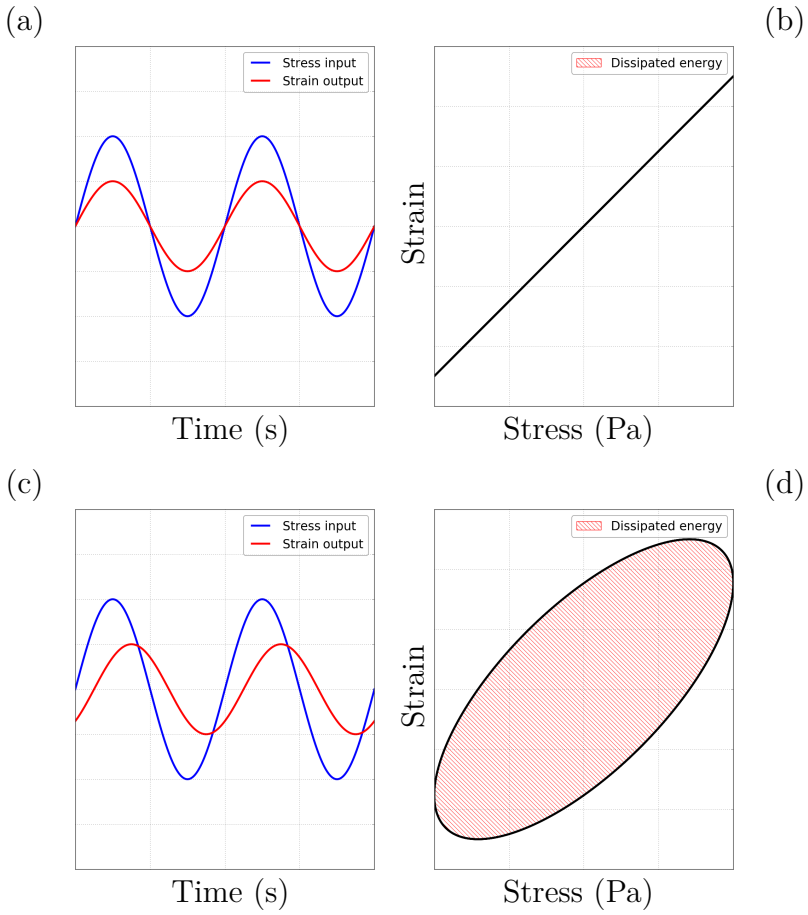

Figure 2.2: Representation of an experiment imposing a sinusoidal stress on an elastic and a viscoelastic material. (a) curves representing the input stress and the observed strain response, (b) the corresponding stress-strain graph, (c) the same input stress and the observed strain of the viscoelastic material and (d) the corresponding stress-strain graph.

the resulting strain are in phase. However, the viscoelastic material involves a delay that is highlighted in Fig. 2.2(c) as a phase shift. Observing the corresponding stress-strain graphs Fig. 2.2(b,d), the delay due to the viscous material leads to a hysteresis effect. Calculating the integral of the stress over a full cycle of charge leads to a non-zero area, whereas the pure elastic material that do not generate an area. This area has the dimension of an energy and is proportional to the dissipation due to the internal friction. It leads to measure this delay to quantify the internal dissipation of a material, and so its viscous behavior. There are multiple quantities that are linked to this delay. They can be recovery time/relaxation time of the material to a mechanical load, or phase shift between

an input and an output for more complex viscoelastic model. To go into more details, viscoelastic models are introduced in the next part.

2.5.2 Introduction to rheological representation and small strain viscoelastic model

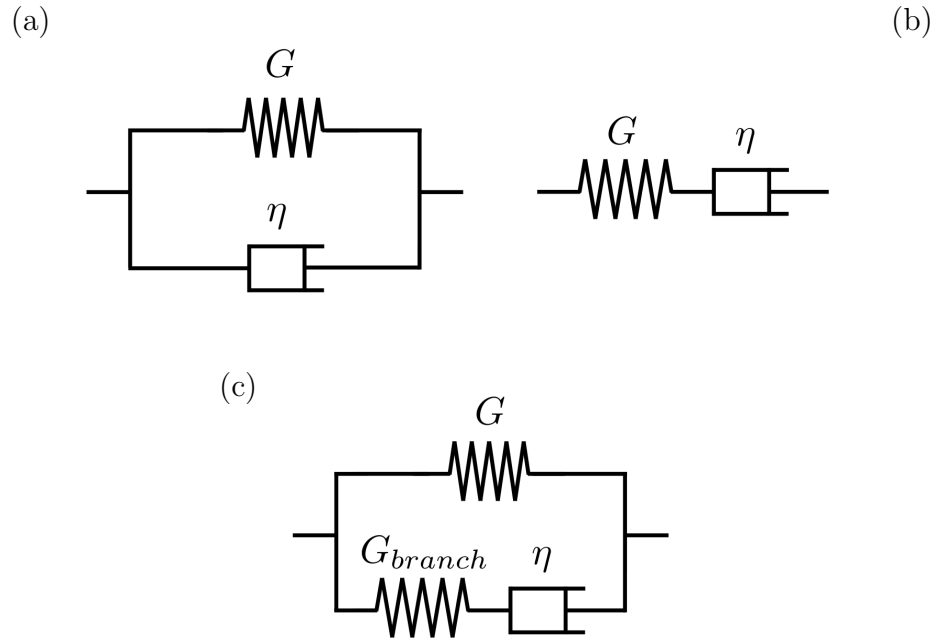

Figure 2.3: Three basic viscoelastic behavior laws represented by their rheological models in the small strain framework. (a) the Kelvin-Voigt model, (b) the Maxwell model and (c) the Zener model.

During this study, to facilitate visualization of the different viscoelastic laws, the rheological representation will be used. Rheological models are a convenient way to visualize mechanical laws. The main principle is to associate symbols representing basic mechanical behaviors in series or in parallel to obtain a more complex behavior law. In this introduction, every law is represented in the small-strain hypothesis. In this framework, the stress tensor is classically taken as the Cauchy stress tensor $\boldsymbol{\sigma}$ and the strain represented with the small-strain tensor $\boldsymbol{\varepsilon}$. The only rheological elements needed in this work are the springs and the dashpots. The springs are representative of the classical Hooke elastic law $\boldsymbol{\sigma} = G\boldsymbol{\varepsilon}$ in the small-strain framework (later we will define springs as hyperelastic springs that will follow hyperelastic behavior laws) and the dashpots represent linear

viscous laws $\boldsymbol{\sigma} = \eta\dot{\boldsymbol{\varepsilon}}$, with G here the young modulus (in Pa) and η the viscosity modulus (in Pa.s).

to represent a more complex behavior law, those rheological elements are put in parallel or in series. When elements are put in series, it means that the whole strain tensor is obtained by addition of the strains of the elements in series. On the other hand, elements put in parallel means that the stress of the resulting behavior law is obtained by summing the stresses in each of the element in parallel. Putting a spring and a dashpot in parallel leads to the Kelvin-Voigt model, (Fig. 2.3a). Summing stresses of the different elements directly leads to the following expression of the Kelvin-Voigt viscoelastic behavior law:

$$\boldsymbol{\sigma} = G\boldsymbol{\varepsilon} + \eta\dot{\boldsymbol{\varepsilon}}. \tag{2.6}$$

Using the same logic, putting a spring and a dashpot in series leads to the Maxwell viscoelastic behavior law, usually written in the following form:

$$\frac{\eta}{G}\dot{\boldsymbol{\sigma}} + \boldsymbol{\sigma} = \eta\dot{\boldsymbol{\varepsilon}}, \tag{2.7}$$

with $\dot{\boldsymbol{\sigma}}$ the derivative with respect to time of the stress tensor. In this form, the Maxwell behavior law clearly highlights the Maxwell characteristic time $t_c = \frac{\eta}{G}$. Because the term characteristic time is classically used to describe a viscoelastic behavior, to avoid misunderstanding, it is important to understand the physical interpretation of this time. Indeed, the characteristic time interpretation depends on the viscoelastic behavior law. For example, in the case of the Maxwell, the characteristic time represents the time for the stress to decrease of 66% of its initial value when the material undergoes an instantaneous deformation. However, for a material following the Kelvin-Voigt behavior law, the characteristic time $t_c = \frac{\eta}{G}$ represents the time for the strain to increase to 66% of the pure elastic deformation when the material undergoes an instantaneous stress. Also, to highlight the fact that the physics behind those two characteristic times are different, it is not possible to impose an instantaneous strain on a pure Kelvin-Voigt material, and impossible to impose an instantaneous stress on a pure Maxwell material. Replacing the viscous branch in the Kelvin-Voigt model by a Maxwell branch leads to construct the Zener model Fig. 2.3. The Zener behavior law can be written as:

$$\boldsymbol{\sigma} + \frac{\eta}{G_{branch}}\dot{\boldsymbol{\sigma}} = G\left(\boldsymbol{\varepsilon} + \frac{(G + G_{branch})}{G}\frac{\eta}{G_{branch}}\dot{\boldsymbol{\varepsilon}}\right) \tag{2.8}$$

Similarly, to before, two characteristic times can be calculated here. The first one $t_{c1} = \frac{\eta}{G_{branch}}$ is the Maxwell characteristic time and represent the same

physics. Moreover, the second characteristic time $t_{c2} = \frac{G+G_{branch}}{G} t_{c1}$ is like the Kelvin-Voigt characteristic time. Indeed, if G_{branch} tends to infinity, then t_{c2} tends to the Kelvin-Voigt characteristic time $\frac{\eta}{G}$. Finally, when G_{branch} tends to infinity, Eq. (2.8) tends to Eq. (2.6). This property of the Zener behavior law will be used during this work.

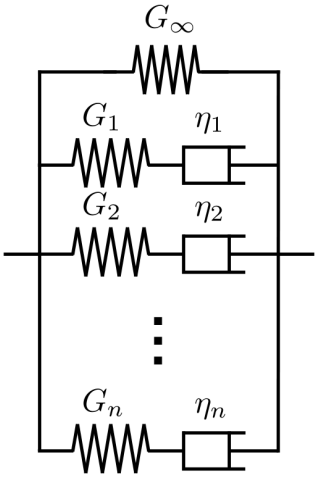

Figure 2.4: Rheological representation of the generalized Maxwell law with n the number of viscoelastic branch.

Finally, multiple characteristic times can be introduced in the system, by adding more Maxwell branches in parallel to the Zener model: it leads to the so-called generalized Maxwell model Fig. 2.4.

Interestingly, the Maxwell model has a general solution to compute stress for a given strain. This solution is obtained by integrating the differential equation Eq. (2.7). It leads to the following expression of the Maxwell stress:

$$\boldsymbol{\sigma}(t) = \int_0^t G e^{-\frac{t-t'}{\eta/G}} \dot{\boldsymbol{\varepsilon}}(t') dt'. \tag{2.9}$$

Thanks to this solution, because the generalized Maxwell model is just a sum of Maxwell model in parallel with a spring as a first branch, the general expression of the stress of a material following a Generalized maxwell model, using the same notation as in Fig. 2.4 leads to the following equation:

$$\boldsymbol{\sigma}(t) = G_\infty \boldsymbol{\varepsilon} + \sum_{i=1}^{n} \int_0^t G_i e^{-\frac{t-t'}{\eta_i/G_i}} \dot{\boldsymbol{\varepsilon}}(t') dt'. \tag{2.10}$$

The main interest of this model is that it enables to represent every viscoelastic law under the small strain hypothesis. Indeed, putting Maxwell branch enables the

selection of the frequencies where the material dissipates the most. It enables even to reproduce non-Newtonian behaviors (where the apparent viscosity depends on the mechanical load) like shear-thinning behaviors or shear-hardening. After this presentation of the classical viscoelastic models in the small strain framework, next section will present choices made to describe the membrane viscoelastic behavior.

2.5.3 Viscoelastic model for the membrane

Since the early 80's, the RBC's membrane is described as a viscoelastic material thanks to experimental measurements [24, 78]. However, even if the hyperelastic behavior of the membrane has been studied extensively [149, 164], the viscous aspect of the membrane behavior has not received the same interest from the community. Always in the early 80's, experiments trying to measure membrane viscosity are done using multiple techniques as the study of recovery of the red blood cell membrane from micropipette aspiration [24] or rheoscopic techniques combined with the Keller and Skalak theoretical model [84, 155]. However, since those works, experiments trying to increase knowledge on the RBC's membrane viscosity are rare and do not propose a mechanical model richer than a Kelvin-Voigt like model. The only work that we found that propose another model is the work done by Puig-de-Morales-Marinkovic et al, using ferromagnetic microbeads fixed to the membrane inside a magnetic field to apply stretch at different stretch locally on the membrane [135]. Even if advances thanks to this work are big by measuring a nonlinear viscous behavior of the membrane, the work to transpose the measure of viscosity effect done thanks to this experiment to the membrane mechanical viscoelastic behavior law is not done yet.

The design of complex membrane viscoelastic models involving multiple characteristic times is depending on the experimental measurements of the membrane viscosity. The more the membrane viscosity will be inspected, the more complex and precise membrane viscous models will be. This lack of knowledge about membrane viscosity leads to model the membrane viscoelasticity with a simplistic model. Statements made by literature on the model suggest that this simplistic model is a Kelvin-Voigt like behavior law, suggesting the addition of viscous stress and hyperelastic stress [78]. Research of such a model in publications about numerical simulations of RBCs and capsules leads to three main works [68, 90, 162]. For both of those publications, the same viscoelastic model is used to represent the membrane. This model is based on an existing viscoelastic model used in the

commercial simulation software ABAQUS©. It leads that publications using this model to briefly present the model and cite the ABAQUS© manual. To this day and to our knowledge, it does not exist yet a document that details the physical framework of this mechanical model and the hypothesis behind this model. The model is based on the hypothesis of stress addition between the viscous and the hyperelastic stresses. The choice of the model was therefore mainly based on 2 criteria. The first and that, not knowing the real behavior of the material, we wanted a simple model based close to the Kelvin-Voigt model. The second criterion was that we wanted to be able to quickly validate the model with others works, and quickly inspect impact of such a behavior on the RBCs deformability. Since the simulation works modeling the membrane viscosity are not numerous, we have therefore made the same choice of modeling as the works cited above, namely those of Yazdani *et al.* [162], Li *et al.* [90] and Guglietta *et al.* [68], based on the commercial computer code ABAQUS ©. This model is based on the work of Simo [147]. In this work, Simo describes a fully three-dimensional finite-strain viscoelastic damage model. First, the damage part of the law is not considered here This model enables the local additive split of the stress tensor into initial and nonequilibrium parts. As it is written in Simo's work, this characteristic leads to a free-energy form that generalizes the linear viscous model presented previously. This model also enables the decomposition of the stress tensor into an uncoupled deviatoric part and a hydrostatic part. Finally, it enables the viscous relaxation to recover to general finite elasticity. This bulk of characteristics corresponding to all the needs that were described earlier motivates the literature to use this model.

The third characteristic interesting for this work in Simo's work is the recovery to a general finite elasticity behavior. It was in particularly tested during Simo's work using classical rubber hyperelastic law as neo-Hookean or Mooney-Rivlin laws and is thus supposed to work the same with the Skalak model. Moreover, Simo's model is a fully 3D finite strain model. However, in the RBC membrane framework where is located this study, the membrane is represented by a 3D mesh composed of 2D triangular elements, on which in-plane stresses and curvature resistance are treated separately. Moreover, Simo's model is a fully 3D finite strain model. However, in the RBC membrane framework where is located this study, the membrane is represented by a 3D mesh composed of 2D triangular elements. Those 2D elements follow a mechanical behavior law that ensures the reproduction of the in-plane strain behavior, and a bending resistance law ensures the reproduction of the curvature behavior separately. First, viscosity linked

to the curvature was neglected. Then, the result that generalizes linear viscous behavior in finite strain is used but in a plate theory framework. It supposes that Simo's law can also be expressed in this framework and leads to the same characteristics as mentioned before. Finally, because of the quasi-incompressibility of the RBC membrane, it has been decided to neglect the viscosity linked to the hydrostatic part of the stress tensor. It means that only the deviatoric part of the stress tensor is described using a viscoelastic behavior. This concludes to present the mechanical framework where this viscoelastic behavior law exists. As said before, the framework could still be improved in terms of fundamental mechanics. However, the description of the existing framework and of its limitations had not been made. By doing that work, we hope that it will highlight lack of knowledge and will motivate future works to consolidate it. Unfortunately, it could not be performed within this thesis. Now that a framework enabling the generalization of small strain viscoelastic model is defined, let's define the rheological model that was implemented to achieve this study. The literature highlights the fact that a direct implementation of a Kelvin-Voigt model in finite strain leads to numerical instability [162]. To our knowledge, this result has not been proved yet. However, to avoid numerical instability, the classical way for the few models present in the literature is to implement a more versatile model that is enabled to converge to a Kelvin-Voigt behavior under some conditions. The classic implemented model that is a fully generalized Maxwell model in a finite strain framework that converges to a Skalak behavior law once the viscous stress is relaxed and uses Maxwell viscoelastic branch combining a finite strain Hooke spring and linear viscosity. The finite strain Hooke law is defined as Eq. (2.11):

$$\begin{aligned} \sigma_{11} &= \frac{G_H}{1-\nu_H}\left[\lambda_1^2 - 1 + \nu_H(\lambda_2^2 - 1)\right] \\ \sigma_{22} &= \frac{G_H}{1-\nu_H}\left[\lambda_2^2 - 1 + \nu_H(\lambda_1^2 - 1)\right] \\ \sigma_{12} &= \sigma_{21} = 0 \end{aligned} \tag{2.11}$$

with G_H the Young modulus of the Hooke behavior law and μ_H the Poisson coefficient. However, the Maxwell generalized model was used is this study only to converge in a Kelvin-Voigt model. To do that, the model was defined with only one viscoelastic branch, as seen in Fig. 2.5, with G_∞ the Skalak shear modulus of the membrane. Put a big enough G_H leads the model to converge in a Kelvin-Voigt

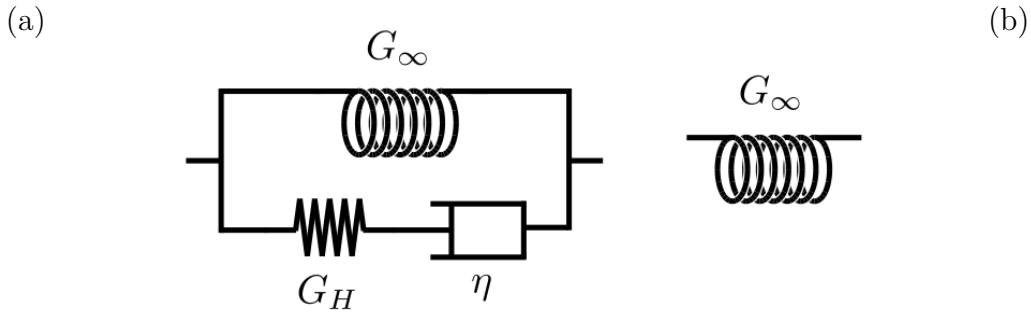

Figure 2.5: Rheological model of the behavior law used in this study. The curved springs represent the Skalak hyperelastic law and the straight spring the Hooke law. Rheological model for the deviatoric (a) and the hydrostatic part (b).

model with only the curved spring and the viscous damper in parallel. That result has only been empirically tested and no rules has been found for now. Now that all parameters were presented, the final tools present in the RBC framework to describe RBC behavior are non-dimensional numbers obtained thanks to the model parameters. It is presented in the next part.

2.6 Non dimensional numbers

In this part, the main goal is to present the different non-dimensional numbers used to describe the configurations of RBCs under flow. First, some parameters are linked to the fluid nature: the density of the internal and external fluids, ρ_{int} and ρ_{ext} (in kg.m^{-3}) and μ_{int} and μ_{ext}, in Pa.s, viscosity values of the internal and external fluids, respectively. This leads to two non-dimensional numbers, the density ratio $\frac{\rho_{int}}{\rho_{ext}}$, which is set to 1.0, the density differences between the cytoplasm and the external medium being neglected, and the viscosity ratio:

$$\lambda = \frac{\mu_{int}}{\mu_{ext}}. \tag{2.12}$$

The viscosity ratio is classically considered to be of the order of 5.0-10.0 *in vivo*, but *in vitro* experiments may involve the resuspension of the cells in a different medium, like phosphate-buffered saline (PBS) or dextran solutions, that have a viscosity different from that of plasma. Consequently, the viscosity ratio λ will be one the the variable parameters in the study.

By introducing characteristic scales linked to the flow itself, such as fluid velocity V (in m.s^{-1}) or shear rate $\dot{\gamma}$ or strain rate $\dot{\varepsilon}$ (both in s^{-1}), the Reynolds

number Re can be defined as previously by Eq. (2.13). It represents the ratio between the forces of convection and the forces of diffusion of the fluids, and is calculated as:

$$Re = \frac{\rho\dot{\gamma}a^2}{\nu}; Re = \frac{\rho\dot{\varepsilon}a^2}{\nu}. \tag{2.13}$$

Re number is generally low in the context of studies of phenomena at RBC scale.

Then, the other parameters are related to the RBC itself. First, single cells will be considered, so that the volume fraction will always be negligible. Then the geometry of the RBC is associated a volume of V of $94\mu\text{m}^3$ and a surface area S of $135\mu\text{m}^2$. One can also introduce a characteristic size of the red blood cell, denoted by a, which is a few microns. Typically, a is the radius of the sphere having the same volume as the RBC, which lead to $a = 2.82\mu\text{m}$.

Then, there are parameters linked to the RBC's non-dissipative behavior. The membrane bending resistance introduces the curvature modulus E_b (in J). Then the hyperelastic behavior of the RBC introduces the shear modulus G_s and the area modulus E_{area} (both in Pa). These parameters allow the construction of several dimensionless numbers. Let's first introduce $C = \frac{E_b}{E_{area}}$, the number comparing the shear modulus and the area change modulus.
Similarly, a relevant number within the RBC study framework is the Föppl-von Karman number α. This number is calculated as $\alpha = \frac{a^2 G_s}{E_b}$. This number makes it possible to know, at the RBC scale, which forces dominate the behavior of the RBC between the in-plane forces and the bending forces [103]. In the cases that we present in this study, α is of the order of 500, showing that it is the forces in the plane that dominate.
A dimensionless number particularly used in the study of RBCs is the capillary number Ca. Ca define the ratio between the viscous stresses applied by the fluid to the membrane and the membrane response to stress. It is expressed as:

$$Ca = \frac{\mu_{ext}\dot{\gamma}a}{G_s}. \tag{2.14}$$

Finally, this work introduces a dissipative behavior in the membrane represented by a membrane viscosity model. This model introduces two parameters: the branch shear modulus G_H (in Pa) and the membrane viscosity modulus η (in Pa.s.m). We can use the ratio $\frac{G_H}{G_s}$ to control the behavior of the model. Thus, if this ratio is large, then the model will tend towards the behavior of a Kelvin-Voigt model. Conversely, a very small ratio will tend to minimize the impact of viscosity on commonly observed phenomena. The membrane viscosity parameter η enables

the introduction of a new non dimensional number known as the Boussinesq number Bq. This number represents the ratio of viscosity between a fluid and the membrane and is expressed as:

$$Bq = \frac{\eta}{a\mu_{fluid}}. \tag{2.15}$$

In our case, the Boussinesq number may be expressed either using the internal fluid viscosity (Bq_{int}) or the external fluid viscosity, (Bq_{ext}). In this study, we choose to use Bq_{int} because it does not depend of the external environment and is thus viewed as an intrinsic number characterizing the RBC itself. However, both Boussinesq numbers are used in the literature [68].

Chapter 3

Numerical framework

Chapter contents

3.1 Introduction 48
3.2 Flow solver 49
3.2.1 The Navier-Stokes equations and their time advancement . 49
3.2.2 Space discretization method: Finite Volume Method . . . 50
3.2.3 Variable viscosity 54
3.3 Fluid-structure interaction: Immersed Boundary Method 55
3.3.1 Coupling: General algorithm 55
3.3.2 Coupling: Interpolation and Spreading 56
3.3.3 In-plane stress: Hyperelasticity 59
3.3.4 From element stress to nodal forces 60
3.3.5 Curvature forces 62
3.4 Implementation of the membrane viscosity 63
3.4.1 Implementation 63
3.4.2 Validation: small strain cases 66
3.4.3 Convergence Zener to Kelvin-Voigt 69
3.5 Validation: capsule under shear flow 70

3.1 Introduction

There is a multitude of studies of the mechanical behavior of RBC through numerical simulation. However, these studies have not yet made it possible to establish an ideal numerical framework for the study of such a problem, each method offering its own set of pros and cons. It is therefore necessary for a numerical study of RBCs to present in detail the different methods used to represent the RBC as well as its environment.
As part of this study, the modeling choices were to model both the fluid and the membrane in the form of two distinct meshes. Thus, the fluid is modeled in the form of a volume mesh. The RBC, on the other hand, is represented only by its surface, meshed by 2D triangles. The method used is a one-fluid method with variable properties: inside the 2D surface, the fluid elements have the properties of the cytosol; outside, they have the properties of the suspending medium. It is necessary to introduce the methods to solve the fluid flow, the calculation of the stresses and the mechanical deformations of the membrane, as well as the communication between the 2 meshes. This is the purpose of this part.
To do this, we will first present the methods used which constitute the fluid solver used in this study. Next, the method of solving the Navier Stokes equations, the bases concerning the Finite Volume Method, and the method used to consider the internal viscosity of the RBC used in this study will be presented.
Subsequently, we will present the fluid-structure coupling methods used. This will detail the coupling method used in this study, namely the Immersed Boundary Method. These first two parts have already been widely presented in previous studies and have not been developed specifically in the context of this thesis. The third part here aims to present the approach for implementing membrane viscosity within the calculation methods already presented. Being specifically developed during this thesis work, the implementation and the validation process will be presented.

All the numerical simulation work present in this study was carried out using the YALES2BIO computer code. YALES2BIO is a multiphysics numerical calculation software based on the massively parallel code YALES2. Its purpose is to be a tool allowing the physical study of blood at different scales, ranging from thrombosis phenomena to blood flow on a macroscopic scale. It is mainly composed of a fluid solver solving the Navier-Stokes equations. In the context of RBC simulations, the fluid-structure interaction is carried out using the Immersed

Boundary Method (IBM). This computer code has already been the subject of numerous publications [106]. The tools presented are therefore an integral part of this computer code. Most non-viscosity modeling aspects were present before this work. Thus, the fluid solver, the fluid structure interaction and the membrane viscosity implementation are presented separately.

3.2 Flow solver

3.2.1 The Navier-Stokes equations and their time advancement

The purpose of this section is to present the resolution method used in our study to solve the Navier-Stokes equations. For the sake of reading comfort, although already present Eq. (2.1), we will recall them briefly. The Navier-Stokes equations can be written as follows:

$$\begin{aligned} \frac{\partial \boldsymbol{u}}{\partial t} + \boldsymbol{\nabla}.(\boldsymbol{u} \otimes \boldsymbol{u}) &= -\frac{1}{\rho}\boldsymbol{\nabla} P + \boldsymbol{\nabla}.(\nu \boldsymbol{\nabla} \boldsymbol{u}) + \boldsymbol{\nabla}.(\nu (\boldsymbol{\nabla} \boldsymbol{u})^T) \\ \boldsymbol{\nabla} \cdot \boldsymbol{u} &= 0 \end{aligned} \tag{3.1}$$

with ρ the fluid density in kg.m^{-3}, $\boldsymbol{u}$ the velocity of the fluid in m.s$^-$1, p the pressure in Pa, $\boldsymbol{\nabla}$ the gradient operator, P the pressure in Pa and ν the fluid kinematic viscosity in m^2.s^{-1}. Note that although high-Reynolds number flows are not considered in this study, RBCs may face extreme stresses leading to non-zero Reynolds number flows even at the scale of the RBC, so that the full incompressible Navier-Stokes equations need to be solved [153].

In our case, these equations are advanced using a so-called prediction-correction method developed by Chorin in 1968 [26]. From the velocity known at the time t^n,the idea is to first calculate a velocity that does not necessarily satisfy the zero-divergence condition, by just advancing the momentum equation. Then, in a second step, pressure P is used to impose a corrective term making it possible to calculate a speed $\boldsymbol{u}^{n+1}$, satisfying the zero divergence condition.
to represent the time derivative term, YALES2BIO uses a Runge-Kutta scheme

of order 4. However, this part having a purely didactic purpose, for the sake of simplicity, we use the explicit Euler scheme in the equations to illustrate Chorin's solution method.
Semi-discretizing equation Eq. (3.1) in time leads to the following equation relating that the velocity at times t^n and t^{n+1}:

$$\frac{\boldsymbol{u}^{n+1}-\boldsymbol{u}^n}{\Delta t} = -\boldsymbol{\nabla}.(\boldsymbol{u}^n \otimes \boldsymbol{u}^n) - \frac{1}{\rho}\boldsymbol{\nabla} P^{n+1} + \boldsymbol{\nabla}.(\nu \boldsymbol{\nabla}\boldsymbol{u}^n) + \boldsymbol{\nabla}.(\nu(\boldsymbol{\nabla}\boldsymbol{u}^n)^T) \quad (3.2)$$

with $\boldsymbol{u}^{n+1}$,$\boldsymbol{u}^n$ the velocity at a time of t^{n+1} and t^n, respectively, and P^{n+1} the pressure at the time t^{n+1}.
It is not possible to solve both velocity and pressure as it is. Chorin's method consists in advancing the velocity field in time without the pressure term to calculate a prediction velocity u^* which is not necessarily divergence-free:

$$\frac{\boldsymbol{u}^{*}-\boldsymbol{u}^n}{\Delta t} = -\boldsymbol{\nabla}.(\boldsymbol{u}^n \otimes \boldsymbol{u}^n) + \boldsymbol{\nabla}.(\nu \boldsymbol{\nabla}\boldsymbol{u}^n) + \boldsymbol{\nabla}.(\nu(\boldsymbol{\nabla}\boldsymbol{u}^n)^T) \quad (3.3)$$

Subtracting Eq. (3.3) to Eq. (3.2) leads to:

$$\frac{\boldsymbol{u}^{n+1}-\boldsymbol{u}^{*}}{\Delta t} = -\frac{1}{\rho}\boldsymbol{\nabla} P^{n+1} \quad (3.4)$$

We can then apply the divergence operator on each side of Eq. (3.4):

$$\begin{aligned} \boldsymbol{\nabla}.\frac{\boldsymbol{u}^{n+1}}{\Delta t} - \boldsymbol{\nabla}.\frac{\boldsymbol{u}^{*}}{\Delta t} &= -\boldsymbol{\nabla}.\left(\frac{1}{\rho}\boldsymbol{\nabla} P^{n+1}\right) \\ &= -\frac{1}{\rho}\boldsymbol{\nabla}.(\boldsymbol{\nabla} P^{n+1}) \end{aligned} \quad (3.5)$$

We can now use the divergence-free property of $\boldsymbol{u}^{n+1}$ to obtain an equation between the predicted velocity and the pressure at time t^{n+1}. It is a Poisson equation for pressure:

$$\frac{1}{\rho}\boldsymbol{\nabla}.(\boldsymbol{\nabla} P^{n+1}) = \frac{1}{\Delta t}\boldsymbol{\nabla}\boldsymbol{u}^{*} \quad (3.6)$$

This system can now be solved using an iterative solver of the type of conjugate gradient (CG). The method used in the YALES2BIO code is the Deflated Preconditioned Conjugate Gradient method (DPCG) [5, 99].

3.2.2 Space discretization method: Finite Volume Method

The Finite-Volume Method (FVM) used for the spatial discretization of the equations is the subject of this part.
This method consists in defining the fluid domain as the sum of different control volumes Ω_i. Each volume is enclosed by a surface composed of several faces between control volumes. $S_{i,j}$ is the face separating Ω_i and Ω_j. We note $\delta\Omega_i$ the outer boundary of Ω_i, representing the union of these faces $S_{i,j}$. The values of the macroscopic quantities to be calculated, namely P and $\boldsymbol{u}$ are located at the center of mass $\boldsymbol{x}_i$, vector position relative to the global reference of the center of mass of the control volume Ω_i.
The FVM principle thus consists in expressing all the interesting physical quantities in the form of volume integral over each control volume Ω_i.
As a reminder, the time discretization yields a set of 3 equations (Eq. (3.3), Eq. (3.4) and Eq. (3.6)) allowing us to determine the quantities $\boldsymbol{u}^{n+1}$ and P^{n+1}, with$\boldsymbol{u}^*$ as an intermediate velocity. To express these equations in the FVM formalism, each of them is integrated over a control volume Ω_i, of boundary $\delta\Omega_i$. First, integrating Eq. (3.3) results in:

$$\begin{aligned}
&\frac{1}{\Delta t}\int_{\Omega_i}(\boldsymbol{u}^*-\boldsymbol{u}^n)dV = \int_{\Omega_i}\left(-\boldsymbol{\nabla}.(\boldsymbol{u}^n\otimes\boldsymbol{u}^n)+\boldsymbol{\nabla}.(\nu\boldsymbol{\nabla}\boldsymbol{u}^n)+\boldsymbol{\nabla}.(\nu(\boldsymbol{\nabla}\boldsymbol{u}^n)^T)\right)dV\\
\leftrightarrow\ &\frac{1}{\Delta t}\left(\int_{\Omega_i}\boldsymbol{u}^*dV-\int_{\Omega_i}\boldsymbol{u}^ndV\right) = -\int_{\Omega_i}\left(\boldsymbol{\nabla}.(\boldsymbol{u}^n\otimes\boldsymbol{u}^n)\right)dV+\int_{\Omega_i}\left(\boldsymbol{\nabla}.(\nu\boldsymbol{\nabla}\boldsymbol{u}^n)\right)dV\\
&\qquad\qquad+\int_{\Omega_i}\left(\boldsymbol{\nabla}.(\nu(\boldsymbol{\nabla}\boldsymbol{u}^n)^T)\right)dV
\end{aligned} \tag{3.7}$$

Using the Green-Ostrogradski formula, it is possible to express Eq. (3.7) by involving surface integrals over boundaries:

$$\begin{aligned}
\frac{1}{\Delta t}\left(\int_{\Omega_i}\boldsymbol{u}^*dV-\int_{\Omega_i}\boldsymbol{u}^ndV\right) &= -\int_{\delta\Omega_i}(\boldsymbol{u}^n\otimes\boldsymbol{u}^n)\,d\boldsymbol{S}+\int_{\delta\Omega_i}(\nu\boldsymbol{\nabla}\boldsymbol{u}^n)\,d\boldsymbol{S}\\
&\quad+\int_{\delta\Omega_i}\left(\nu(\boldsymbol{\nabla}\boldsymbol{u}^n)^T\right)d\boldsymbol{S}\\
\leftrightarrow\ \frac{1}{\Delta t}\left(\int_{\Omega_i}\boldsymbol{u}^*dV-\int_{\Omega_i}\boldsymbol{u}^ndV\right) &= -\sum_j\int_{S_{i,j}}(\boldsymbol{u}^n\otimes\boldsymbol{u}^n)\,d\boldsymbol{S}+\sum_j\int_{S_{i,j}}(\nu\boldsymbol{\nabla}\boldsymbol{u}^n)\,d\boldsymbol{S}\\
&\quad+\sum_j\int_{S_{i,j}}\left(\nu(\boldsymbol{\nabla}\boldsymbol{u}^n)^T\right)d\boldsymbol{S}
\end{aligned} \tag{3.8}$$

with $d\boldsymbol{S}$ the area element times the normal vector to $S_{i,j}$.
Similarly integrating Eq. (3.4) and Eq. (3.6) yields Eq. (3.9) and Eq. (3.10), respectively:

$$\frac{1}{\Delta t}\int_{\Omega_i}\left(\boldsymbol{u}^{n+1}-\boldsymbol{u}^{*}\right)dV \;\; = -\frac{1}{\rho}\sum_j\int_{S_{i,j}} P^{n+1}d\boldsymbol{S} \tag{3.9}$$

$$\frac{1}{\rho}\sum_j\int_{S_{i,j}} \boldsymbol{\nabla} P^{n+1}d\boldsymbol{S} \;\; = \frac{1}{\Delta t}\sum_j\int_{S_{i,j}} \boldsymbol{u}^{*}.d\boldsymbol{S}. \tag{3.10}$$

It is seen that Eq. (3.8), Eq. (3.9) and Eq. (3.10) involve sums over the sub-surfaces of the boundary of the control volumes. We will rename these terms for better readability, as well as to more easily relate them to their meaning. We therefore define the following operators:

$$\mathcal{C}(\boldsymbol{u},\boldsymbol{u}) = \sum_j\int_{S_{i,j}} \left(\boldsymbol{u}^n\otimes\boldsymbol{u}^n\right)d\boldsymbol{S} \tag{3.11}$$

$$\mathcal{G}(P) = \sum_j\int_{S_{i,j}} Pd\boldsymbol{S} \tag{3.12}$$

$$\mathcal{D}(\boldsymbol{u}) = \sum_j\int_{S_{i,j}} \boldsymbol{u}.d\boldsymbol{S} \tag{3.13}$$

$$\mathcal{L}(P) = \sum_j\int_{S_{i,j}} \boldsymbol{\nabla} P.d\boldsymbol{S} \tag{3.14}$$

$$\mathcal{L}_{cv}(\nu,\boldsymbol{u}) = \sum_j\int_{S_{i,j}} \nu\boldsymbol{\nabla}\boldsymbol{u}d\boldsymbol{S} \tag{3.15}$$

$$\mathcal{L}^T_{cv}(\nu,\boldsymbol{u}) = \sum_j\int_{S_{i,j}} \nu\left(\boldsymbol{\nabla}\boldsymbol{u}\right)^T d\boldsymbol{S}. \tag{3.16}$$

$\mathcal{C}$ represents the convective term of the Navier-Stokes equations, $\mathcal{G}$ the pressure gradient term in the right-hand side of Eq. (3.4) and $\mathcal{D}$ the divergence operator. $\mathcal{L}$ is the laplacian operator. $\mathcal{L}_{cv}$ and $\mathcal{L}^T_{cv}$ are involved in the viscous part of the Navier-Stokes equations Eq. (3.1).
These notations allow Eq. (3.8),Eq. (3.9) and Eq. (3.10) to be rewritten as Eq. (3.17), Eq. (3.18) and Eq. (3.19), respectively:

$$\frac{1}{\Delta t}\left(\int_{\Omega_i}\boldsymbol{u}^{*}dV - \int_{\Omega_i}\boldsymbol{u}^{n}dV\right) = -\mathcal{C}(\boldsymbol{u}^n,\boldsymbol{u}^n) + \mathcal{L}_{cv}(\nu,\boldsymbol{u}^n) + \mathcal{L}^T_{cv}(\nu,\boldsymbol{u}^n) \tag{3.17}$$

$$\frac{1}{\Delta t}\int_{\Omega_i}\left(\boldsymbol{u}^{n+1}-\boldsymbol{u}^{*}\right)dV=-\frac{1}{\rho}\mathcal{G}(P^{n+1}) \tag{3.18}$$

$$\frac{1}{\rho}\mathcal{L}(P^{n+1})=\frac{1}{\Delta t}\mathcal{D}(\boldsymbol{u}^{*}) \tag{3.19}$$

One can approximate the volume integrals present on the left-hand side of Eq. (3.17) and Eq. (3.18) using a Taylor expansion:

$$\int_{\Omega_i}\boldsymbol{u}dV=\int_{\Omega_i}\left(\boldsymbol{u}_i+\boldsymbol{\nabla}\boldsymbol{u}|_i(\boldsymbol{x}-\boldsymbol{x}_i)+\mathcal{O}(||\boldsymbol{x}-\boldsymbol{x}_i||^2)\right)dV \tag{3.20}$$

Using the fact that, as mentioned before, $\boldsymbol{x}_i$ represents the center of mass of Ω_i, we only get the following result, with second-order precision:

$$\begin{aligned}\int_{\Omega_i}\boldsymbol{u}dV &= \int_{\Omega_i}\left(\boldsymbol{u}_i+\mathcal{O}(||\boldsymbol{x}-\boldsymbol{x}_i||^2)\right)dV\\ \leftrightarrow \int_{\Omega_i}\boldsymbol{u}dV &= \boldsymbol{u}_iV_i\end{aligned} \tag{3.21}$$

with V_i the volume of Ω_i.
By using Eq. (3.21) within the equations Eq. (3.17), Eq. (3.18), we can rewrite Eq. (3.17), Eq. (3.18) and Eq. (3.19) one last time:

$$\frac{V_i}{\Delta t}\left(\boldsymbol{u}_i^{*}-\boldsymbol{u}_i^{n}\right)=-\mathcal{C}(\boldsymbol{u}^n,\boldsymbol{u}^n)+\mathcal{L}_{cv}(\nu,\boldsymbol{u}^n)+\mathcal{L}_{cv}^{T}(\nu,\boldsymbol{u}^n) \tag{3.22}$$

$$\frac{V_i}{\Delta t}\left(\boldsymbol{u}_i^{n+1}-\boldsymbol{u}_i^{*}\right)=-\frac{1}{\rho}\mathcal{G}(P^{n+1}) \tag{3.23}$$

$$\frac{1}{\rho}\mathcal{L}(P^{n+1})=\frac{1}{\Delta t}\mathcal{D}(\boldsymbol{u}^{*}) \tag{3.24}$$

It is this set of equations that are solved in YALES2BIO. Each operator previously defined is discretized to obtain the quantities $\boldsymbol{u}^{*}$, P^{n+1} and $\boldsymbol{u}^n+1$. YALES2BIO includes 2nd-order and 4th-order schemes in space. The 4th-order scheme is used in this thesis. The case of the second-order discretization is available in appendix Section (6.1) as an illustration.

Concerning the boundary conditions, more information is contained in the article of Kim and Moin 1985 [85]. In the present work, simple boundary conditions are used. In periodic boundaries, the nodes on the periodic boundaries are supposed to be shared by the boundary conditions. They are considered as part

of an internal boundary, and the treatment is identical as for nodes shared by multiple processors.

Non-slipping walls are used in this work, where the fluid velocity is set to that of the wall velocity, using Dirichlet boundary conditions. Wall velocity is either set to zero or to a tangential velocity when shear flows are studied. The shear is maintained by the boundaries. At inlets boundary conditions, Dirichlet boundary conditions are imposed. Dirichlet boundary conditions are imposed at the node velocity, between the prediction and the correction steps. At the outlets, convective boundary conditions are imposed [85]. Homogeneous Neumann boundary conditions are imposed on pressure when solving the Poisson equation.

3.2.3 Variable viscosity

Throughout this presentation, we have treated the fluid with a unique viscosity throughout the field. In the case of our application, it is important to be able to account for viscosity variations in space. Indeed, in general, the RBC is suspended in a medium with a viscosity different from its internal viscosity.
Let us therefore note ν_{in} and ν_{ext} the viscosity values of the internal and external fluids, respectively. The method implemented in YALES2BIO is based on the front-tracking method of Unverdi and Tryggvason 1992 [156]. The idea is to use an indicator function, allowing to determine if each node i of the fluid mesh is located inside or outside the globule. Thus, the viscosity ν_i is calculated as follows:

$$\nu_i = \nu_{ext} + (\nu_{in} - \nu_{ext})I_i \tag{3.25}$$

with I_i the indicator function at point i such that$I_i = 0$ if node i is outside the RBC and $I_i = 1$ if i is inside.
The indicator function is calculated by solving the following Poisson equation:

$$\boldsymbol{\nabla}.(\boldsymbol{\nabla} I) = -\boldsymbol{\nabla}.\boldsymbol{G} \tag{3.26}$$

where $\boldsymbol{G}$ informs about the normal to the membrane surface close to fluid node i. It is zero far enough for the membrane. More detail on $\boldsymbol{G}$ is given in the Section (3.3.2) (for the sake of precision, $\boldsymbol{G}$ is the regularized field of outward surface normal vector). Basically, this equation states that I should vary when we cross the membrane.

The discretization of the equation Eq. (3.26) is done as before thanks to the finite volumes and results in the following linear system:

$$\mathcal{L}(I)|_i = -\mathcal{D}(\boldsymbol{G})|_i \tag{3.27}$$

with $\mathcal{L}$ and $\mathcal{D}$ the operators defined above. This linear system is solved thanks to the DPCG method present in the article by Malandain *et al.*. [99].

3.3 Fluid-structure interaction: Immersed Boundary Method

3.3.1 Coupling: General algorithm

The numerical framework used in this work is the YALES2BIO solver (https://imag.umontpellier.fr/~YALES2BIO/), dedicated to the simulation of RBC dynamics under flow *et al.*ready used in several publications in the recent years [87, 103, 104, 105, 146, 153]. It is based on a continuum framework both for the fluid and the membrane. The membrane is supposed to be massless and may be viewed as an interface with specific surface tension that depends on its state of deformation. The fluid and the membrane are coupled by the Immersed Boundary Method (IBM) [129]. This technique enables the communication between two meshes, one for the fluid and one for the membrane. Inside the temporal loop, the main YALES2BIO algorithm can be reduced to four main steps:

1. For a given state of deformation of the membrane and using the material behavior law, the membrane stress field is computed. Nodal forces are then calculated under the massless membrane assumption.

2. The forces at the nodes are regularized to the fluid mesh to act as a source term for the Navier-Stokes equations, representing the action of the membrane on the fluid.

3. The next step consists in solving explicitly the incompressible Navier-Stokes equations in a finite-volume framework with the membrane forcing, thanks to a pressure projection technique [26, 99, 114] for imposing fluid incompressibility. This results in an updated fluid velocity field.

4. The fluid velocity is then interpolated to the membrane vertices, with the assumption that the membrane is displaced at the same velocity as the local fluid velocity. The membrane position is then updated with an explicit Euler scheme, which provides the deformation state for the next iteration. A volume conservation algorithm is used to guarantee that the volume inside the membrane does not change during the simulation [107, 145]. In case of a viscosity contrast between the cytoplasm and the suspending fluid, the fluid viscosity is then updated from the new membrane position, with different values inside and outside the membrane.

This algorithm has been presented and validated in several publications [87, 107, 145, 146].
In the previous part, we presented the different steps to obtain the calculation of the velocity and the pressure within a fluid domain. The next step is the communication between the fluid and the membrane. This step is necessary to allow the displacement of the various points constituting the RBC membrane, generating the deformations. This communication step is detailed in the next section.

3.3.2 Coupling: Interpolation and Spreading

The fluid resolution has been featured in previous parts. Within the framework of the problem study dealing with the modeling of red blood cells, the simple representation of the fluid is obviously not sufficient. Indeed, the idea is to represent the RBC in its environment, as well as the interactions between the RBC membrane and the fluid.
The interaction between the fluid and the membrane is possible in this study thanks to the IBM method, originally developed by Peskin [129]. This model is devoted to the interactions between a fluid domain and an infinitely thin and massless deformable membrane in this domain. The idea here will be to make a Lagrangian representation of the membrane coexist with an Eulerian representation of the fluid: the Eulerian grid is fixed and the Lagrangian grid follows the structure (*ie* the RBC membrane). The method is non-conformal. Thus, the position vector of a point i belonging to the fluid mesh will be noted $\boldsymbol{x}_i$ and will use the coordinate system $(\boldsymbol{e}_x, \boldsymbol{e}_y, \boldsymbol{e}_z)$, while a point belonging to the mesh of the membrane (also called marker) will be noted $\boldsymbol{X}_i$ and will use a system

$(\boldsymbol{e}_s, \boldsymbol{e}_r, \boldsymbol{e}_q)$, with $(\boldsymbol{e}_s, \boldsymbol{e}_r)$ tangential to the membrane and $\boldsymbol{e}_q$ oriented along the outward normal to the membrane. Since we assume the membrane to be infinitely thin, the coordinate q will not be used, so we are only in 2D from the Lagrangian point of view.

The fluid equations when taking into account the presence of a RBC in our framework is modified by a forcing source term $\boldsymbol{f}_v$. They are written as follows:

$$\begin{aligned} \frac{\partial \boldsymbol{u}}{\partial t} + \boldsymbol{\nabla}.(\boldsymbol{u} \otimes \boldsymbol{u}) &= -\frac{1}{\rho}\boldsymbol{\nabla} P + \boldsymbol{\nabla}.(\nu \boldsymbol{\nabla}\boldsymbol{u}) + \boldsymbol{\nabla}.(\nu(\boldsymbol{\nabla}\boldsymbol{u})^T) + \frac{1}{\rho}\boldsymbol{f}_v \\ \boldsymbol{\nabla} \cdot \boldsymbol{u} &= 0. \end{aligned} \tag{3.28}$$

The term $\boldsymbol{f}_v$ represents a volumetric version of the forces exerted by the membrane on the fluid. As the problem is modeled in our study, behind this term hides the forces linked to different behaviors in the deformation of the membrane such as the elastic behavior of the membrane, the resistance to curvature, and this is what is the heart of this study, the viscoelasticity of the membrane. It is important to note that $\boldsymbol{f}_v$ is an Eulerian term. It is directly related to the quantity $\boldsymbol{F}_{TOT}$, representing the forces generated by the internal stress of the membrane in the Lagrangian formalism.

Similarly, the fluid also acts on the solid, through the kinematic coupling condition: a non-slipping condition is imposed on the membrane, so that the membrane velocity is set to be equal to the fluid velocity. Indeed, the fluid velocity field $\boldsymbol{u}$ will thus move the different markers which will generate deformations on the membrane. In the Lagrangian formalism, the velocity of the membrane is denoted $\boldsymbol{U} = \dfrac{d\boldsymbol{X}}{dt}$, and is related to $\boldsymbol{u}$.

The coupling is therefore a matter of communicating these different Lagrangian and Eulerian quantities together, which is not straightforward as the meshes are not conformal. In our framework, calculating a Lagrangian quantity from an Eulerian quantity (so here a membrane quantity from a fluid quantity) is called the interpolation step. The membrane velocity needs to be interpolated from the fluid. Formally, the non-slipping condition at the membrane reads:

$$\frac{d\boldsymbol{X}}{dt} = \int_{\Omega_f} \boldsymbol{u}\delta(\boldsymbol{x} - \boldsymbol{X})d\boldsymbol{x} \tag{3.29}$$

with Ω_f the fluid volume in our case, δ represents the Dirac function (which is 1 when $\boldsymbol{x} = \boldsymbol{X}$ and 0 otherwise) and $d\boldsymbol{x}$ the infinitesimal quantity related to

$(\boldsymbol{e}_x, \boldsymbol{e}_y, \boldsymbol{e}_z)$.

Moreover, calculating an Eulerian quantity from a Lagrangian quantity, here a fluid quantity from a membrane quantity is called the spreading (also called regularisation) step. This is what is done to compute the term $\boldsymbol{f}_v$ as follows:

$$\boldsymbol{f}_v(\boldsymbol{x}) = \int_{\Omega_s} \boldsymbol{F}_{TOT}(\boldsymbol{X})\delta(\boldsymbol{x} - \boldsymbol{X})drds \tag{3.30}$$

with Ω_s the surface of the membrane in our case, δ the Dirac function and dr and ds respectively the infinitesimal quantities related to $\boldsymbol{e}_r$ and $\boldsymbol{e}_s$.
Regularization is also necessary in the calculation of the viscosity field, by spreading the normal n to the membrane on the domain, to allow the calculation of the indicator function I mentioned Section (3.2.3) . So, $\boldsymbol{G}$ is calculated as:

$$\boldsymbol{G} = \int_{\Omega_s} \boldsymbol{n}\delta(\boldsymbol{x} - \boldsymbol{X})drds \tag{3.31}$$

with $\boldsymbol{n}$ the outward membrane normal.
However, as the grids are not conformal, interpolation and regularization are not perfectly local. In other words, the Dirac function needs to be approximated, using and appropriate window function [129]. Let N be the number of volumes making up the fluid domain and M the number of markers on the surface mesh of the membrane. We obtain for the equations Eq. (3.29), Eq. (3.30) and Eq. (3.31) respectively:

$$\frac{d\boldsymbol{X}_j}{dt} = \sum_{i=1}^{N} \boldsymbol{u}_i \delta_h(\boldsymbol{x}_i - \boldsymbol{X}_j)V_i \tag{3.32}$$

$$\boldsymbol{f}_v(\boldsymbol{x}_i) = \sum_{j=1}^{M} \boldsymbol{F}_{TOT}|_j \delta_h(\boldsymbol{x}_i - \boldsymbol{X}_j)S_j^m \tag{3.33}$$

$$\boldsymbol{G}(\boldsymbol{x}_i, t) = \sum_{j=1}^{M} \boldsymbol{n}|_j \delta_h(\boldsymbol{x} - \boldsymbol{X})S_j^m \tag{3.34}$$

with V_i the volume of the control volume Ω_i and S_j^m the surface surrounding the marker m. δ_h is an approximation of the analytical Dirac function δ. The shape of the window function depends, among other things, on the desired properties [139], but also on the meshes (regular or not). The construction of these functions in the regular mesh framework is treated in Peskin's work [128, 139]. Extensions on irregular meshes have been proposed by Liu *et al.* [93, 94, 96] using the so-called

Reproducing Kernel Particle Method and adapted by Pinelli *et al.* [131] and Mendez *et al.* [107] to our framework.
In conclusion, we presented the interpolation and spreading tools allowing the coupling of fluid models and RBC membrane models. The method to solve the fluid equation has been presented in Section (3.2). It yields the fluid velocity field $\boldsymbol{u}$, which is then interpolated on the membrane markers, and these are therefore moved accordingly, using a first-order Euler approximation. To allow the complete presentation of the calculation process in our framework, it remains to present the calculation of the different quantities constituting $\boldsymbol{F_{TOT}}$.

3.3.3 In-plane stress: Hyperelasticity

As presented Section (2.4.1), the hyperelastic model used to represent the hyperelastic behavior of the membrane is based on Skalak's law [149]. This law leads to the following expressions:

$$\begin{aligned}
\sigma_{11} &= \frac{G_s}{\lambda_1\lambda_2}\left[\lambda_1^2(\lambda_1^2-1) + C(\lambda_1\lambda_2)^2\left[(\lambda_1\lambda_2)^2-1\right]\right] \\
\sigma_{22} &= \frac{G_s}{\lambda_1\lambda_2}\left[\lambda_2^2(\lambda_2^2-1) + C(\lambda_1\lambda_2)^2\left[(\lambda_1\lambda_2)^2-1\right]\right] \\
\sigma_{12} &= \sigma_{21} = 0
\end{aligned} \tag{3.35}$$

with σ_{ij} the components of the Cauchy stress tensor $\boldsymbol{\sigma}$ on the surface (in Pa.m), λ_i the eigenvalues of the transformation gradient tensor $\boldsymbol{F}$ expressed as $\boldsymbol{F} = \frac{\partial x(t)}{\partial x(0)}$, with $x(t)$ the current state and $x(0)$ denotes the stress-free state. G_s is the Skalak shear modulus (in Pa.m) and C the ratio between the area change modulus and the shear modulus.
to calculate the λ_i, it is possible to express them as a function of the Cauchy-Green strain tensor $\boldsymbol{\mathcal{G}}$. Let's first recall the expression of $\boldsymbol{\mathcal{G}}$ as a function of the tensor transformation $\boldsymbol{F}$:

$$\boldsymbol{\mathcal{G}} = \boldsymbol{F}^T\boldsymbol{F} = \left(\boldsymbol{I} + \frac{\partial \boldsymbol{U}}{\partial s}\right)^T\left(\boldsymbol{I} + \frac{\partial \boldsymbol{U}}{\partial s}\right) \tag{3.36}$$

with $\boldsymbol{I}$ the identity matrix and $\boldsymbol{U}$ the displacement field on the membrane.
This tensor is symmetric, and of dimension two in our problem. This allows to

define the following expression of the square of the eigenvalues λ_1 and λ_2:

$$\begin{aligned} \lambda_1^2 &= \frac{1}{2}\left(G_{11}+G_{22}+\sqrt{(G_{11}-G_{22})^2+4G_{12}^2}\right) \\ \lambda_2^2 &= \frac{1}{2}\left(G_{11}+G_{22}-\sqrt{(G_{11}-G_{22})^2+4G_{12}^2}\right) \end{aligned} \tag{3.37}$$

with G_{ij} the components of $\boldsymbol{\mathcal{G}}$. The transition of this expression to the forces at the solid nodes which is added to $\boldsymbol{F_{TOT}}$ is detailed in the next part.

3.3.4 From element stress to nodal forces

In YALES2BIO, a first-order finite-element method is used. The computation of the nodal forces from the stress in the element is detailed in what follows. We use only triangular elements, which are assumed to remain flat during the deformation of the membrane. Thus, in the element basis, deformations are two-dimensional, and each displacement can be split into X and Y components, respectively horizontal and vertical axis in the element basis. Noting u_1, u_2, u_3 and v_1, v_2, v_3 the X and Y displacements, respectively, of the nodes $1, 2, 3$ of any triangular element, and assuming linear interpolation between the three nodes, displacements on the element can be written as:

$$\begin{aligned} u &= N_1u_1 + N_2u_2 + N_3u_3, \\ v &= N_1v_1 + N_2v_2 + N_3v_3, \end{aligned} \tag{3.38}$$

with N_1, N_2, N_3 linear shape functions of the element, that can be computed as:

$$\begin{aligned} N_1 &= \frac{(y_2-y_3)x+(x_3-x_2)y+(x_2y_3-x_3y_2)}{2A_0} = \frac{a_1x+b_1y+c_1}{2A_0}, \\ N_2 &= \frac{(y_3-y_1)x+(x_1-x_3)y+(x_3y_1-x_1y_3)}{2A_0} = \frac{a_2x+b_2y+c_2}{2A_0}, \\ N_3 &= \frac{(y_1-y_2)x+(x_2-x_1)y+(x_1y_2-x_2y_1)}{2A_0} = \frac{a_3x+b_3y+c_3}{2A_0}, \end{aligned} \tag{3.39}$$

with A_0 the element area at t=0. a_i, b_i and c_i are the coefficients of the shape functions, only determined by the shape of the element at rest. Since displacements can be fully expressed as a function of known parameters following Eq. (3.39), the displacement can be used to express the two-dimensional transformation gradient

$\boldsymbol{F} = \dfrac{\partial x(t)}{\partial x(0)}$. It can also be expressed as $F_{ij} = \delta_{ij} + \dfrac{\partial u_i}{\partial x_j}$. Using Eq. (3.38) and Eq. (3.39), $\boldsymbol{F}$ becomes:

$$\boldsymbol{F} = \frac{1}{2A_0}\begin{pmatrix} 2A_0 + \sum_{i=0}^{3} a_i u_i & \sum_{i=0}^{3} b_i u_i \\ \sum_{i=0}^{3} a_i v_i & 2A_0 + \sum_{i=0}^{3} b_i v_i \end{pmatrix} \tag{3.40}$$

Eq. (3.40) will be used when writing the principle of virtual work to obtain the nodal forces. Because we are neglecting inertial effects, equilibrium of forces and moment equations can be written as:

$$div(\boldsymbol{\sigma}) = \vec{0};\ \boldsymbol{\sigma}^T = \boldsymbol{\sigma} \tag{3.41}$$

The virtual work principle is just a weak formulation of the following equilibrium equations. It is obtained by integrating stress Cauchy tensor $\boldsymbol{\sigma}$ contracted to a virtual arbitrary displacement vector $\vec{\delta u}$, with δu and δv its components, over the element's area. This leads to this formulation:

$$\int_S div(\boldsymbol{\sigma}) \cdot \vec{\delta u}\ ds = 0 \tag{3.42}$$

Using the divergence theorem, it leads to:

$$\int_S \boldsymbol{\sigma} : \boldsymbol{grad}(\vec{\delta u})\ ds - \int_{\Omega S} \vec{S} \cdot \vec{\delta u}\ dl = 0 \tag{3.43}$$

with ΩS the element's boundary, $\vec{\delta u}$ the virtual displacement vector, dl the integration variable representing an infinitesimal part of the element's boundary and $\vec{S}$ the traction vector $\vec{S} = \boldsymbol{\sigma}\vec{n}$, with $\vec{n}$ the outward unit normal vector of the element's boundary. The gradient term can be written as:

$$\boldsymbol{grad}(\vec{\delta u}) = \frac{\partial \delta u}{\partial x(t)} = \frac{\partial \delta u}{\partial x(0)}\frac{\partial x(0)}{\partial x(t)} = \boldsymbol{\delta F}\boldsymbol{F}_0(t)^{-1} \tag{3.44}$$

As for Eq. (3.40), by using Eq. (3.38), $\boldsymbol{\delta F}$,the variation of $\boldsymbol{F}$ associate with the virtual displacement $\vec{\delta u}$, can be identified as:

$$\boldsymbol{\delta F} = \frac{1}{2A_0}\begin{pmatrix} \sum_{i=0}^{3} a_i \delta u_i & \sum_{i=0}^{3} b_i \delta u_i \\ \sum_{i=0}^{3} a_i \delta v_i & \sum_{i=0}^{3} b_i \delta v_i \end{pmatrix} \tag{3.45}$$

with $\delta u_i,\ \delta v_i$ the virtual X and Y nodal displacements, respectively. The second term of Eq. (3.43) is then developed to identify nodal forces. As previously, $\vec{\delta u}$ can be identified thanks to Eq. (3.38) in:

$$\vec{\delta u} = \begin{pmatrix} N_1\delta u_1 + N_2\delta u_2 + N_3\delta u_3 \\ \\ N_1\delta v_1 + N_2\delta v_2 + N_3\delta v_3 \end{pmatrix} \tag{3.46}$$

Defining $\vec{\delta u^N}$ and $\vec{P^N}$ respectively the nodal displacement vector and the nodal force vector, expressed as:

$$\vec{\delta u^N} = \begin{pmatrix} \delta u_1 \\ \delta v_1 \\ \delta u_2 \\ \delta v_2 \\ \delta u_3 \\ \delta v_3 \end{pmatrix},\ \vec{P^N} = \begin{pmatrix} \int_{\Omega S} S_X N_1 dl \\ \int_{\Omega S} S_Y N_1 dl \\ \int_{\Omega S} S_X N_2 dl \\ \int_{\Omega S} S_Y N_2 dl \\ \int_{\Omega S} S_X N_3 dl \\ \int_{\Omega S} S_Y N_3 dl \end{pmatrix}, \tag{3.47}$$

and assuming stress and deformation gradient constant on the element, it leads that Eq. (3.43) is equivalent to:

$$tr(\boldsymbol{\delta F} \boldsymbol{F}_0^{-1}(t)\boldsymbol{\sigma})A - \vec{\delta u^N} \cdot \vec{P^N} = 0 \tag{3.48}$$

with A the area of the current (deformed) element. Using the fact that this relation is true for every virtual displacement, the components of $\vec{P^N}$ can be directly identified by splitting the equality with respect to the $\vec{\delta u}$ components, leading to an equality for each $\vec{P^N}$ component.

3.3.5 Curvature forces

As defined in Section (2.4.2) Eq. (2.5), in this model the force coming from the curvature of the RBC follow the Helfrich energy:

$$W_b = \frac{E_b}{2} \int_{\Omega_S} (2\kappa - c_0)^2 dS \tag{3.49}$$

κ corresponds to the mean curvature, E_b to the modulus of curvature and c_0 to the spontaneous curvature.
During most of this work, the calculations were carried out thanks to a model developed thanks to the work of Zhong-can *et al.* and Farutin *et al.* [48, 167]. By taking the functional derivative of the curvature energy, the expression of $\boldsymbol{F}_b^O$, the surface density of force due to the bending at marker O, is obtained:

$$\boldsymbol{F}_b^O = E_b \left((2\kappa^O - c_0)(2(\kappa^O)^2 - 2\kappa_s^0 + \kappa^O c_0) + 2\nabla^s \kappa^O \right) \boldsymbol{n}^O. \tag{3.50}$$

κ_s represents the Gaussian curvatures and ∇^s the Laplace Beltrami operator. It is seen that this expression features a 4th-order derivative of the membrane surface (the Laplacian operator applied to the mean curvature).
The calculation of the different curvatures and of the surface Laplacian of the mean curvature was based on the work of Farutin et al [48]. Basically, the principle is to express the field of local coordinates of the membrane vertices as a quadratic approximation in the tangential coordinates, then use differential geometry formula to calculate the mean and Gaussian curvatures. The same method is then applied to calculate the surface Laplacian of the mean curvature.

3.4 Implementation of the membrane viscosity

3.4.1 Implementation

The calculation of the purely hyperelastic RBC membrane forces is based on a first-order finite-element framework that has often been used in RBC modeling [21]. It has already been validated in numerous cases [104, 107, 145]. To compute forces applied on the fluid from a hyperelastic membrane, λ_i, the eigenvalues of the transformation gradient, are first calculated for the membrane elements. Then, the membrane stress is computed thanks to Eq. (2.4). The stress is then used to compute nodal forces using the virtual work principle as in Shrivastava and Tang's work [144]. Details about the methodology to obtain nodal forces are provided in Appendix.

Steps for implementation of viscoelastic behavior are similar, except that membrane viscous stress is a priori a function of the whole history of deformation of the membrane, so that some preliminary work is needed to express it as a function of the last time step only. Because only shear viscosity is considered here,

the expression of the membrane viscoelastic behavior can be written as:

$$\boldsymbol{\sigma}(t) = \boldsymbol{\sigma}^d + \sigma^h(t)\boldsymbol{I} = \int_0^t 2G(t-s)\dot{\boldsymbol{\varepsilon}}^d ds + \sigma^h(t)\boldsymbol{I}, \tag{3.51}$$

with t the time, $\boldsymbol{\sigma}$ the Cauchy stress tensor, $G(t-s)$ the relaxation modulus of the viscoelastic model (in Pa.m) at time $t-s$, $\dot{\boldsymbol{\varepsilon}}^d$ the time derivative of the deviatoric part of the strain tensor $\boldsymbol{\varepsilon}$, σ^h the mean normal of the Cauchy stress tensor, calculated as $\sigma^h = \frac{tr(\boldsymbol{\sigma})}{DIM(\boldsymbol{\sigma})}$ and $\boldsymbol{I}$ the identity matrix. This expression is just another form of the Eq. (2.10), split using the hypothesis of separation of deviatoric and spherical part of the stress tensor, and neglect the hydrostatic viscosity.

The first hypothesis is that we assume additivity between the Hooke spring and the viscous damper (see Fig. 2.5). This leads to the following formulation of the relaxation modulus:

$$G(t) = G_\infty + G_H e^{-\frac{t}{t_c}}, \tag{3.52}$$

with G_∞ the Skalak shear modulus from the pure hyperelastic branch (in Pa.m), G_H the Hooke shear modulus from the viscoelastic branch (in Pa.m), and t_c the Maxwell characteristic time of the viscoelastic branch computed as $t_c = \frac{\eta}{G_H}$ with η the membrane viscosity (in Pa.s.m).

With the aforementioned hypotheses, Simo [147] obtained an expression for the Kirchhoff stress tensor $\boldsymbol{\tau} = det(\boldsymbol{F})\boldsymbol{\sigma}$, with $\boldsymbol{\sigma}$ the Cauchy stress tensor and $\boldsymbol{F}$ the deformation gradient tensor. We will thus keep the formulation with the Kirchhoff stress tensor until the end of the derivation, which simplifies the reading and the comparison with existing literature, where the Kirchhoff tensor is classically used. Using integration by part in Eq. (3.51) enables to apply the derivation in time on the relaxation modulus:

$$\boldsymbol{\tau}(t) = \boldsymbol{\tau}_0^d(t) + SYM\left[\int_0^t \frac{\dot{G}(s)}{G_0}\boldsymbol{F}_t^{-1}(t-s)\cdot\boldsymbol{\tau}_0^d(t-s)\cdot\boldsymbol{F}_t(t-s)ds\right] + \tau^h(t)\boldsymbol{I}, \tag{3.53}$$

with $\boldsymbol{\tau}_0^d$ the deviatoric part of the instantaneous Kirchhoff stress computed with $G_0 = G(0) = G_\infty + G_H$ and $\tau^h(t)$ the mean normal Kirchhoff stress. The SYM is the operator that ensure the symmetry of the resulting tensor. It appears to be needed and is used in the literature [162]. Explanation on why this term is necessary was not in the scale of this work, but would be interesting. Finally, $\boldsymbol{F}_t(t-s)$ represents the deformation gradient computed between time t and time $t-s$. Also called shifter, its expression is:

$$\boldsymbol{F}_{t_1}(t_2) = \frac{\partial x(t_2)}{\partial x(t_1)}, \tag{3.54}$$

with $x(t)$ the Lagrangian position of the solid particle at the time t. It is important to note that the main role of the shifter is to enable the stress sum. Indeed, for finite strains, it makes no sense to add stresses from different strain configurations. Shifters $\boldsymbol{F}_t(t-s)$ transport the stress at time $t-s$ to the time t, for every s value between 0 and t. Now, simply combining Eq. (3.52) with Eq. (3.53) leads to:

$$\boldsymbol{\tau}(t) = \boldsymbol{\tau}_0^d(t) - \boldsymbol{\tau}_{visc}(t), \tag{3.55}$$

with $\boldsymbol{\tau}_{visc}(t)$ expressed as:

$$\boldsymbol{\tau}_{visc}(t) = \frac{G_H}{t_c G_0} SYM\left[\int_0^t \boldsymbol{F}_t^{-1}(t-s)\cdot\boldsymbol{\tau}_0^d(t-s)\cdot\boldsymbol{F}_t(t-s)e^{-\frac{s}{t_c}}ds\right]. \tag{3.56}$$

From this expression, we can see that an integration between $t=0$ and t is needed to compute the stress. The next step consists in modifying this expression to make it depend on times t and $t-\Delta t$ only. To do so, Eq. (3.54) allows expressing $\boldsymbol{F}_t(t-s)$ as a function of $\boldsymbol{F}_t(t-\Delta t)$:

$$\boldsymbol{F}_t(t-s) = \boldsymbol{F}_{t-\Delta t}(t-s)\cdot\boldsymbol{F}_t(t-\Delta t). \tag{3.57}$$

Consequently, we have also:

$$\boldsymbol{F}_t^{-1}(t-s) = \boldsymbol{F}_t^{-1}(t-\Delta t)\cdot\boldsymbol{F}_{t-\Delta t}^{-1}(t-s). \tag{3.58}$$

By substituting Eq. (3.57) and Eq. (3.58) into Eq. (3.56), and by doing a variable change from s to $s+\Delta t$, Eq. (3.56) can be split in two terms as follows:

(3.59) :

$$\begin{aligned}\boldsymbol{\tau}_{visc}(t) &= \tfrac{G_H}{t_c G_0} SYM\Big[\boldsymbol{F}_t^{-1}(t-\Delta t)\cdot\textstyle\int_{-\Delta t}^{0}\boldsymbol{F}_{t-\Delta t}^{-1}(t-\Delta t-s)\cdot\boldsymbol{\tau}_0^d(t-\Delta t-s)\cdot\boldsymbol{F}_{t-\Delta t}(t-\Delta t-s)e^{-\frac{s+\Delta t}{t_c}}ds\cdot\boldsymbol{F}_t(t-\Delta t)\Big]\\ &+ \tfrac{G_H}{t_c G_0} SYM\Big[\boldsymbol{F}_t^{-1}(t-\Delta t)\cdot\textstyle\int_{0}^{t-\Delta t}\boldsymbol{F}_{t-\Delta t}^{-1}(t-\Delta t-s)\cdot\boldsymbol{\tau}_0^d(t-\Delta t-s)\cdot\boldsymbol{F}_{t-\Delta t}(t-\Delta t-s)e^{-\frac{s+\Delta t}{t_c}}ds\cdot\boldsymbol{F}_t(t-\Delta t)\Big].\end{aligned}$$

We can use Eq. (3.56) to identify the integral from 0 to $t-\Delta t$ as a known term depending on $\boldsymbol{\tau}_{visc}(t-\Delta t)$, which results from the previous time step. To compute the final integral term, we will assume that $\boldsymbol{\tau}_0^d$ varies linearly over one time step. Finally, we obtain the following expression that can be implemented for the computation of $\tau_{visc}(t)$:

$$\boldsymbol{\tau}_{visc}(t) = \alpha\frac{G_H}{G_0}\boldsymbol{\tau}_0^d(t) + \beta\frac{G_H}{G_0}\hat{\boldsymbol{\tau}}_0^d(t-\Delta t) + \hat{\boldsymbol{\tau}}^d(t-\Delta t)\times e^{-\frac{\Delta t}{t_c}}, \tag{3.59}$$

with:

$$\begin{cases} t_c = \frac{\eta}{G_H} \\ \alpha = 1 - \frac{t_c}{\Delta t}(1 - e^{-\frac{\Delta t}{t_c}}) \\ \beta = \frac{t_c}{\Delta t}(1 - e^{-\frac{\Delta t}{t_c}}) - e^{-\frac{\Delta t}{t_c}} \\ \hat{\boldsymbol{\tau}}_0^d(t - \Delta t) = SYM\left[\boldsymbol{F}_t^{-1}(t - \Delta t) \cdot \boldsymbol{\tau}_0^d(t - \Delta t) \cdot \boldsymbol{F}_t(t - \Delta t)\right] \\ \hat{\boldsymbol{\tau}}^d(t - \Delta t) = SYM\left[\boldsymbol{F}_t^{-1}(t - \Delta t) \cdot \boldsymbol{\tau}_{visc}(t - \Delta t) \cdot \boldsymbol{F}_t(t - \Delta t)\right] \end{cases} \tag{3.60}$$

Once the stress tensor computed, we use the principle of virtual work [144] to compute the associated nodal forces at the vertices of the element (see in Section (3.3.4)). The contribution of one element to the nodal force $\vec{f_n}$ of one of its vertices n is:

$$\vec{f_n}(t) = V_{elem}(t)\boldsymbol{F_0}^{-1}(t)\boldsymbol{\sigma}(t)\vec{\varphi}_n \tag{3.61}$$

with V_{elem} the deformed element area and $\vec{\varphi}_n$ the vector of the shape function corresponding to node n. The final force for each node of the membrane is obtained by accumulating of the nodal forces associated with all the elements which contain that node.

3.4.2 Validation: small strain cases

In this section, verification test cases are presented.

It is important to note that cases presented are not sufficient to ensure the good implementation of the viscoelastic model presented here. However, they allowed to debug during implementation and ensure a certain number of elementary consistency behaviors of the implemented version. They are quick to compute, and they enabled us to understand a lot on the mechanics behind the viscoelastic behavior. A more involved validation test cases is proposed in the next section.

Local verification test cases are important to validate the good functioning of the subroutines. Three local test cases were computed. Two cases outside the fluid with imposed strain: an homothety Fig. 3.1 and a pure shear Fig. 3.3. The third one is a strain relaxation inside the fluid from a deformed configuration.

The homotethy case enables to check that the viscosity has no impact on the hydrostatic part of the stress tensor.

The pure shear enables to validate the viscoelastic behavior (value of instantaneous and relaxed stress and the characteristic time). Finally, the relaxation inside the fluid checks the compatibility of the viscoelastic behavior with the immersed boundary method (IBM) [129], which is used in YALES2BIO to compute the fluid structure interaction [107].

Imposed strain : homothety

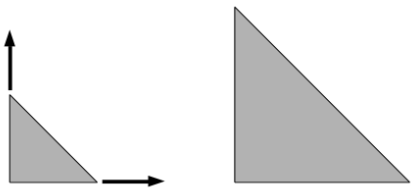

Figure 3.1: homothety test case, with reference configuration (left) and deformed one (right).

The main goal of this case is to ensure that the viscous behavior has only an effect on the deviatoric part of the stress tensor. By imposing the strain on our mesh and comparing stress obtained by using only the hyperelastic behavior to the viscoelastic computation, we can check the good implementation of the viscosity on the deviatoric part of the stress tensor. Indeed, because such a configuration does not involve any shear, then pure hyperelastic and our viscoelastic model should behave the same. We obtained the same stress between Skalak hyperelastic law and the viscoelastic one (see Fig. 3.2), which verifies this elementary aspect of the implementation.

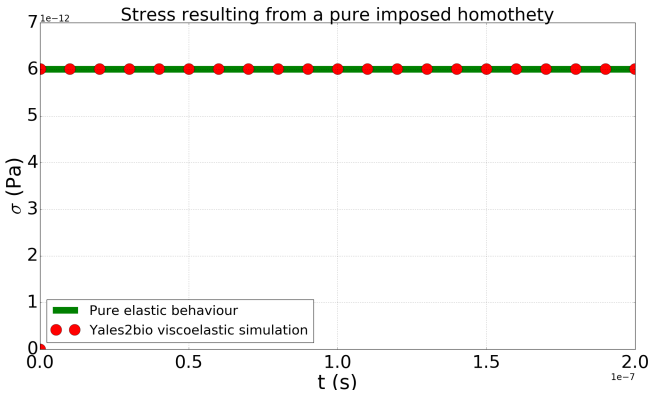

Figure 3.2: Comparison of the stress during time obtained by simulation and the analytical hyperelastic solution. The imposed strain starts at $t = 0s$

Imposed strain: pure shear

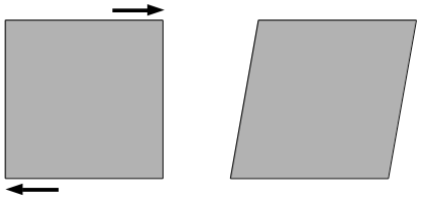

Figure 3.3: Schematic of the pure shear test case, with reference configuration (left) and deformed one (right). The deformation is exaggerated in the figure. The simulation is performed on a single element, without fluid. Thus, the deformation is imposed, and the stress response is studied.

The main goal here is to verify that the law implemented follows the generalized Maxwell viscoelastic model on the deviatoric part of the stress. To verify the implementation, a small strain is applied, so that the hyperelastic law is well represented by a Hooke's law [9], which enables to derive an analytical solution. For a Zener model on which an instantaneous strain ε_0 is imposed, the stress response, known analytically, is as follows:

$$\sigma(t) = G_1 \varepsilon_0 e^{-\frac{G_1 t}{\eta}} + G_\infty \varepsilon_0 \tag{3.62}$$

with G_1 and G_∞ respectively the elastic modulus of the viscous and elastic branches of the Zener model and η the viscosity modulus.

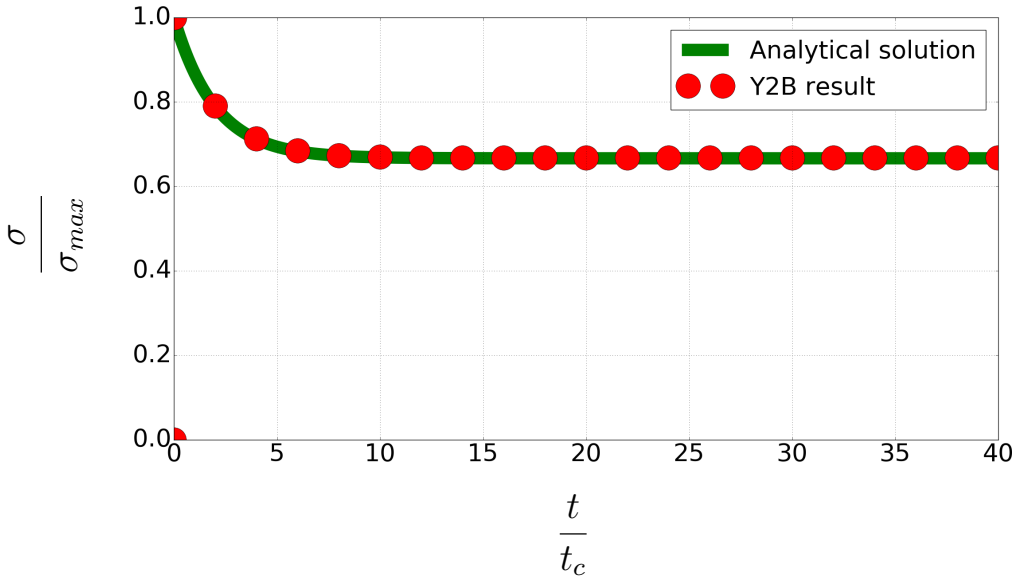

Figure 3.4: Stress responses as a function of time for a Zener model for a strain-imposed case.

In this test case, we consider a one-branch generalized Maxwell model, also named Zener model, with $G_\infty = G_1 = 3.0 \times 10^{-6}$ Pa.m, and a membrane viscosity of $\eta_1 = 3.0 \times 10^{-15}$ Pa.m.s. This configuration enabled us to check that the instantaneous stress is equal to the theoretical one and that the relaxed stress is equal to the Skalak hyperelastic one Fig. 3.4. Moreover, we also checked that the characteristic time of the implemented model is the stress relaxation of the Zener model, given by the branch viscoelastic characteristic time $t_c = \frac{\eta_1}{G_1}$. We did similar verifications for multiple-branch models and obtained valid results.

3.4.3 Convergence Zener to Kelvin-Voigt

The modeling choice (represented in Fig. 2.5) made is that the implemented model must behave like a Kelvin-Voigt model. The behavior of a Zener model converges to a behavior like a Kelvin-Voigt model provided that the elastic modulus of the viscous branch is high enough. This can be shown by using the analytical results concerning the response of these models to an imposed stress test. Consider a Kelvin-Voigt model with viscosity η and elastic modulus G. Consider a Zener model with parameters G, G_{branch} and η. We impose $\sigma(t) = \sigma_0 H(t)$ with $H(t)$ the function which equals 0 if $t \leq 0$ and 1 otherwise. The analytical solutions of

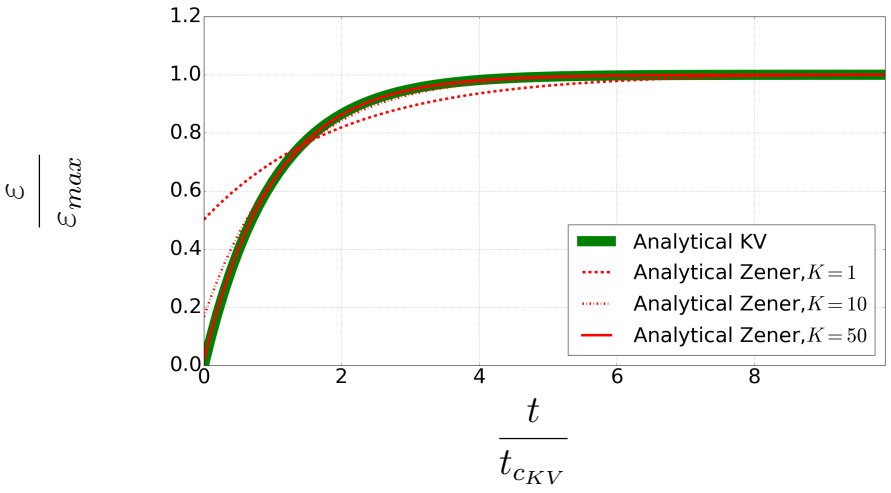

Figure 3.5: Analytical results of strain responses as a function of time for a Kelvin-Voigt and Zener models for an imposed stress. K represents the ratio between the elastic modulus of the viscous branch of a Zener model and the elastic modulus from the purely elastic branch.

these models to such a mechanical load are respectively:

$$\begin{aligned} \varepsilon_{KV}(t) &= \frac{\sigma_0}{G}\left(1 - e^{\frac{Gt}{\eta}}\right) \\ \varepsilon_{Zener}(t) &= \frac{\sigma_0}{G}\left(1 - \frac{G_{branch}}{G + G_{branch}} e^{\frac{GG_{branch}t}{\eta(G+G_{branch})}}\right). \end{aligned} \tag{3.63}$$

Thanks to these results, we can verify the convergence when the branch modulus increases. An expanded case is shown for illustration in Fig. 3.5. By defining the parameter K such as $K = \frac{G_{branch}}{G}$, we can observe the convergence of the Zener model for $K = 50$ in this case. It is important to specify that the value of K to ensure good convergence of the model depends on the parameters of the problem. Indeed, the convergence towards a Kelvin-Voigt model will be less and less true at $K = 50$ as the viscosity increases for example. Thus, we verified the good convergence of the behavior empirically for each simulation. In the range of this work, a value of K of 50 is enough to have convergence of the behavior.

3.5 Validation: capsule under shear flow

to validate the implementation of the viscoelastic model in the regime of large deformations, we take advantage of recent publications reporting the dynamics of

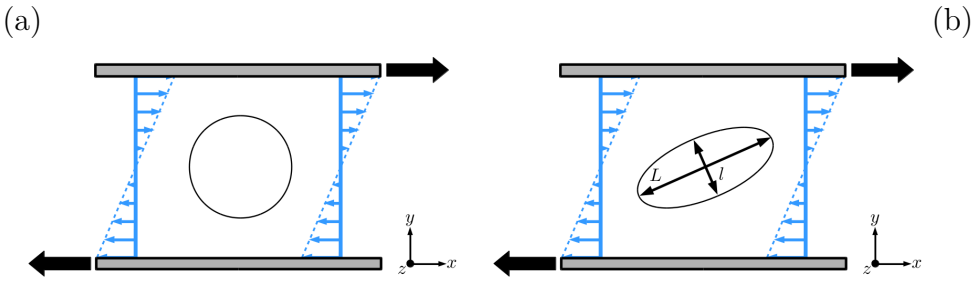

Figure 3.6: Representation of a capsule under shear flow. (a) Undeformed capsule at $t = 0$ (b) deformed capsule at $t > 0$ due to the shear flow, enabling the measurement of $D_{caps} = \frac{L-l}{L+l}$.

viscoelastic capsules [68, 90]. Data for the deformation of spherical capsules in a pure shear flow are available for different values of the membrane viscosity. The principle of the configuration is presented in Fig. 3.6. In addition, the viscoelastic model used in these two studies [68, 90] relies on the same assumptions as those used in the present paper and described in the former section. It leads to model the capsule membrane as a Kelvin-Voigt material, obtained as the limit of a Zener model with $G_H >> G_\infty$. When a spherical capsule is sheared, it deforms with a shape similar to an ellipsoid. The maximum elongation is of course in the quadrant of extension (x and y of the same sign), with a certain angle with respect to the flow direction x. The capsule is compressed in the perpendicular direction in the shear plane. To quantify the deformation, a deformation index may be calculated, defined as $D_{caps} = \frac{L-l}{L+l}$, with L and l the large and small lengths (in the shear plane), respectively, of the ellipsoid having the same inertia tensor as the capsule (see Fig. 3.6b).

The capsule is initially a 3D sphere of radius a described by a triangular mesh of 2890 elements. The typical edge length of this surface mesh is initially of $L_{elem} \approx \frac{a}{10}$. The capsule is in a cubic fluid domain of size $20a$, discretized by a Cartesian mesh of 200^3 cubic elements, of the same size as L_{elem}. The domain is large enough to minimize the effects of the boundary conditions on the results [68, 90]. Two moving walls are imposed as boundary conditions at the top and bottom of the domain to impose the shear rate (see Fig. 3.6), so that the velocity field in the absence of capsule reads $\vec{u} = \dot{\gamma} y \vec{e_x}$. Periodic boundary conditions are imposed in the x and z directions.

The non-dimensional numbers involved in this case are the Reynolds number R_e, the capillary number Ca, the viscosity ratio λ and the external Boussinesq

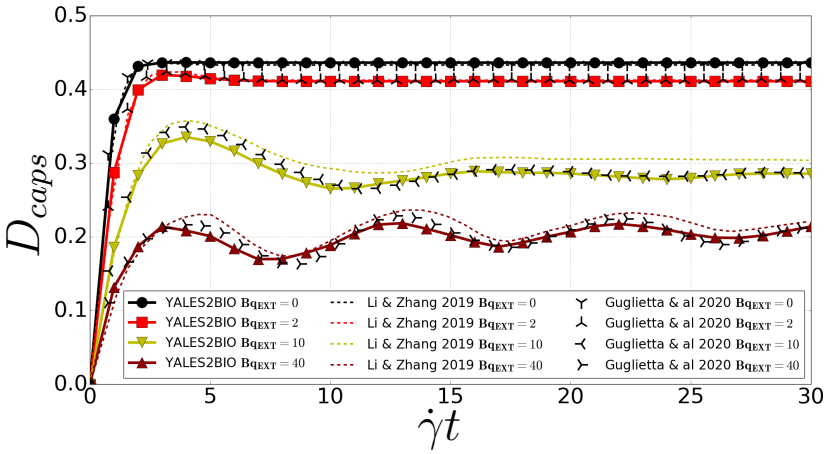

Figure 3.7: Deformation index as a function of non-dimensional time $\dot{\gamma}t$ for spherical capsules under shear with different Bq_{ext}, at $Ca = 0.3$ and $\lambda = 1$. Comparison of present results (YALES2BIO) with those from Li and Zhang [90] and Guglietta *et al.* [68].

number Bq_{ext}. There are defined as follows:

$$R_e = \frac{\rho \dot{\gamma} a^2}{\mu_{ext}};\ C_a = \frac{\mu_{ext} \dot{\gamma} a}{G_\infty};\ \lambda = \frac{\mu_{int}}{\mu_{ext}};\ Bq_{ext} = \frac{\eta}{a \mu_{ext}} \tag{3.64}$$

with ρ the constant density, μ_{int} and μ_{ext} the internal and external fluid dynamic viscosities (in Pa.s), respectively, η the membrane viscosity (in Pa.m.s). All the following computations are done at $Re = 0.2$ to avoid having important inertial effects while keeping the computational cost moderate, $Ca = 0.3$ and $\lambda = 1$. Only Bq_{ext} is changed between the different cases. Results are displayed in Fig. 3.7.

Fig. 3.7 shows that the simulations from the different groups (including ours) predict the same trends regarding the effect of membrane viscosity on the dynamics of a spherical membrane. When no membrane viscosity is considered, a steady-state is rapidly reached, with an asymptotic deformation of $D_{caps} \approx 0.44$. Deformations are then reduced when Bq_{ext} is small. For higher values, oscillations in the deformation appear, with a relative frequency increasing with Bq_{ext}. Finally, note that the present computations are very close to the results by Guglietta *et al.* [68], which is the closest method to ours in terms of membrane modeling. Despite major differences in the general algorithm with the previous studies [68, 90], results align very well, so that the implementation of the viscoelastic model is validated.

Note also that a similar test case has been computed by Yazdani and Bagchi (2013) [162] with similar trends in the general behavior. However, we could not reproduce their results. The agreement with other studies [68, 90] make us assume that results from Yazdani and Bagchi (2013) are singular and may not be perfectly trustworthy.

Chapter 4

Application

Chapter contents

4.1 Introduction 76
4.2 Effect of membrane viscosity on tank-treading red blood cells . . . 77
4.2.1 Introduction 77
4.2.2 Numerical setup and operating points 77
4.2.3 Non-dimensional study 80
4.2.4 Dimensional study 83
4.2.5 Shear-thinning model 86
4.3 Strain experiment: RBCs in an extensional flow 89
4.3.1 Introduction 89
4.3.2 Design of the extensional flow 90
4.3.3 Numerical setup and operating points 94
4.3.4 Initial state of the RBC in the crossflow device 99
4.3.5 Experimental case's preliminary results using tank treading initial shape and outcomes 100

4.1 Introduction

Internal dissipation and membrane dissipation cannot be controlled individually in an experiment. This confusion has been reinforced by some modeling works. Keller and Skalak have notably developed a theoretical model for the dynamics of RBCs in shear flow [84], which has been extended to more complex cases later [1, 39, 104, 105, 150], in which internal viscosity and membrane viscosity act in the exact same manner, the two being combined in an effective RBC viscosity. Membrane viscosity has sometimes been used to account for the whole viscosity of the system. For example, Mancuso and Ristenpart [100] fit experimental data of RBCs stretched in a sudden contraction to extract the membrane viscosity of the RBC thanks to a model neglecting internal viscosity. Are internal viscosity and membrane viscosity equivalent? Do they contribute in the same way to the dissipation in the system? These questions are open, but numerical simulation of RBC dynamics can contribute to answering them, as we show in this study. The main goal of this part is to assess the impact of the membrane viscoelasticity on the whole RBC's behavior, for two canonical configurations. The first configuration is that of a single RBC in pure shear flow. While RBCs may exhibit different types of motion depending on the applied shear stress and external viscosity [103], we focus here on the specific dynamics obtained when the RBC is suspended in a viscous fluid (typically more than 3 times the viscosity of plasma) at moderate and high shear stresses. This configuration has been extensively studied experimentally, which enables to have numerous reference measurements from the literature to compare with. We are interested in the impact of membrane viscosity on the tank-treading regime. This study enables to highlight the lack of membrane viscosity in the classical numerical model. Moreover, thanks to the implemented viscoelastic model, it enables the reproduction of experimentally measured behavior. Finally, some conclusion about the shear thinning aspect of the membrane has been made. This work resulted in the publication of an article in Physical Review Fluids [102].

The second study concerns the deformation of the red blood cell placed in an extensional flow. It illustrates the interest of having a model considering the membrane viscosity to design relevant experimental devices for the measurement of this behavior. We will detail the design of the experimental device, the simulation devices as well as the first results obtained.

4.2 Effect of membrane viscosity on tank-treading red blood cells

4.2.1 Introduction

To compare the effect of internal viscosity and membrane viscosity, a relevant configuration is that of an RBC tank-treading in a shear flow, which has already been extensively studied experimentally [1, 56, 59], and numerically [30, 36, 37, 123, 125, 126, 163]. In a shear flow, when the suspending medium is viscous enough and for high enough shear stresses, the membrane circulates around the cell like the tread of a tank [84]. The RBC lengthens in the direction of the flow and adopts an almost constant angle with respect to the flow direction [1]. Tank-treading results are generally characterized in terms of RBC elongation, inclination angle and tank-treading frequency, measured experimentally by attaching a bead to the RBC membrane to track its circulation [54].

While simulations generally compare favorably with experiments in terms of elongation and inclination, tank-treading frequencies are overestimated in the absence of membrane viscosity in the model, as shown by Dodson and Dimitrakopoulos [36]. Because membrane viscosity contributes to internal friction in the membrane, it always opposes to the load. Moreover, it adds a delay between the load and the response. Implementation of an internal membrane dissipation is expected to slow down tank-treading motion, thus to decrease tank-treading frequencies.

The purpose of this study is to compare the dissipative sources in an RBC and to study their impact on the tank-treading behavior. Numerical simulations with and without membrane viscosity were performed to systematically assess its effect. The tank-treading configuration of interest is presented before detailing the results, focusing on the comparison between internal viscosity and membrane viscosity. A comparison with existing experimental results is also shown. Finally, experiments and simulation results are combined to infer the effective value of membrane shear viscosity in this configuration of tank-treading RBCs.

4.2.2 Numerical setup and operating points

Simulations of single red blood cells under pure shear are performed. The configuration is represented in Fig. 4.1. An external shear flow $\vec{u} = \dot{\gamma} y \vec{e_x}$ is imposed in

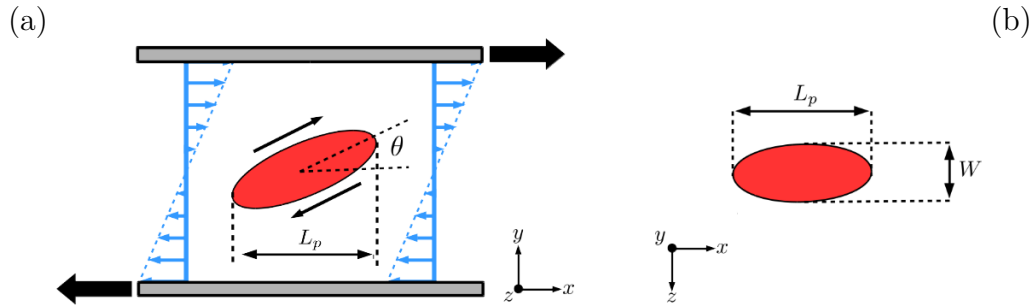

Figure 4.1: Representation of the tank-treading behavior. (a) Side view, enabling the measurement of the inclination angle θ. Translating walls are located at the top and bottom boundaries. (b) Top view, for the measurement of the deformation index $D = \frac{L_p - W}{L_p + W}$.

a periodic domain closed by moving walls. The domain is a cube of edge 30 µm. The fluid inside and outside the membrane may have different values of viscosity. The RBC is biconcave at rest, with diameter 7.6 µm. Its volume is 93.9 µm^3 and its surface area 135 µm^2. Concerning the internal fluid viscosity, the literature does not provide very precise values at ambient temperature. Viscosity values between 7 cP and 15 cP are reported for hemoglobin solutions [22, 112, 113] for temperatures between 20°C and 25°C, for a hemoglobin concentration between 330 g l^{-1} and 360 g l^{-1}. In this work, a value close to 11 cP will be used where dimensional results are presented (sections 4.2.4 and 4.2.5).

In this study, the RBC without membrane viscosity and with fixed mechanical properties is chosen as a reference to highlight the impact of the lack of dissipation in the model. For every simulated RBC presented in this study, the Skalak shear modulus value is fixed to $G_\infty = 2.5 \times 10^{-6}$ Pa.m [88, 103]. The bending modulus E_b is fixed to 6.0×10^{-19} J, which allows to slightly extend the upper bound in Ca for which stable results can be obtained without membrane viscosity. This value is higher than the classically measured value (around 2.0×10^{-19} J), but such values of increased bending modulus are regularly used in the literature [27, 28, 30]. In the capillary range used in this study, we found no impact of E_b on the deformation index D and the tank-treading frequencies. Using those parameter values, the initial biconcave shape is obtained by defining the stress-free shape of the RBC as an oblate ellipsoid[30] with an axis ratio of 0.9 and the same surface area as the RBC at equilibrium and by deflating the stress-free shape to the RBC volume of 93.9 µm^3 to obtain the equilibrium shape [30, 124]. Finally,

regarding the viscoelastic RBCs, the viscoelastic branch shear modulus is set to $G_H = 50 \times G_\infty$, so that the model behaves almost like a Kelvin-Voigt model, which is often done in numerical simulations [68, 78, 124].

The RBC membrane is discretized with 3919 triangles with a characteristic element size of 0.3 µm. To ensure the accuracy of the immersed boundary method, the characteristic size of the fluid mesh is the same [131]. The RBC, initially at rest, is subjected to the shear flow at $t = 0$. After a brief transient phase, the shape of the RBC and its inclination angle θ reach a quasi-steady state, with small oscillations due to the circulation of the stress-free shape of the membrane [1, 104]. The deformation is characterized with a deformation index calculated from the top view (in the (x,z) plane) $D = \frac{L_p - W}{L_p + W}$ (see Fig. 4.1). The tank-treading frequency f_{TT} (in s^{-1}) is also extracted. Simulations are performed for a total of $150\,t^*$ with $t^* = \dot{\gamma}t$ the non-dimensional time. D, θ and f_{TT} are computed over the last $120\,t^*$.

In this study, we vary the external shear rate $\dot{\gamma}$, the external viscosity μ_{ext}, the internal viscosity μ_{int} and the membrane viscosity η. The other parameters of the model (geometry, mechanical properties) are considered fixed and are representative of an average value for RBCs. We thus ignore natural variability or the effect of age on these RBC characteristics [15, 88]. On the other hand, a systematic study of the effects of membrane viscosity and internal viscosity is performed.

Parameters for the simulations will be expressed in terms of non-dimensional numbers. As for the case with capsules, the non-dimensional numbers of the problem are the Reynolds number Re, the capillary number Ca, the viscosity ratio λ and a Boussinesq number characterizing the membrane viscosity. Concerning RBCs, we chose to use the internal Boussinesq number $Bq_{int} = \frac{\eta}{a\mu_{int}}$, with a =2.82 µm the radius of a sphere of the same volume as that of the RBC, 93.9 μm^3. This non-dimensional number compares the membrane viscosity with the internal fluid viscosity. Here, it is preferred to the external Boussinesq number, as Bq_{int} characterizes the RBC only, independently of its environment. As for capsules, the Reynolds number was fixed to a small value of 0.2 to shorten the computation times without introducing fluid inertia effects. However, this choice may lead to a slight overestimation of the tank treading frequencies.

The purpose of this study is to highlight the impact of both λ and Bq_{int} on the dynamics of tank-treading RBCs, for different values of Ca. Increasing either λ or Bq_{int} is expected to produce similar effects associated with an increase of

Name	λ	Bq_{int}	Ca	Figure
L02B0	0.2	0.0	0.6, 1.8, 4.0, 7.2	Fig. 4.4(a,b)
			0.6, 2.0, 4.0	Fig. 4.2(a-c)
L05B0	0.5	0.0	0.5, 1.6, 2.4, 4.0, 7.2	Fig. 4.4(a)
			0.6, 2.0, 4.0	Fig. 4.2(a,c)
L1B0	1.0	0.0	0.6, 1.6, 2.4, 4.0, 7.2	Fig. 4.4(a)
			0.6, 2.0, 4.0	Fig. 4.2(a-c)
L02B1	0.2	1.0	0.6, 1.8, 4.0, 8.5	Fig. 4.4(b)
			0.6, 2.0, 3.0, 4.0	Fig. 4.2(a-c)
L02B3	0.2	3.0	0.6, 1.8, 4.0, 8.5	Fig. 4.4(b)
			0.6, 2.0, 3.0, 4.0	Fig. 4.2(a-c)
L02B5	0.2	5.0	0.6, 2.0, 3.0, 4.0	Fig. 4.2(a-c)
L084B0	0.84	0.0	0.6, 1.0, 2.0, 3.8	Fig. 4.4(c)
L084B1	0.84	1.0	0.6, 1.0, 2.0, 3.8	Fig. 4.4(c)
L084B3	0.84	3.0	0.6, 1.0, 2.0, 3.8	Fig. 4.4(c)

Table 4.1: Recap of the simulations used in the non-dimensional and dimensional studies.

the total dissipation in the RBC. A recap of the computations done in this study can be found in Tab. 4.1.

The numerical results are presented in two different ways: first, in a non-dimensional framework to present the impact of the membrane viscosity on the characteristics of a tank-treading RBC and to highlight the difference between the effects of internal and membrane viscosities. Then, results are presented in a dimensional way to enable the comparison with experimental data on the tank-treading frequency.

4.2.3 Non-dimensional study

In this non-dimensional study, results are presented in terms of the inclination angle θ, deformation index D and non-dimensional frequency $f^*_{TT} = \dfrac{4\pi f_{TT}}{\dot{\gamma}}$ [162, 163], as a function of Ca. We will highlight how the characteristics of tank-treading depend on λ and Bq_{int}, *i.e.* of the internal viscosity and the membrane viscosity. To do so, the following ranges of non-dimensional parameters were considered. The range of Ca is from 0.3 to 2.0, in particular to avoid the low-Ca region, where tank-treading is not stable and out-of-plane motions and deformations are possible [40, 105]. In addition, high values of the capillary number yield sharp shapes of RBCs [54] which may be unstable at the tip. Concerning the range of λ, it is

well known that the tank-treading behavior is not stable anymore for λ values greater than 2.5-3.0 [3, 87, 103, 105]. In addition, experimental studies of the tank-treading behavior are generally performed in dextran solutions, with a high external viscosity [56]. As a consequence, the range of λ was chosen to be between 0.2 and 1.0. Finally, Bq_{int} values were chosen between 0 (no membrane viscosity) and 5.0, for which the tank-treading frequency is largely decreased (see further).

Computational results from the L02B0, L05B0, L1B0, L02B1, L02B3 and L02B5 series are displayed in Fig. 4.2. First, the deformation index is not very sensitive to the value of λ and Bq_{int} (see Fig. 4.2b), in particular at low values of Ca. At higher values of Ca, both λ and Bq_{int} have the same effect of slightly decreasing the deformation. However, Fig. 4.2(a,c) show a different effect of λ and Bq_{int} on the tank-treading frequency and on the inclination angle. In particular, differences are more pronounced on the frequency (Fig. 4.2c). Fig. 4.2(c) first shows that the non-dimensional frequency decreases when Ca increases: the tank-treading frequency is not linear with respect to Ca (a linear dependency would correspond to constant f^*_{TT} in Fig. 4.2c). This has also been obtained in simulations without membrane viscosity [163]. Fig. 4.2(c) also highlights the differences between an increase in internal viscosity or in membrane viscosity. While both lead to a decrease of f^*_{TT}, this decrease is rather uniform when increasing λ, but not increasing Bq_{int}. Membrane viscosity has a mild effect at low shear stresses, but its influence increases with shear stress. The same comments can be made on the effect of λ and Bq_{int} on the inclination angle (Fig. 4.2a).

From the modeling point of view, the consequence is that membrane viscosity and internal viscosity are not interchangeable. For instance, for tank-treading, one cannot properly mimic membrane viscosity by increasing internal viscosity, contrary to what may be suggested in low-order models and in specific situations [84, 100]. As a matter of fact, it is possible to obtain similar tank-treading frequencies from two different RBCs, as illustrated by comparing L1B0 and L02B3 at $Ca = 2.0$. Even the shapes are pretty similar, despite little differences that can be seen in Fig. 4.3. However, the similarity is only possible for a given Ca and does not hold for a whole range of Ca (see how the L1B0 and L02B3 trajectories differ with varying Ca in Fig. 4.2c). In other words, it is not possible to infer internal viscosity value or membrane viscosity value using only one RBC and only one value of Ca.

The difference between the impacts of the internal viscosity and of the membrane viscosity has been highlighted in the non-dimensional analysis. Now, it

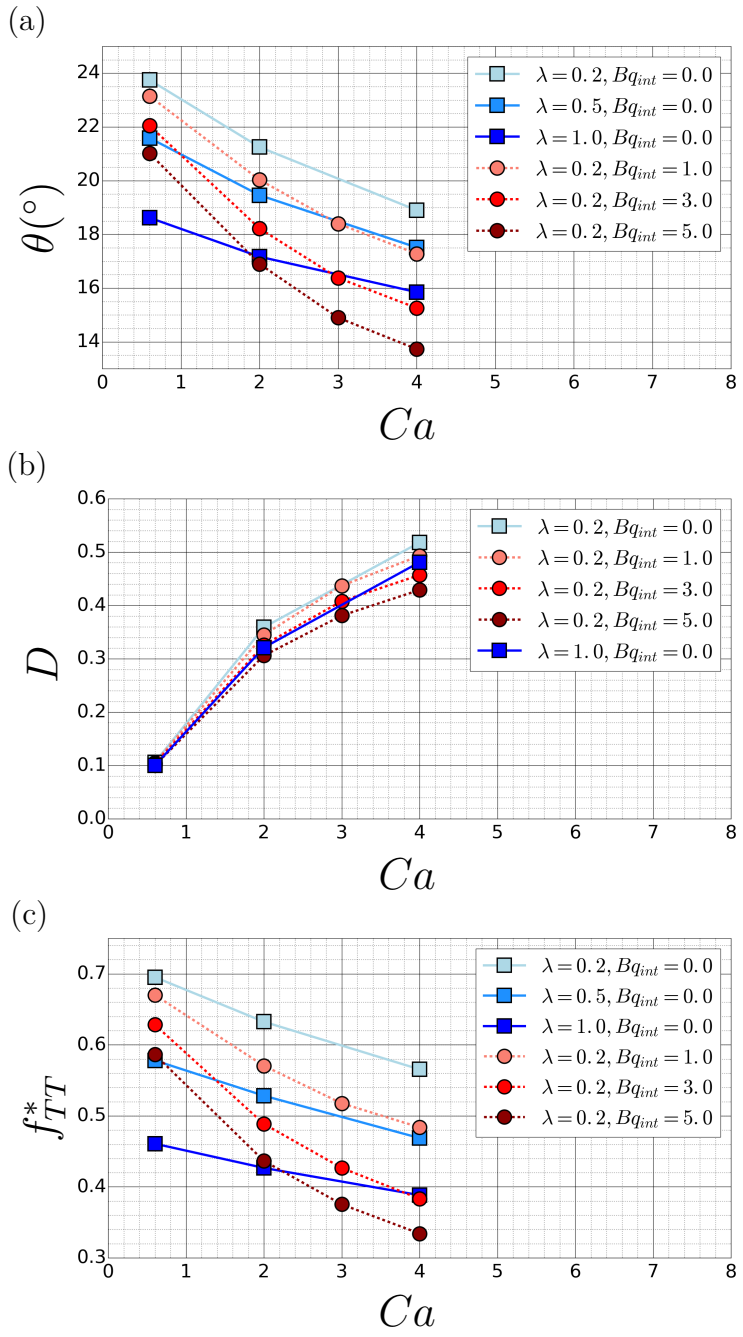

Figure 4.2: Impact of the internal viscosity and the membrane viscosity on the tank-treading characteristics of a single RBC in shear flow as a function of Ca. (a) Inclination of the RBC, (b) deformation index and (c) the non-dimensional frequency. Only chosen data are represented on (b) to improve clarity.

is interesting to study the consequences of those differences in comparison with experimental data in a dimensional framework. To do so, we will make the

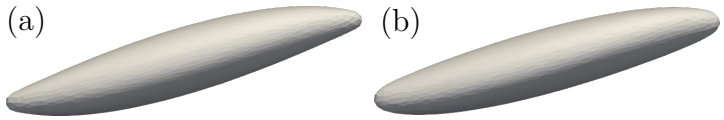

Figure 4.3: RBC shape comparison at $Ca = 2$ for L1B0 (a) and L02B3 (b). Corresponding values of D are 0.48 for L1B0 and 0.46 for L02B3. Corresponding f^*_{TT} is about 0.38 for both. Shape differences can mostly be seen on the extremities of the RBC. Different combinations of λ and Bq_{int} yield almost identical cells, but for a given value of Ca only.

non-dimensional data (Tab. 4.1) dimensional to match experimental operating conditions.

4.2.4 Dimensional study

As previously explained, tank-treading is classically characterized by three main parameters: the tank-treading frequency f_{TT}, the deformation of the RBC represented by its deformation index $D = \frac{L_p - W}{L_p + W}$ and the inclination angle between the RBC and the flow direction θ. Here we specifically compare simulation results with experiments in terms of frequency, for which differences between the impacts of internal and membrane viscosities have been emphasized, and for which data is available in the literature. Experimental data for tank-treading frequencies are extracted from Fischer's work [56]. In this study, tank-treading experiments are performed with three different blood samples, for multiple external fluid viscosities and different shear rates, at a room temperature of 23°C. We selected cases with external fluid viscosity of 12.9 cP and 53.9 cP. Assuming that the internal viscosity of the RBC is $\mu_{int} = 10.78$ cP, which is an acceptable value at ambient temperature (see section 4.2.2), such values of external viscosity correspond to $\lambda = 0.84$ and $\lambda = 0.2$, respectively. Results are presented in Fig. 4.4(a-c). Experimental results are presented in terms of average and error bars from Fischer's data [56]. Blood samples used in this study come from three different donors. As experimental data are dispersed both in terms of tank-treading frequency and shear rate at which it is measured, mean values and standard deviation were computed for each cloud of data and reported in Fig. 4.4.

First, it is seen in all subfigures that for the cases without membrane viscosity, the tank-treading frequency is overestimated with respect to the experimental data. This is consistent with existing results from the literature [36]. Then, an

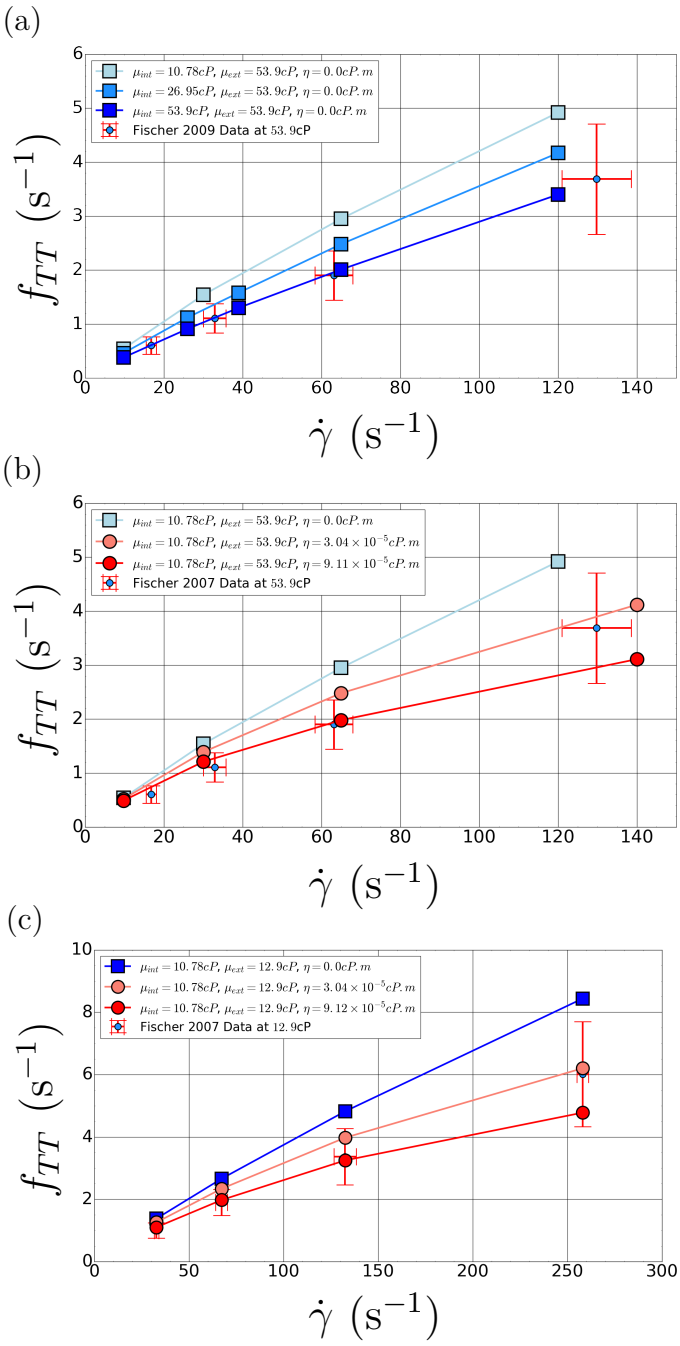

Figure 4.4: Comparison between computational and experimental results. (a) Impact of the internal fluid viscosity on tank-treading frequencies for an external viscosity of $\mu_{ext} = 53.9$ cP. (b) and (c) Impact of the membrane viscosity on frequencies for two different external viscosities ($\mu_{ext} = 53.9$ cP (b) and $\mu_{ext} = 12.9$ cP (c)). Error bars represent two times the standard deviation observed experimentally.

increase either in the internal viscosity or in the membrane viscosity leads to a decrease in the tank-treading frequencies, as shown for the case with $\mu_{ext} = 53.9$ cP (Fig. 4.4a,b): additional dissipation in the RBC slows down the membrane circulation, whatever the source for this extra dissipation. It is interesting to comment the value of the internal viscosity and membrane viscosity needed to get results close to the experiments: Fig. 4.4(a) shows that, to obtain simulation results comparable with experimental measurements, we have to increase the internal viscosity up to a value of 53.9 cP. This value is typically five times the expected value of the internal viscosity, which is unrealistic: even if some uncertainties exist on the value of internal viscosity, this value is not consistent with the expected range. In addition, if such a high value of internal viscosity is used with $\mu_{ext} = 12.9$ cP, tank-treading is not obtained anymore as the viscosity contrast is too high [87, 103]. As a consequence, we do not present results increasing the internal viscosity with $\mu_{ext} = 12.9$ cP. Indeed, results at $\mu_{ext} = 12.9$ cP Fig. 4.4(c) shows that the same range of membrane viscosity yields favorable comparison with experiments. Consequently, membrane viscosity seems indispensable to explain the behavior RBCs during tank-treading.

Fig. 4.4(b,c) allow detailing the impact of the membrane viscosity on tank-treading frequency. Interestingly, the effect of membrane viscosity is not uniform with different shear rates, as reported in the non-dimensional analysis. At low shear rates, the tank-treading frequencies seem relatively unaffected by membrane viscosity. The effect of membrane viscosity is all the more important that shear rate (and thus tank-treading frequency) increases. This is true for both $\mu_{ext} = 53.9$ cP (Fig. 4.4(b)) and $\mu_{ext} = 12.9$ cP (Fig. 4.4(c)).

In the series of simulations presented in Fig. 4.4, we have fixed the ratio between the membrane viscosity and the internal viscosity (in other terms, the internal Boussinesq number Bq_{int}) to three different values: $Bq_{int} = 0.0, 1.0$ and 3.0. It leads to three different η values, 0.0 cP.m, 3.04×10^{-5} cP.m and 9.11×10^{-5} cP.m, respectively. Clearly, $\eta = 3.04 \times 10^{-5}$ cP.m and $\eta = 9.11 \times 10^{-5}$ cP.m yield better results than $\eta = 0.0$cP.m, and this range of membrane viscosity yields fair comparisons with the experiment. However, the evolution with shear rate of the relative impact of the membrane viscosity on the results makes results at $\eta = 3.04 \times 10^{-5}$ cP.m (pink curve in Fig. 4.4(b,c)) better at high shear rates and results at $\eta = 9.11 \times 10^{-5}$ cP.m (red curve in Fig. 4.4(b,c)) better at low shear rates. Note that this statement seems independent of the value of external viscosity.

To conclude, even if imposing a large value of internal viscosity can reproduce experimental tank-treading frequencies in some cases, membrane viscosity is the only source for dissipation enabling a consistent improvement of the agreement between simulations and experiments for a large range of operating conditions. Indeed, the values of membrane viscosity that yield a satisfactory comparison with experiments are similar to those extracted by Tran-Son Tay [155]. However, they are higher than the values used by Guglietta *et al.* [68] to predict relaxation experiments. However, a constant membrane viscosity does not lead to a perfect agreement between experiments and simulations. This result suggests that a viscoelastic modeling of the membrane with a constant shear viscosity is not enough, and that a more complex membrane viscosity behavior should be accounted for. The idea of a shear-thinning behavior for the RBC membrane is not new. Chien *et al.* [24] reported a shear-thinning behavior of the membrane from micropipette experiments. Tran-Son Tay *et al.* [155] studied the shear-thinning behavior of the RBC's membrane in the case of tank-treading RBCs and studied differences of viscosity for young and old cells using the analytical model from Keller and Skalak [84]. The variation of the apparent membrane viscosity with the shear is discussed from our results in the next section.

4.2.5 Shear-thinning model

Results obtained with a constant membrane viscosity suggest that higher values of membrane viscosity are needed for low shear rates to reproduce experimental tank-treading frequencies. This is in line with previous experimental works pointing out the shear-thinning behavior of the membrane [24, 155].

In this section, the value of membrane viscosity is inferred from the comparison between numerical predictions of the tank-treading frequency and experimental data[56] already reported in Fig. 4.4, at different values of the external viscosity. We use a unique red blood cells with fixed characteristics except for the membrane viscosity. For each experimental cloud (at approximatively 15, 35, 65, 130 and $260\,\mathrm{s}^{-1}$, see Fig. 4.4), we use the ensemble average of the shear rate as a reference. For that shear rate, simulations with different values of the membrane viscosity are performed and the tank-treading frequency is compared to the ensemble average of each cloud (this data is plotted as blue dots in Fig. 4.4). By dichotomy, we converge to an inferred value of membrane viscosity. The value was considered to be accurate if the difference between the numerical and the experimental

frequencies was less than 5%. The results of this process in terms of frequencies are displayed in Fig. 4.5(a,b). Fig. 4.5(c) shows the inferred values of membrane viscosity as a function of the shear rate, for $\mu_{ext} = 12.9$ cP and $\mu_{ext} = 53.9$ cP. In addition to the value of membrane viscosity yielding a good comparison with the average frequency in the experiment, we use simulations to extract a dispersion on the values of membrane viscosity (displayed in bars in Fig. 4.5c) from the dispersion of the experimental data. Experimental dispersion is measured using the standard deviation of the data Δf_{TT}. In simulations, we calculate how a change in membrane viscosity changes the resulting tank-treading frequency: this means calculating $\partial f_{TT}/\partial \eta$ at the inferred membrane viscosity. We define the dispersion in membrane viscosity as $\Delta\eta = \Delta f_{TT} \times \partial\eta/\partial f_{TT}$.

Fig. 4.5(c) leads to confirm the shear thinning behavior of the membrane, with a factor of 10 between maximum and minimum viscosity values. Moreover, error bars are bigger as the shear rate decrease. It leads to highlight that the membrane viscosity seems to be a more sensitive parameter as the shear rate increase. Finally, Fig. 4.5(c) also shows that the external fluid viscosity does not seem to have a major impact on the shear thinning curve. Note that at low shear rates, a large change in the membrane viscosity is needed to change the resulting tank-treading frequency, which may explain the largest differences seen at $\dot{\gamma} \approx 30$ s $^{-1}$.

Tran-Son Tay [155] made a similar effort to extract membrane viscosity from experimental data and a model. The corresponding results are also displayed in Fig. 4.5(c). Even if differences exist between Tran-Son Tay's results and our results, the trends are similar, even using very different methods to obtain those shear-thinning curves. In comparison, values of membrane viscosities computed with YALES2BIO seem closer to the values for young cells, at high shear rates. The values of membrane viscosity of Fig. 4.5(c) also seem to be consistent with the one used by Guglietta *et al.* [68] in their simulations of RBC relaxation ($\eta = 3.18 \times 10^{-4}$ cP.m), which could then be interpreted as a value relevant to slow deformations of the membrane. Finally, using values obtained thanks to the tank-treading behavior to compute relaxation time, it leads to characteristic times between 0.1 s and 0.01 s, which is in accordance with literature values [68].

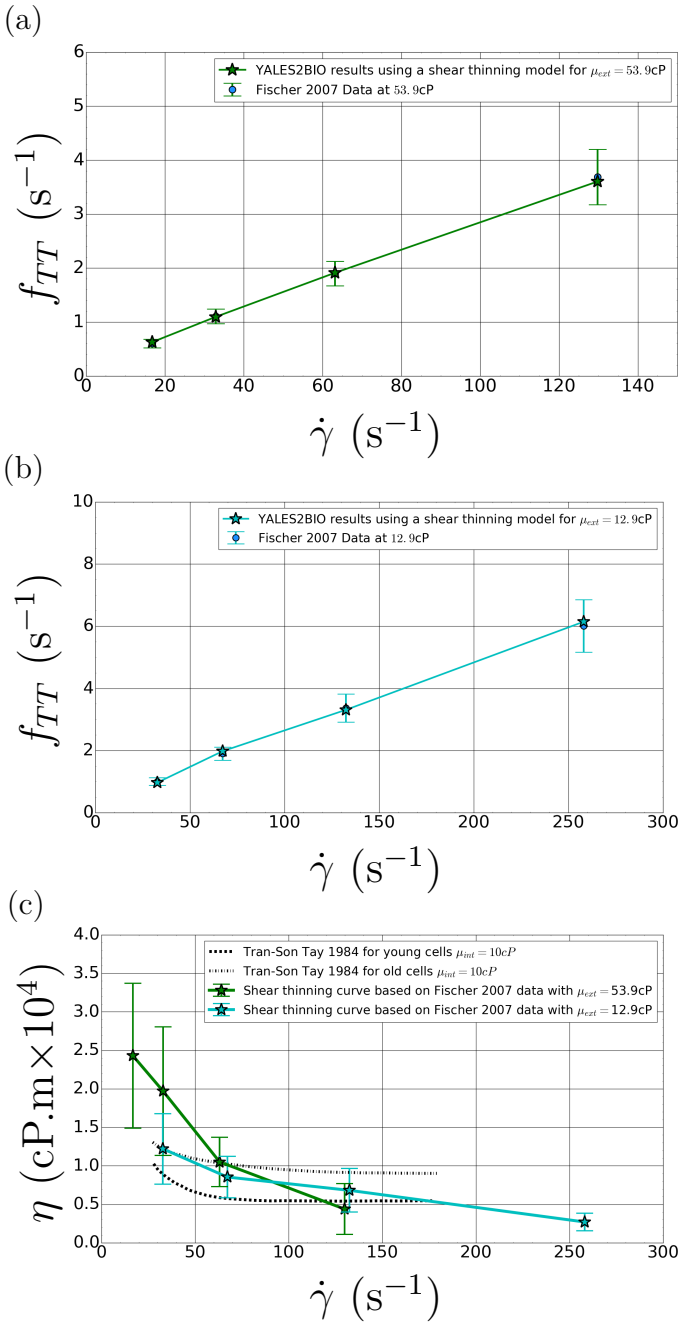

Figure 4.5: Comparison between the experimental frequencies[56] and the simulation frequencies obtained from the inferred membrane viscosity values. (a) Comparison with data at $\mu_{ext} = 53.9$ cP, (b) comparison with data at $\mu_{ext} = 12.9$ cP. (c) Inferred shear-thinning behavior of the membrane viscosity; values from Tran-Son Tay[155] are included for comparison. Bars in (a) and (b) represent the standard deviation of the experimental data. Bars in (c) represent the range of value of membrane viscosity to reproduce the dispersion of the experimental frequencies.

4.3 Strain experiment: RBCs in an extensional flow

4.3.1 Introduction

The goal of this part is to do the same kind of work as in the previous part concerning tank-treading, but on another configuration. Indeed, to improve our knowledge on the viscous behavior of the membrane, it is important to compare the current model to different configurations of RBCs in flow. Here the idea is to design an extensional flow to make a comparison between simulation and experimental results in a simple configuration of uniaxial extension. The study of the impact of membrane viscosity in strained RBC configurations has also recently appeared in the literature thanks to the work of Guglietta *et al.* (2021) [69].

The objective of the work initiated here is to study the response of an RBC stretched in one direction and without avoiding membrane circulation. This situation is obtained in purely extensional flows. A possibility to create a strain and, at a given flow, to reduce the size of the channel. This will accelerate the fluid creating a strain as it passes through the reduced section [100]. The advantage of this type of configuration is to be able to transport the RBC without major shape shift of the RBC upstream. However, the strain is brought to change throughout the passage of the RBC in the channel which is reduced. Another way to create purely extensional flow is by slowing down the flow.

One way to get such a flow is to use a kind of experimental device called crossflow devices [47, 63, 72, 119, 141]. The idea is to use crossing channels and an imposed inflow to produce a constant strain rate area at the center of the device.

This type of device has multiple advantages, in particular the fact of not requiring the addition of a new player to impose the force, as in the context of optical tweezers (the bead). Thus, the stress is controlled thanks to the parameters of the external fluids such as the viscosity or the inlet flow. On the other hand, unlike optical tweezers, it is not possible to solicit a resting RBC (in its discocyte form). Indeed, the delivery of the globule in the traction zone involves the deformation of the RBCs in the channel. Finally, it is also not possible to precisely center the red blood cells in the device. As a result, the RBCs undergo a stress which depends on their trajectory within the stretching zone. The challenge of this type of measurement is therefore to considering the arrival configuration of

the globule as well as its trajectory within the stretching zone.

The advantage of simulation is to be able to overcome experimental constraints and to allow the study of ideal cases. Therefore, it is completely possible to consider the case of the elongation of a RBC in its discocyte form perfectly centered in the extension zone.

We will therefore detail the design of the experimental device and present the flow inside the device. Then, different idealized configuration computed are presented to obtain a better understanding of the dynamics inside the device. Finally, we will present the preliminary results of simulations as well as the experimental results.

4.3.2 Design of the extensional flow

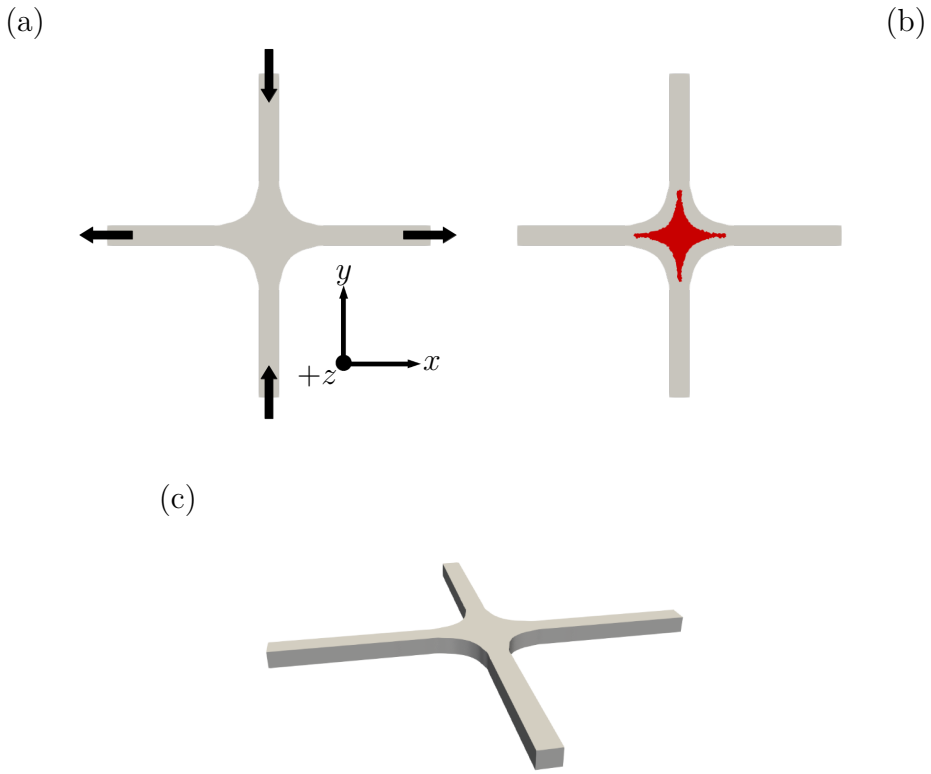

Figure 4.6: Visualization of the crossflow device with in (a) a top view with arrow representing inlets and outlets of the device, (b) a 80% threshold of the max strain rate and (c) a three dimensional view of the device showing the rectangular section of the channels.

We will present here the design of the experimental device used in this work. The issues are multiple. The centering of the RBC in the channel is not perfect experimentally. Therefore, we seek to generate a flow in which the region of uniform strain is as large as possible, so that slight changes in the trajectory would not have a major impact on the strain experienced by the cells. At the same time, we seek to have a sizing of the channels allowing to better center the blood cells arriving in the extensional zone. All these constraints naturally led us to design the experimental device to allow the implementation of an extensional flow with a stagnation point, also called crossflow.

It consists in two opposite inflows that encountered themselves in a middle area and that are evacuated using two other channels. The four channels are forming a cross, which gives the name to those kinds of flows. Those kinds of experimental devices have already been extensively studied during the 2010s, so the chosen design is based on those works [63, 72].

The geometry is displayed in Fig. 4.9. Channels sections are rectangular and measure 50μm of width by 40μm in depth. The choice of the channel size is linked to the issue of centering of the RBCs inside the device. Indeed, we seek to have RBCs as centered as possible so that they remain long enough in the uniform strain region. However, Iss *et al.* in 2019 suggest that, in confined channel, RBCs are self-centering [81]. It is to use this phenomenon, inside the upstream channel that leads RBCs inside the crossing part of the device, to maximize the number of centered RBCs that this channel section was designed. The crossing geometry was found by Galindo Rosales *et al.*, who suggest to replace angle of the cross by a rounded geometry. In this study, the rounded geometry come from circle of 100μm of radius. Finally, the crossing area measures 250μm of length and its diagonal measures 150μm.

Because the microfluidic system is only operated at low Reynolds numbers, the velocity field (and the strain rates) inside the device is linear with the inflow. The values are displayed in Fig. 4.8. One of the interests of the device is to create a large region of quasi-uniform strain. By showing different threshold filters on the strain rate parameter on the flow field inside the device, the constant strain area can be highlighted as in Fig. 4.9(c). Putting a threshold of 80% of the strain maximum value leads to obtain a region of 220μm of width by 15μm of depth. Setting a threshold to 90% leads to a region of width 150μm and of depth 5μm.

to visualize values of the strain rate that the RBC will undergo and residence time of the RBC inside the strain area, streamlines are extracted and quantities

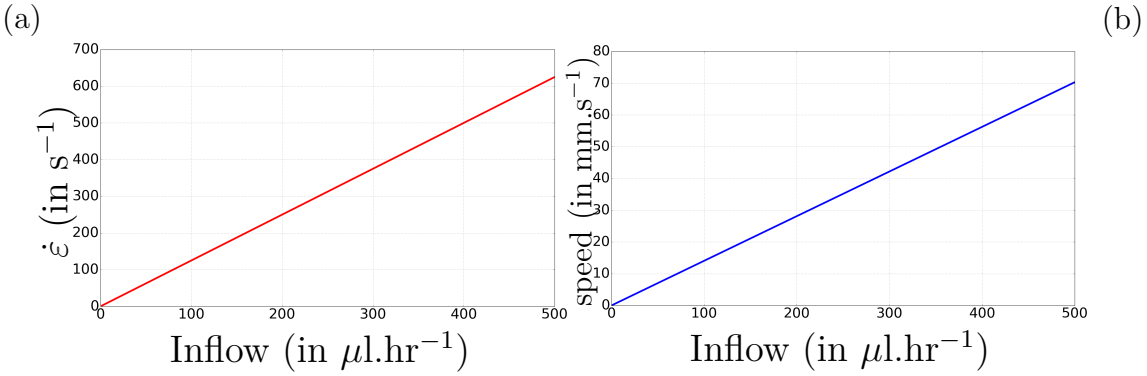

Figure 4.7: Relationship between the input flow rate and the strain $\dot{\varepsilon}$ (a), and the maximum velocity in straigth channels (b). The input flow rate represent the sum between the two channel inflows of the device, the velocity is maximum inside the inlets channels and the strain reported is the maximum value of the strain inside the strain area (at the center of the device).

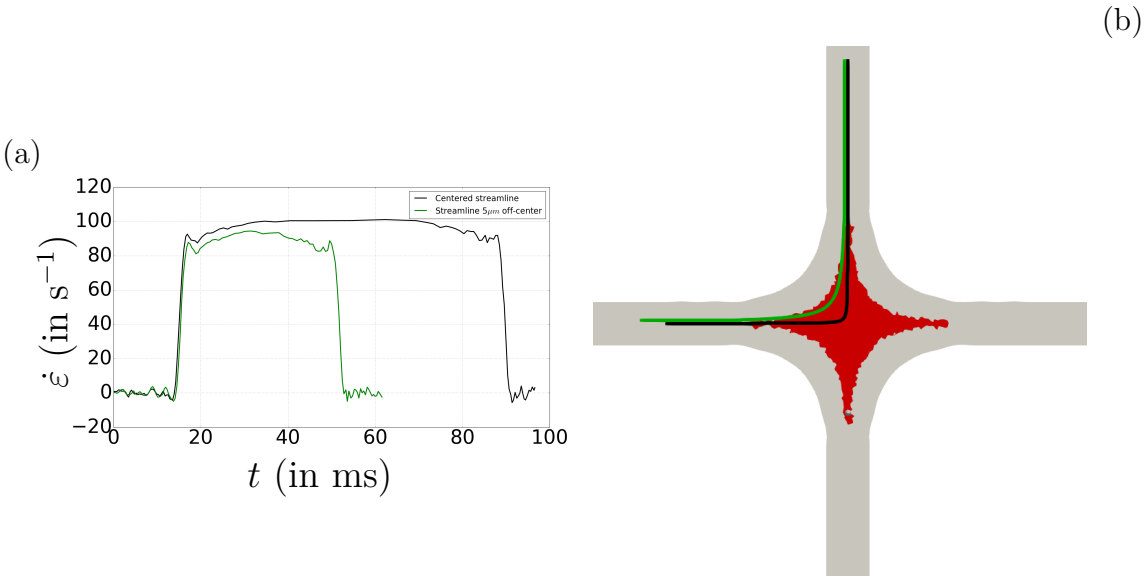

Figure 4.8: Information concerning the flow along a centered streamline and a streamline with 5 μm of shift in the showed plane inside the crossflow device for an imposed strain at 100 s^{-1}. (a) Strain rate $\dot{\varepsilon}$ as a function of time along the streamlines and (b) the crossflow device with in black the centered streamline, in green the shifted one and in red a threshold of 80% of the maximum strain rate.

of interest plotted against time, under the assumption that the RBCs perfectly follow the streamlines (Fig. 4.8). The two streamlines inspected are the perfectly centered streamline and the resulting streamline of an initial shift of 5μm. Fig. 4.8a

highlights that the residence time of a RBC inside the strain area is highly dependent on the streamline that the RBC follows. This means that centering of the RBC is critical in terms of applied stress and resulting deformation. This leads the RBC to undergo the same value of strain for approximately $10t^*$, with $t^* = t \times \dot{\varepsilon}$ the dimensionless time, knowing that the rise time is negligible compared to this total time.

Note also that RBCs will undergo maximum deformation if they are centered in the depth (z direction). Consequently, it is important to combine numerical simulations and experiments to carefully select centered RBCs, using both their position in the (x,y) plane (the imaging plane) and their velocity, which informs on their centering in the z direction.

Finally, a choice had to be made as to the viscosity of the external fluid used. We knew that the more viscous the external fluid, the less the effect of membrane viscosity would be apparent. This is because the external fluid will dissipate too much energy compared to the membrane viscosity. Thus, a pre-study, consisting in calculating some simplified cases at different external viscosities and different membrane viscosities, allowed us to note that from $\lambda = 1$, the effects of the membrane viscosity are visible. This leads this study to be done at $\lambda = 1$.

To conclude, let us recapitulate the advantages and limitations of this system with respect to our objectives. First, it is a purely fluidic system where RBCs will be stretched by a purely extensional flow. The RBC should undergo a constant strain during a relatively long time (several of non-dimensional time units). The application of this strain is relatively sudden, as the RBC enters the uniform strain region at high speed, which allows comparisons with simulations performed under constant strain. However, the RBCs need to be as centered as possible, otherwise they are subject to a lower strain rate and for a shorter time. A second difficulty is also inherent to the system: RBCs enter already stretched in the strain region. The numerical simulation of this configuration is treated in the next section. First, ideal cases are presented to gain a better understanding of the dynamics present when the RBC is stretched. The consideration of the deformed RBC before the arrival in the strain section is discussed at the end of the chapter as well as the experimental results.

4.3.3 Numerical setup and operating points

In numerical simulation, the problem of optimization of the computation time is always in the foreground. In our present case, a problem of scale difference between the fluid domain and the simulated red blood cell led us to think differently about our simulations. Indeed, to optimize IBM, it needs similar mesh size for the fluid and the solid. However, the size fluid domain that is needed to model a representative fluid domain in the experiment is simply too big in comparison to a RBC typical size. For example, streamlines shown in Fig. 4.8(c) are 500μm long, a good agreement for the RBC mesh size is 0.3μm. This scale problem quickly results in a unnecessary large mesh. The objective is therefore to faithfully represent the stresses undergone by the RBCs passing through the experimental device, without however reproducing the complete geometry of the device. To do that, two steps must be modelled to reproduce the experiment.

The first step consists of the generating the initial configuration of the RBC inside the entering channel. To do so, we use tank-treading RBC solutions from the simulations presented in the previous part of the chapter.

Now the RBC shape inside the entering channel is obtained, the strain that the RBC undergoes inside the center of the crossflow must be simulated too. To do that, we proceed in a similar way than before except that instead of using a fixed shear rate to compute the velocity field, we use a fixed strain rate. Thanks to the incompressibility of the fluid it leads to the calculation of the velocity field of the cubic domain as:

$$\overrightarrow{U} = \begin{bmatrix} U_x \\ U_y \\ U_z \end{bmatrix} = \begin{bmatrix} \frac{\partial U_x}{\partial x} \times x \\ \frac{\partial U_y}{\partial y} \times y \\ 0 \end{bmatrix} = \begin{bmatrix} \dot{\varepsilon} \times x \\ -\dot{\varepsilon} \times y \\ 0 \end{bmatrix}. \tag{4.1}$$

As already mentioned, this step is relevant when the reproduction of experimental observed RBCs is wanted. However, because the study is just starting out, it has not been possible during this thesis. Presented results in this section are preliminary results and illustrate outcomes of this study. Presentation of the different tools that had to be put in place to be representative of the experimental configuration are presented here to illustrate the difficulty to deal with simulations of RBCs. Simulations presented here are done with the same starting configuration and are here to help to identify dynamics that can be observed experimentally. This shape was chosen because it has a deformation index of 0.3, which is like the deformation indices observed experimentally in close regimes.

Concerning RBC's membrane mechanical parameters, except for the membrane viscosity, they are fixed thanks to the literature. The idea is to represent an RBC with average properties. By only distinguishing RBCs thanks to their membrane viscosity, it enables to highlight the impact of this behavior on the membrane deformability. Hence, the membrane elastic part of the behavior follows a Skalak behavior law. The corresponding shear modulus G_∞ is fixed to a value of $2.5\times10^{-}6$ Pa.m. The curvature modulus E_b is fixed to 2.0×10^{-19} J. Finally, to ensure that the viscoelastic membrane model is a Kelvin-Voigt model as presented earlier, the branch shear modulus G_{branch} is fixed to 50 times G_∞ (see Section (3.4.3) for more information on the subject). The RBC's membrane is a surfacing triangular mesh, and the fluid domain is a volumetric cartesian mesh. Concerning external fluid viscosity, in every simulation presented in this work we are considering that it is equal to the internal viscosity of the RBC. This leads to have the viscosity ratio number $\lambda = \frac{\mu_{int}}{\mu_{ext}} = 1$. All the simulations presented in this work were carried out with similar mesh parameters. The characteristic size of fluid and solid meshes is 0.25μm. Each simulation took between 1 and 2 full days depending on the strain applied (low strains requiring 2 days).

Most of the parameters are constant between each simulation and follows the value given earlier. Only the starting configuration of the RBC, the value of the strain applied as well as the viscosity of the membrane varies between simulations. Three starting configurations are explored during this study as well as three different Ca and three different Bq_{int}. The first configuration considers the starting shape as a discocyte with the lobes along the z axis. The second orientation is a discocyte with the lobes along the y axis (please refer to Fig. 4.8 for the representation of the axis in the device flow). Finally, the last configuration is a RBC in a tank treading shape close to the arrival configuration of the RBC observed experimentally. The different values of Ca used are $0.085, 0.17$ and 0.25. Finally, the three values of Bq_{int} studied are $0, 1$ and 5 for the most viscous configuration. The observed parameter is the deformation index D, computed using only a projected image of the RBC following the axis orthogonal of the flow plan. Indeed, experimentally, only this side of the RBC can be observed. Using this projection, D is computed as $D = \frac{L-l}{L+l}$ with L the length in the strain axis and l the length in the compressed axis (respectively the x and y axis presented Fig. 4.8). The evolution of D as a function of $t^* = \dot{\varepsilon}\, t$, with $\dot{\varepsilon}$ the strain at the center of the device.

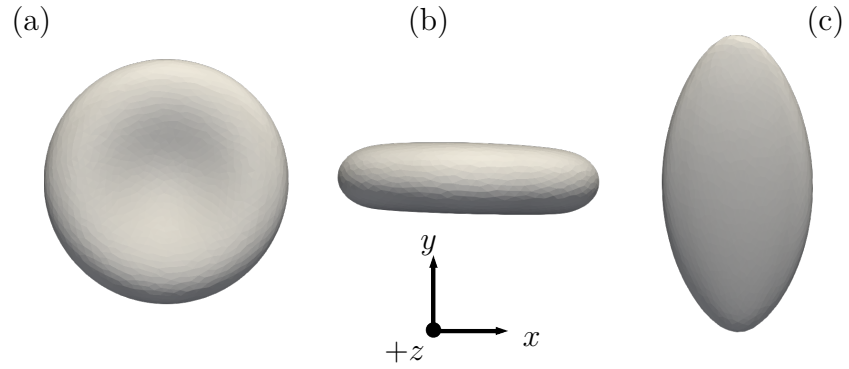

Figure 4.9: Visualization of the three simulated configurations in this work. The x axis representing the strain axis and y axis the compression axis. The first and the second orientation of the ideal cases are respectively represented on (a) and (b). (c) represents the configuration with a RBC in tank-treading shape.

Ideal cases: First orientation

In this first RBC orientation, the lobes are in the unconstrained direction, i.e. normal to the plane of the flow. Results are presented in Fig. 4.10. First, the membrane viscosity does not modify the asymptotic deformation of the RBC. However, the addition of the membrane viscosity delays the membrane deformation in comparison with the pure elastic case, as expected. The impact of the membrane viscosity seems to be more important as a function of the strain rate increases.

Note that the deformation index curves exhibit multiple regimes. This is due to a geometrical effect displayed in Fig. 4.11. Thanks to this visualization, it is now possible to have a better understanding of the shape of the D curves. Indeed, a phenomenon like buckling is happening, with an inversion of the curvatures near the two initial lobes. The impact of the viscosity on this peculiar phenomenon is not clear yet, although the whole phenomenon seems delayed due to the viscosity.

to quantify the additional delay between applied stress and resulting strain due to membrane viscosity, we use an exponential fit of the type $D(t^*) = D_\infty(1 - exp(-t^*/t_s^*))$, with t_s^* a non-dimensional stretching characteristic time and D_∞ an asymptotic value. This fit is used on the initial part of the curve, for $t^* \leq 2.0$, which is necessary to avoid having the fit spoiled by the second regime of buckling of the shape. As D never reaches the asymptotic value of the first deformation regime, D_∞ is a free parameter. The only constraint is that it has the same value for the cases at the same Ca (same strain rate), whatever the value of Bq_{int} (*ie* of membrane viscosity). The values of characteristic time are reported in Table 4.2.

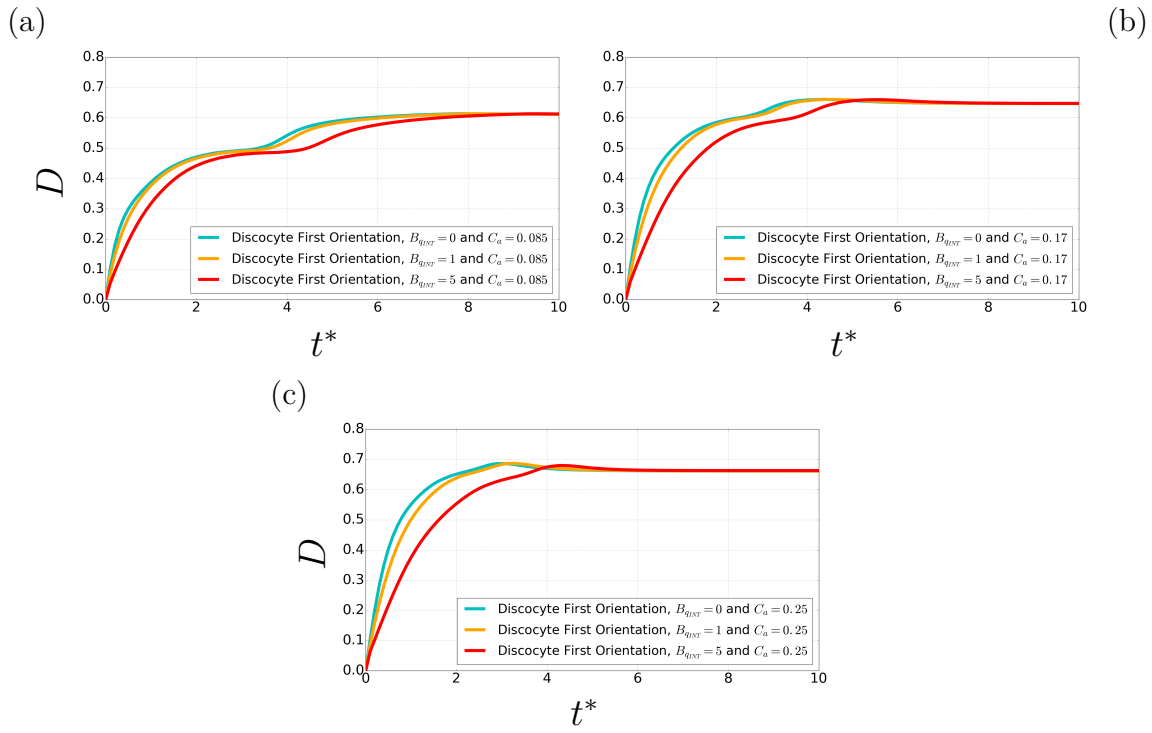

Figure 4.10: Deformation index as a function of the dimensionless time for three different Ca values obtained by simulation of a discocyte in the first orientation configuration. (a) Ca=0.084, (b) Ca=0.17 and (c) Ca=0.25.

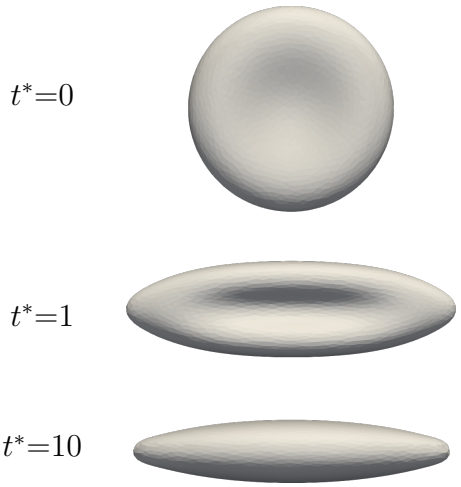

Figure 4.11: Visualization of the RBC shape at different t^* for the first orientation computation, at $Ca = 0.25$ for a pure elastic membrane, $Bq_{int} = 0$.

To conclude, this case highlights the fact that membrane viscosity may have a major impact on the response to stretching. One can observe the clear lengthening

	$Bq_{int} = 0.0$	$Bq_{int} = 1.0$	$Bq_{int} = 5.0$
$Ca = 0.085$	$t_s^* = 0.55$	$t_s^* = 0.62$	$t_s^* = 0.91$
$Ca = 0.17$	$t_s^* = 0.55$	$t_s^* = 0.68$	$t_s^* = 1.08$
$Ca = 0.25$	$t_s^* = 0.56$	$t_s^* = 0.72$	$t_s^* = 1.30$

Table 4.2: Non-dimensional characteristic time t_s obtained thanks to an exponential fit on the initial part of the deformation dynamics ($t^* \leq 2.0$).

of the characteristic times, typical of the effects of dissipation and delay introduced by the addition of a membrane viscosity Tab. 4.2. The values of Bq_{int} chosen however to remain within the reasonable range, much larger values having already been used in the previous study on the tank-treading behavior as well as in the literature [68]. In the elastic case, the characteristic time does not depend on the capillary number. On the contrary, it is seen to increase with the capillary number when the membrane is viscoelastic. However, this ideal case also displays complex geometrical effects due to the buckling of the RBC. Those effects lead the interpretation of the local impact of the membrane on the RBC's membrane complex. to limit the influence of buckling on the results, we also perform another set of simulations with a different orientation: the RBC small axis (the thickness direction) is along the compression axis of the extensional flow.

Ideal cases: Second orientation

In this orientation, the lobes of the RBC are oriented in the direction of compression. The purpose of this choice is to limit the impact of the effects observed previously, namely the inversion of the lobes, on the deformation curves. The same operating points are simulated. The results obtained are visible in Fig. 4.12. The deformation parameter is calculated in the shear plane, so that it is not zero initially.

What we notice is, first of all, the same obvious impact of membrane viscosity on the rate of deformation over time. The shapes of the curves are also very different compared to the first orientation. As for the previous case, however, several regimes are visible, due to the buckling of the RBC dimples, displayed in Fig. 4.13.

The study of these ideal cases confirmed the relevance of the study of such a configuration to study the impact of the membrane viscosity.

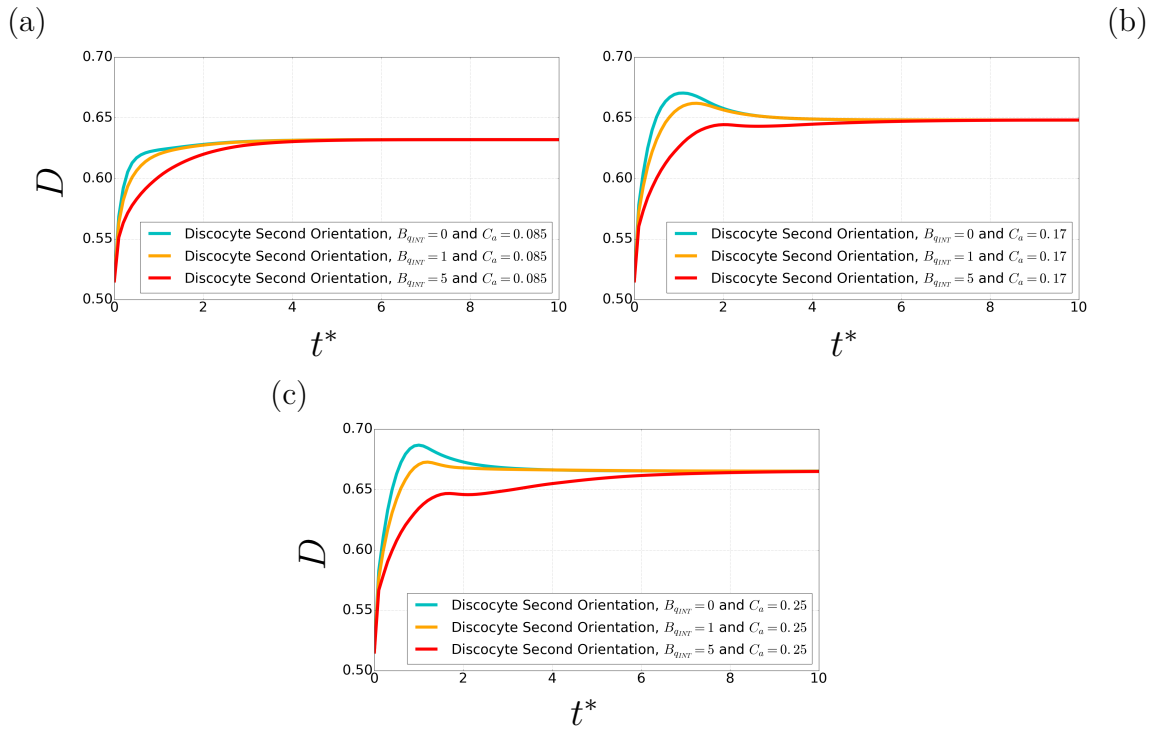

Figure 4.12: Deformation index as a function of the dimensionless time for three different Ca values obtained by simulation of a discocyte in the second orientation configuration. (a) Ca=0.084, (b) Ca=0.17 and (c) Ca=0.25.

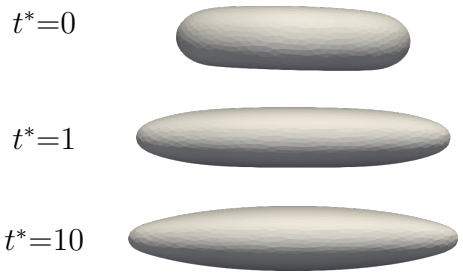

Figure 4.13: Visualization of the RBC shape at different t^* for the second orientation computation, at $Ca = 0.25$ and $Bq_{int} = 0$.

4.3.4 Initial state of the RBC in the crossflow device

Ideally, one would want to perform stretching tests starting from a non-deformed state. This is the case in simulations, where an RBC can be deposited instantaneously in a constant strain flow. Experimentally, because it is not possible yet to just directly inject the RBCs in the straining zone, the RBCs have to come to the crossing section by the entering channel. Indeed, Fig. 4.7 shows that

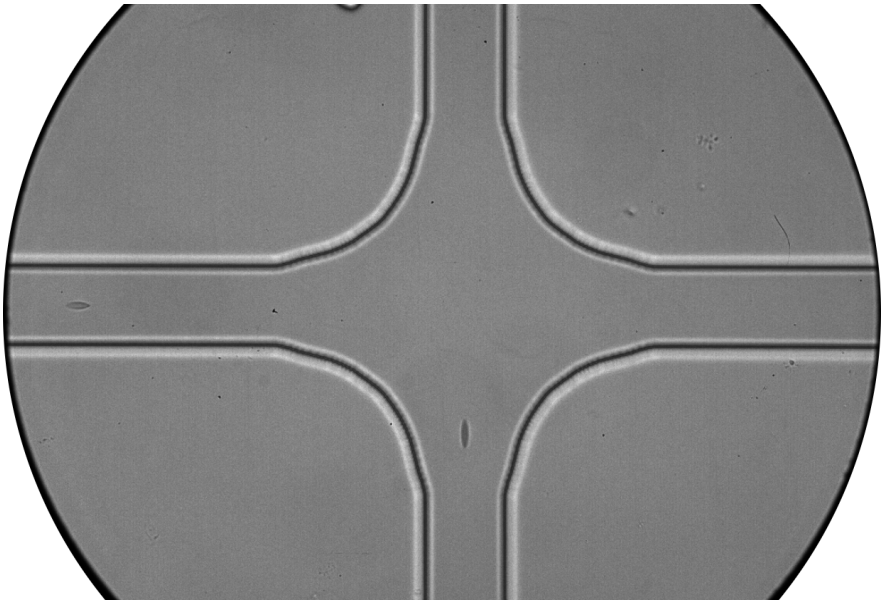

Figure 4.14: Photo of the crossflow device in operation. The horizontal channel is the input channel for the RBCs, a RBC is visible in the channel to the left of the image. An RBC after passing through the strain zone is visible at the bottom of the image, towards the exit channel.

to apply strain rates of the order of 100 s^{-1}, the maximum velocity inside the incoming channel is of the order of 10 mm s^{-1}, which yield shear rates in the channels of the same order as the strain rates targeted in the device. Indeed, when RBC are suspended in a viscous fluid, they arrive in the device in a tank treading configuration, which means that they are stretched in the flow direction and slightly tilted with respect to the flow direction. This means that compared to an ideal case where the RBC is studied initially at rest and perfectly oriented in the strain plane, in the experiments, the RBC is initially deformed and has an unknown orientation with respect to the flow. It will thus be necessary to quantify the effects of these elements on the RBC response.

4.3.5 Experimental case's preliminary results using tank treading initial shape and outcomes

As for the ideal case, results are presented using non-dimensional framework. Values of capillary number and internal Boussinesq number are the same that the values used for the ideal cases. Results are shown in Fig. 4.15. First, some similarities are observed between the ideal case results and the results obtained

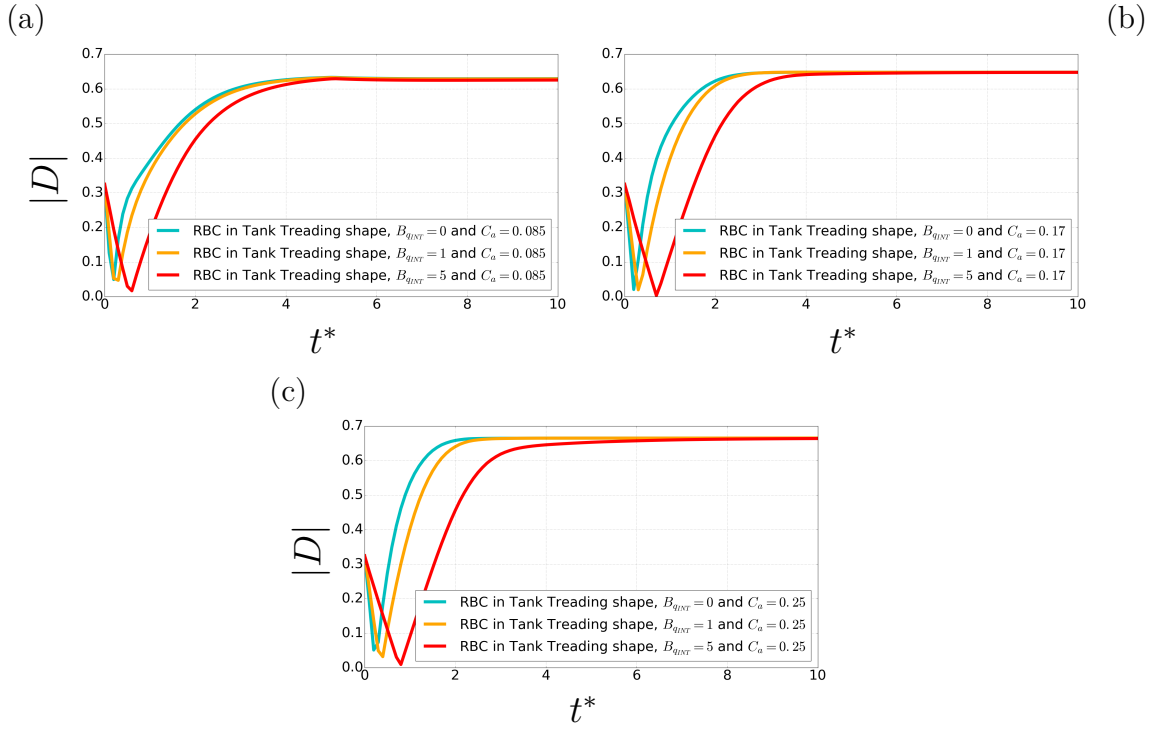

Figure 4.15: Absolute value of the deformation index as a function of the dimensionless time for three different Ca values obtained by simulating the experimental case configurations. (a) Ca=0.084, (b) Ca=0.17 and (c) Ca=0.25.

in this configuration. Indeed, the viscosity impacts the deformation index in a similar way than in the ideal case. Cases at $Bq_{int} = 1.0$ are similar to the inviscid cases, while a much larger delay is obtained at $Bq_{int} = 5.0$. For all cases, the final level of deformation corresponds to a side view of the RBC.

Finally, as before, the membrane viscosity greatly impacts the dynamics. One way to visualize this impact is to plot the dimensionless characteristic time t_c^* corresponding to the increased time it takes RBC to reach a stable configuration (at $\pm 5\%$) as a function of the capillary number Ca Fig. 4.16.

We can emphasize the non-linear character of the impact of the membrane viscosity as a function of the capillary number. As well as the nonlinearity of the impact of membrane viscosity on the characteristic time as the viscosity increases. To ensure the validity of the D values observed numerically with the reality of the experiment, we compared numerical values with the first values obtained experimentally on different RBC's samples. Experimental results are shown Fig. 4.17. These results were obtained thanks to the measurements carried

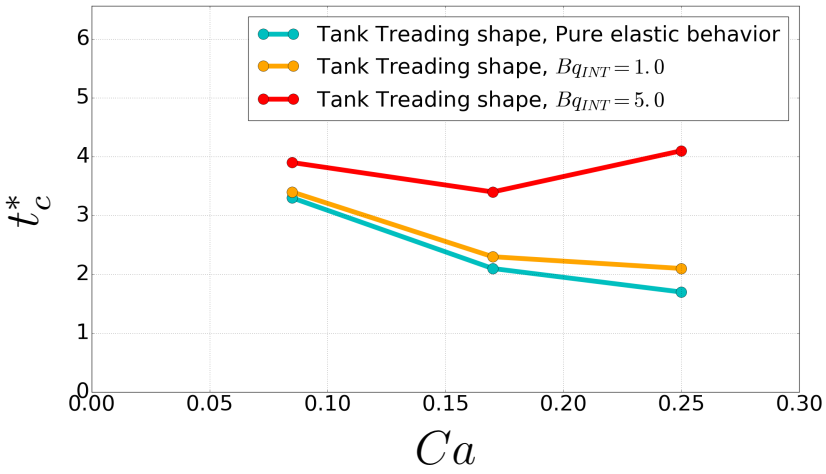

Figure 4.16: Nondimensional characteristic time t_c^* for RBCs , with different membrane viscosity values, in tank treading shape to reach its final stable shape (at ±5%), as a function of the capillary number Ca.

out by Ramadier, G. and Abkarian M. and we thank them for their collaboration in this work.

Because the study is really at its beginning, it is difficult to have a robust

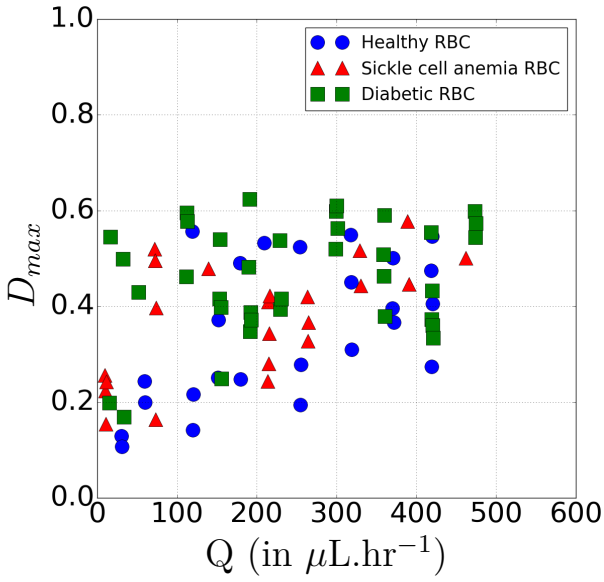

Figure 4.17: Maximum deformation index D_{max} observed experimentally for different flow rates Q for three different samples of RBCs, healthy and sick. The Ca range of values represented here is from values near 0.045 to 3.4. Experiment done at the CBS laboratory by Ramadier and Abkarian.

interpretation and to compare in detail those results. But we can observe that D values obtained numerically are in accordance with the range measured experimentally. However, we notice that our simulations all result with a D close to 0.6, which is not found experimentally. This suggests that the RBCs have turned. Experimentally, we seem to have two regimes. A regime with reorientation and another where the RBCs remain in the plane and deform without buckling. In the range of Ca values computed numerically, only the diabetic RBCs seem to reach D values observed experimentally.

Finally, when comparing the numerical results obtained here with results obtained in the ideal case, we observe that, unlike in the ideal case, here no buckling phenomenon is observed. It is certainly since are present on the initial RBC shape. However, as mentioned before, the initial angle of the cell with respect to the flow induces a rotation of the cell. This rotation is not clearly apparent on the deformation curves but can be seen by looking directly at the RBC during the simulation, as shown Fig. 4.19. It is important to note that this effect can be difficult to observe only experimentally and that it becomes reachable only by using numerical simulation combined with experimental work. The impact of the membrane viscosity on this rotation phenomenon still needs to be quantified.

To conclude, this study highlights the fact that the behavior of the RBC inside such a device is more complex than a simple stretching experiment. Indeed, the rotation effect due to the shape of the RBC inside the entering canal for example highlights the fact that the deformation index is not, in this case, only linked to the RBC deformation, but linked to its apparent deformation (see Fig. 4.18). This apparent deformation can contain solid movement such as the rotation observed in Fig. 4.19. However, this study also highlights the fact that thanks to numerical simulation and a membrane RBC model, all those complexities can be studied which leads this experiment to become richer. Also, thanks to the viscoelastic model in the membrane, the major impact of this behavior on the RBC deformability in this experiment has been highlighted. This study is a good example of the great synergy between experiments and numerical simulation. However, because this study is just at its beginning and cannot be finished during this thesis, more conclusions on the viscoelastic behavior of the RBC's membrane cannot be made.

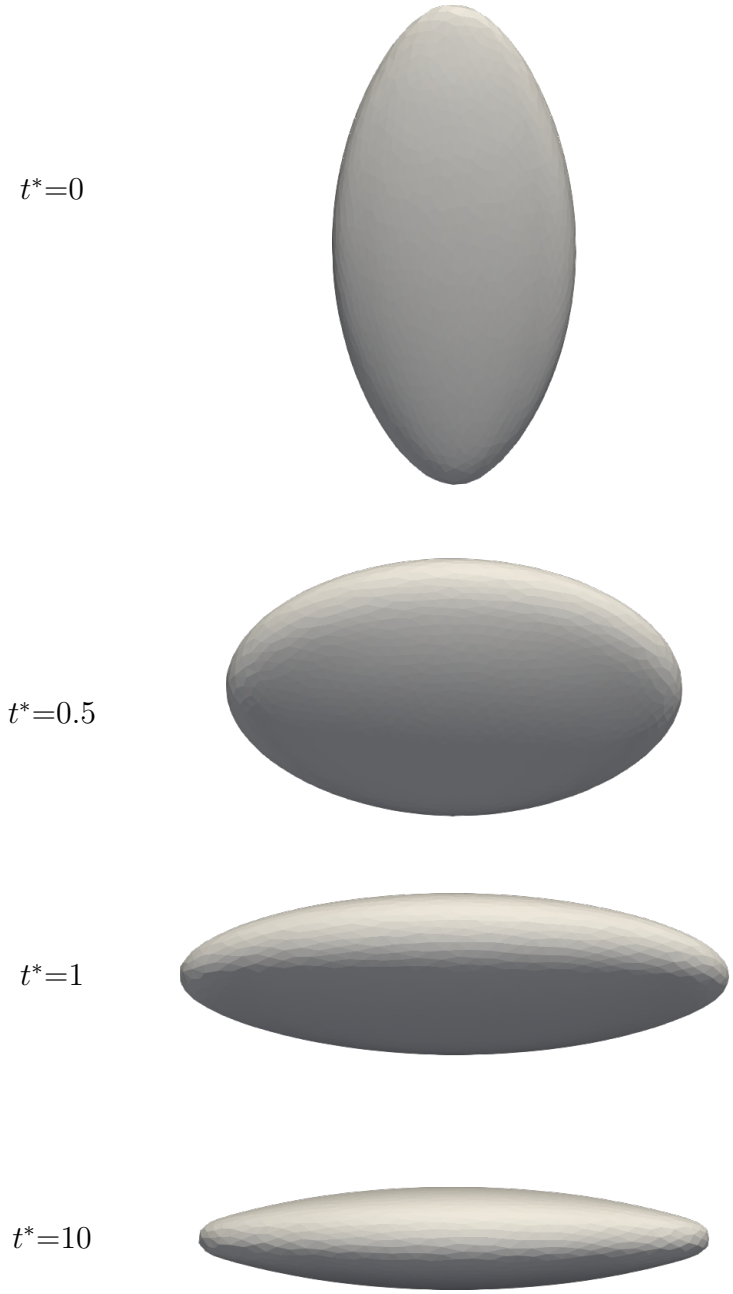

Figure 4.18: Visualization of the RBC shape at different t^* for initial tank treading shape, at $Ca = 0.25$. Visualization oriented along the z axis, and therefore following the experimentally observable plane.

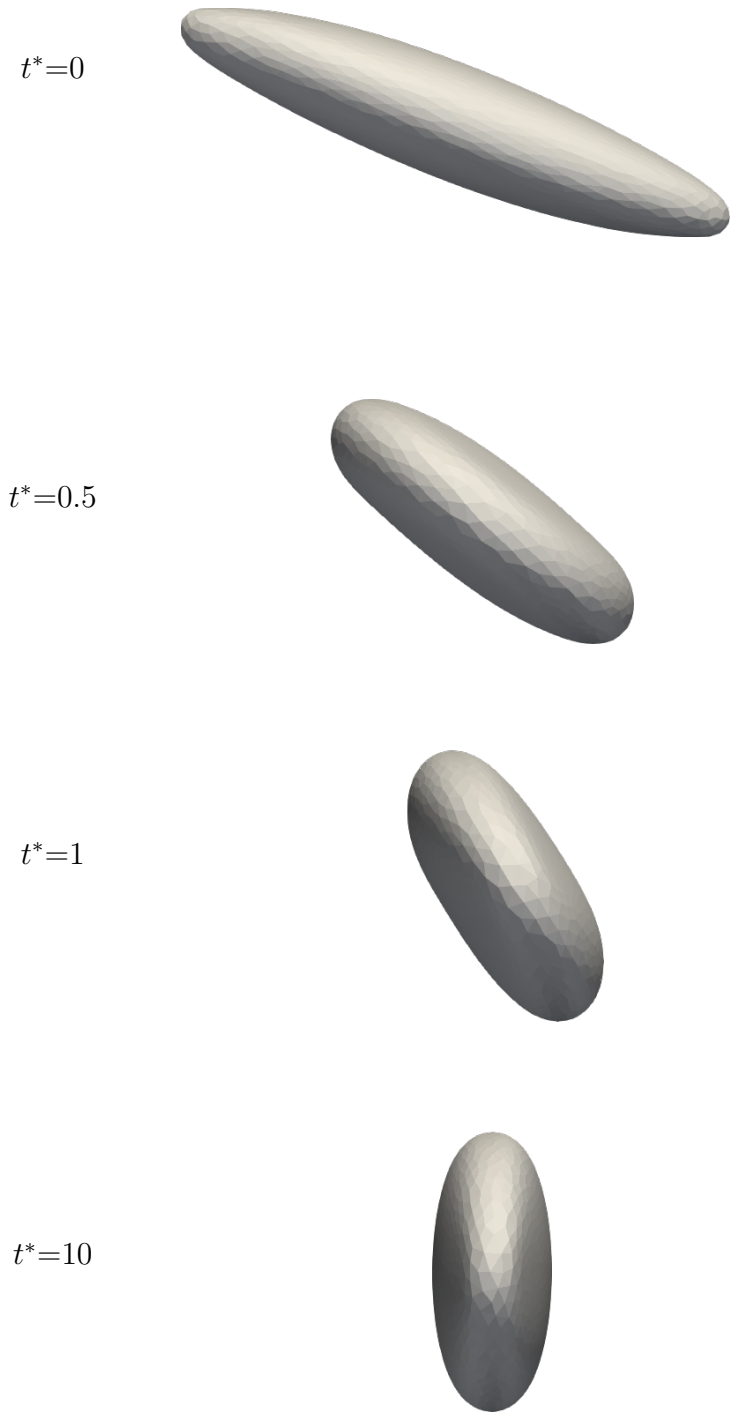

Figure 4.19: Visualization of the RBC shape at different t^* for initial tank treading shape, at $Ca = 0.25$. Visualization oriented along the extension axis (x axis), not reachable experimentally, to show the rotation of the RBC.

Chapter 5

Conclusion and perspectives

Chapter contents

5.1 Main Results 107
5.2 Perspectives 109
5.2.1 Study at the micro scale of the membrane 109
5.2.2 Study at the macro scale of the membrane 110

5.1 Main Results

This work presents the implementation and the study of one characteristic of the membrane of the RBC, usually not considered at the time when this work begins, namely the viscosity of the membrane, in an existing computer code, YALES2BIO. This study was therefore based on an existing state-of-the-art RBC model, and aimed to improve this model, while learning more about the behavior of the RBC membrane itself.

This work was therefore first focused on the search for a relevant membrane viscosity model. This research led to the theoretical model based on the work of Simo in 1984 [148]. The implementation of this model could be validated thanks to the simulations of capsule under shear presented in Section (3.5). This therefore resulted in having a state-of-the-art model of membrane viscoelasticity. This model was then used to study the impact of the intra-membrane dissipation

on different RBC dynamics. Two configurations have mainly been studied: the tank-treading configuration and the crossflow configuration, in which isolated RBCs are subjected to pure shear and pure strain, respectively. These two studies first shed light on the major impact of membrane viscosity on the different RBC dynamics.

The study of tank-treading RBCs was chosen because models of RBCs with inviscid membranes were shown to overestimate the tank-treading frequency, which led Dodson and Dimitrakopoulos [36] to hypothesize that membrane viscosity would provide the additional dissipation needed to reach a good agreement between simulations and experiments. The present study confirmed this hypothesis. We were able to show by means of parametric studies that the effect of internal viscosity and the effect of membrane viscosity are not the same and leads to two distinct impacts on the RBC dynamics. Moreover, this study made it possible to show that the model developed in YALES2BIO allowed the exact modeling of the frequencies of tank treading measured experimentally if a shear-thinning behavior of the membrane, visible in Fig. 4.5 is assumed. This confirmed some estimates using simpler modeling reported in the literature [155].

The second study enabled the establishment of an experimental device allowing, among other things, the study of membrane viscosity on different blood samples. It also allowed the development of all the digital simulation protocols allowing the optimization of the exploitation of the experimental measurement and giving access to information inaccessible without the simulation.
The purpose of this study and to proceed with a similar approach as for the study of tank-treading behavior but within the framework of RBC under strain. The question to which we aspire to answer thanks to this study is: can we make an estimate of the viscosity of the membrane of a RBC by studying its strain deformation? Moreover, if this is the case, do we observe the same type of behavior of the membrane viscosity as in the case of the study of the tank-treading behavior? This will allow us to say whether the shear-thinning membrane model is robust to different RBC dynamics or whether it is a phenomenon specific to the tank-treading behavior. This study also resulted in the manufacture of a dedicated chip to observe dynamics to study membrane viscosity. Experimental conditions were determined thanks to the numerical simulation of the flow device and the dynamics of a RBC with a viscous membrane, to highlight the impact of the membrane viscosity.

This study was also able to show that the configuration of an RBC during a strain is a more complex configuration than it looks. Indeed, the results strongly depend on the orientation of the RBCs as well as the reorientation due to the flow in our device. Buckling phenomena are observed and complicate the analysis. The origin of this phenomenon, whether numerical or not, remains to be determined. This work, therefore, makes it possible to support the importance of considering the viscoelastic behavior of the membrane in the reproduction of certain dynamics. Currently, multiple studies on the subject are beginning to emerge in the [68] literature. Nevertheless, we hope that this work will encourage to continue these studies to deepen the understanding of this behavior of the RBC membrane. In the next part, we detail various avenues for improving this study, which will allow us to deepen our knowledge of RBC membrane mechanics.

5.2 Perspectives

The perspectives of this work are split into two topics: the first one is the understanding of the internal mechanisms of the membrane resulting in this membrane viscosity.
The second part is a direct continuation of the applications studied in this work.

5.2.1 Study at the micro scale of the membrane

Consolidate the mechanical framework

One of the challenges in the viscoelasticity of RBC membrane is to combine a model for the stresses induced by membrane viscosity to an existing hyperelastic model for large deformations of the membrane, represented by the Skalak law [149]. To do so, an approach detailed in [76] refers to Simo's work [148]. From this model, in which assumptions of additivity of the viscous and elastic potential is made, the equations implemented in the solver are derived. However, the link between Simo's work and the starting equation in [76] are unclear. Indeed, Simo presents a very different framework, and a specific work is needed to justify its use. Due to a lack of time in this thesis, we could not perform this work, but we think it would be important to have a better idea of the underlying assumptions of the model.

Moreover, the validation of the implementation of this law of behavior consists in using the deformations capsule in shear flow, detailed Section (3.5). This case has now been used on several studies and serves to validate the implementation of viscosity [68, 90, 102]. Nevertheless, the validation is based on the comparison of a global deformation index of the simulated capsules. However, the observed dynamics are much more complex, with the appearance of membrane folds for example.
Thus, if this case should be used as a validation protocol for future studies, a more detailed study of this case, with indices more representative of the simulated dynamics should be proposed. In addition, comparisons with experimental results would be interesting.

Identification of sources of dissipation

Although the presence of internal membrane dissipation leading to membrane viscosity is no longer a matter of debate in the community, the sources of this dissipation have not yet been clearly identified. Thus, phenomena such as the circulation of the lipid bilayer around transmembrane proteins would be a possible suspect in the phenomena generating dissipation. Experimental devices like AFM allow inspection and observation of the membrane at a more local scale than what is typically observed [18, 33, 152].
More local simulation tools such as multi-scale models could undoubtedly be useful to inspect these phenomena [50, 122].

5.2.2 Study at the macro scale of the membrane

Improve the viscosity model

As shown in Section (4.2), the addition of a viscosity model coupled with the known dynamics study of the RBC, in this case the tank treading, leads to a better understanding of the dynamics as well as the nature of the RBC. Thus, it is by studying tank treading that we have come to an apparent shear-thinning membrane viscosity, with membrane viscosity values ranging from 3.5×10^{-4} cP.m to less than 0.5×10^{-4} cP.m.
It would be interesting to compare this model of red blood cells with this range of values to other dynamics, with the objective to verify the robustness of this

finding in other dynamics. It was the objective of the study of RBC in crossflow Section (4.3). But there are a very large number of observed dynamics of the RBC. The idea being that the more the model makes accessible a large number of configurations, the more it can be trusted to inspect new horizons of research.

Searching other dynamics

The previous part insists on the fact that the model can benefit from improvement by studying the configurations which were already accessible beforehand. Similarly, improving a model allows access to new configurations. Taking into account or not taking into account the dissipation of the membrane must have an impact on all the high-speed configurations. Such dynamics have direct applications, such as the study of the behavior of RBCs within hydrofocused counting tanks.
Similarly, membrane viscosity should have its part to play in determining larger scale viscosity, such as blood viscosity. Thus, if we want to be able to go up the scales, the membrane viscosity must certainly be considered. In addition, network effects observed in work on blood flow inside bifurcations with the transient dynamics of RBCs that stop in the flow and leave again must certainly be impacted by the membrane viscosity [8]. It would be interesting to study the role of the membrane viscosity in this type of phenomenon.

Chapter 6

Appendix

Chapter contents

6.1 Appendix 1: Discretization of operators 114
6.1.1 Laplacian operators 114
6.1.2 Divergence operators 115
6.1.3 Gradient operator 116

6.1 Appendix 1: Discretization of operators

6.1.1 Laplacian operators

This part is dedicated to the calculation of Laplacian operators, namely $\mathcal{L}(P)$, $\mathcal{L}_{cv}(\nu, \boldsymbol{u})$ and $\mathcal{L}_{cv}(\nu, \boldsymbol{u})$, thanks to spatial discretization.
First, let us use the formalism presented previously. Let's define $\boldsymbol{x}_{i,j}$ the position vector defining the point of intersection between the vector linking the points $\boldsymbol{x}_i$ and $\boldsymbol{x}_j$ and the interface $S_{i,j}$. Similar to Eq. (3.21), using the assumption that $\boldsymbol{x}_{i,j}$ is the center of mass of $S_{i,j}$ we can apply the equation Eq. (3.14) at the position $\boldsymbol{x}_{i,j}$ to obtain the following equation at the order 2:

$$\mathcal{L}(P)|_i = \sum_j \int_{S_{i,j}} \boldsymbol{\nabla} P . d\boldsymbol{S} = \sum_j \nabla P|_{i,j} . \boldsymbol{S}_{i,j} \tag{6.1}$$

with $\boldsymbol{S}_{i,j}$ the normal vector of $S_{i,j}$ having as norm the surface of $S_{i,j}$.
Une approximation de $\nabla P|_{i,j}$ est possible en exprimant les développement de Taylor au points i et j de la quantité P:

$$P_i = P_{i,j} + \boldsymbol{\nabla} P|_{i,j} . (\boldsymbol{x}_i - \boldsymbol{x}_{i,j}) + \mathcal{O}\left(||\boldsymbol{x}_i - \boldsymbol{x}_{i,j}||^2\right) \tag{6.2}$$

$$P_j = P_{i,j} + \boldsymbol{\nabla} P|_{i,j} . (\boldsymbol{x}_j - \boldsymbol{x}_{i,j}) + \mathcal{O}\left(||\boldsymbol{x}_j - \boldsymbol{x}_{i,j}||^2\right). \tag{6.3}$$

We can thus, by subtracting Eq. (6.2) from Eq. (6.3), obtain an expression of $\boldsymbol{\nabla} P|_{i,j}$:

$$\begin{aligned} P_j - P_i &= \boldsymbol{\nabla} P|_{i,j} . (\boldsymbol{x}_j - \boldsymbol{x}_i) \\ \leftrightarrow \boldsymbol{\nabla} P|_{i,j} &= (P_j - P_i) \frac{(\boldsymbol{x}_j - \boldsymbol{x}_i)}{|\boldsymbol{x}_j - \boldsymbol{x}_i|^2}. \end{aligned} \tag{6.4}$$

Now, we identify Eq. (6.4) in Eq. (6.1). We obtain:

$$\mathcal{L}(P)|_i = \sum_j (P_j - P_i) \frac{(\boldsymbol{x}_j - \boldsymbol{x}_i)}{|\boldsymbol{x}_j - \boldsymbol{x}_i|^2} . \boldsymbol{S}_{i,j}. \tag{6.5}$$

Proceeding similarly, one can also rewrite $\mathcal{L}_{cv}(\nu, \boldsymbol{u})$ as follows:

$$\mathcal{L}_{cv}(\nu, \boldsymbol{u})|_i = \sum_j \nu (\boldsymbol{u}_j - \boldsymbol{u}_i) \left(\frac{(\boldsymbol{x}_j - \boldsymbol{x}_i)}{|\boldsymbol{x}_j - \boldsymbol{x}_i|^2} . \boldsymbol{S}_{i,j} \right). \tag{6.6}$$

Similarly, we get an expression of $\mathcal{L}^T_{cv}(\nu, \boldsymbol{u})$:

$$\mathcal{L}^T_{cv}(\nu, \boldsymbol{u})|_i = \sum_j \nu \frac{(\boldsymbol{x}_j - \boldsymbol{x}_i)}{|\boldsymbol{x}_j - \boldsymbol{x}_i|^2} \left((\boldsymbol{u}_j - \boldsymbol{u}_i) . \boldsymbol{S}_{i,j} \right). \tag{6.7}$$

It is important to note that this development was done assuming ν constant in the domain. This is not necessarily the case, especially in studies within the framework of the study of red blood cells. In this case, it suffices during development to replace in the relations Eq. (6.6) and Eq. (6.7) ν by $\nu_{i,j}$. Thus, using the Taylors expansion at point i and j of the quantities ν_i and ν_j, we obtain the following expression, with a convergence order of 2:

$$\nu_{i,j} = \frac{\nu_i + \nu_j}{2}. \tag{6.8}$$

6.1.2 Divergence operators

This part aims to detail the spatial discretization of the operators $\mathcal{C}(\boldsymbol{u}, \boldsymbol{u})$ and $\mathcal{D}(\boldsymbol{u})$. Many points already mentioned during the development of the Laplacian operators will be reused here. Using the same assumption as previously for Eq. (6.1), namely that the point represented by the position vector $\boldsymbol{x}_{i,j}$ is located at the center of mass of the surface $S_{i,j}$, we can rewrite $\mathcal{C}(\boldsymbol{u}, \boldsymbol{u})$ calculated at point i such that:

$$\mathcal{C}|_i(\boldsymbol{u}, \boldsymbol{u}) = \sum_j \int_{S_{i,j}} (\boldsymbol{u} \otimes \boldsymbol{u})\, d\boldsymbol{S} = \sum_j (\boldsymbol{u}_{i,j} \otimes \boldsymbol{u}_{i,j})\, \boldsymbol{S}_{i,j}. \tag{6.9}$$

We can obtain an expression for $\boldsymbol{u}_{i,j}$ using the Taylor expansion at point i and j, as we did previously for $\nu_{i,j}$ Eq. (6.8). We therefore obtain the following expression:

$$\boldsymbol{u}_{i,j} = \frac{\boldsymbol{u}_i + \boldsymbol{u}_j}{2}. \tag{6.10}$$

By identifying $\boldsymbol{u}_{i,j}$ by Eq. (6.10) in Eq. (6.9), we obtain:

$$\mathcal{C}|_i(\boldsymbol{u}, \boldsymbol{u}) = \sum_j \left(\frac{\boldsymbol{u}_j + \boldsymbol{u}_i}{2} \otimes \frac{\boldsymbol{u}_j + \boldsymbol{u}_i}{2} \right) \boldsymbol{S}_{i,j}. \tag{6.11}$$

This expression can be rewritten using the property $(\boldsymbol{a} \otimes \boldsymbol{b}).\boldsymbol{c} = \boldsymbol{a}(\boldsymbol{b}.\boldsymbol{c})$:

$$\mathcal{C}|_i(\boldsymbol{u}, \boldsymbol{u}) = \sum_j \frac{\boldsymbol{u}_j + \boldsymbol{u}_i}{2} \left(\frac{\boldsymbol{u}_j + \boldsymbol{u}_i}{2} . \boldsymbol{S}_{i,j} \right) = \sum_j \frac{\boldsymbol{u}_j + \boldsymbol{u}_i}{2} U_{i,j}. \tag{6.12}$$

The term $U_{i,j}$ is identified as $\frac{\boldsymbol{u}_j + \boldsymbol{u}_i}{2} . \boldsymbol{S}_{i,j}$ and represents the flow passing through the surface $S_{i,j}$.

Finally, we can make the same reasoning for $\mathcal{D}(\boldsymbol{u})|_i$, using Eq. (6.8) as well as the fact that $\boldsymbol{x}_{i,j}$ is the center of mass of $S_{i,j}$, we get:

$$\mathcal{D}|_i(\boldsymbol{u}) = \sum_j \frac{\boldsymbol{u}_j + \boldsymbol{u}_i}{2} . \boldsymbol{S}_{i,j} = \sum_j U_{i,j}. \tag{6.13}$$

We can therefore see that $\mathcal{D}(\boldsymbol{u})$ represents the set of incoming and outgoing flows of the volume Ω_i, passing through the set of surfaces $S_{i,j}$.

6.1.3 Gradient operator

Here, we are going to write the spatial discretization to order 2 of the operator $\mathcal{G}(P)$. We will calculate the quantity $P_{i,j}$ as we did previously to calculate the quantities $\nu_{i,j}$ Eq. (6.8) and $\boldsymbol{u}_{i,j}$. We therefore have the following second-order expression:

$$P_{i,j} = \frac{P_i + P_j}{2}. \tag{6.14}$$

Thus, by identifying $P_{i,j}$ within the equation Eq. (3.12), as well as by using the fact that $\boldsymbol{x}_{i,j}$ is center of mass of $S_{i,j}$, we obtain the following expression of $\mathcal{G}(P)|_i$:

$$\mathcal{G}(P)|_i = \sum_j \frac{P_j + P_i}{2} \boldsymbol{S}_{i,j}. \tag{6.15}$$

Bibliography

[1] M. Abkarian, M. Faivre, and A. Viallat. Swinging of red blood cells under shear flow. *Physical Review Letters*, 98(188302), 2007.

[2] M. Abkarian and A. Viallat. Vesicles and red blood cells in shear flow. *Soft Matter*, 4:653–657, 2008.

[3] M. Abkarian and A. Viallat. *Fluid-Structure Interactions in Low-Reynolds-Number Flows*, chapter On the importance of red blood cells deformability in blood flow, pages 347–462. Royal Society of Chemistry, 2016.

[4] R. Agrawal, T. Smart, J. Nobre-Cardoso, C. Richards, R. Bhatnagar, A. Tufail, D. Shima, P. H. Jones, and C. Pavesio. Assessment of red blood cell deformability in type 2 diabetes mellitus and diabetic retinopathy by dual optical tweezers stretching technique. *Scientific Reports*, 6, 2016.

[5] R. Aubry, F. Mut, R. Löhner, and J. R. Cebral. Deflated preconditioned conjugate gradient solvers for the pressure–Poisson equation. *Journal of Computational Physics*, 227:10196–10208, 2008.

[6] P. Bagchi and A. Z. K. Yazdani. Analysis of membrane tank-tread of nonspherical capsules and red blood cells. *European Physical Journal E*, 35(12103), 2012.

[7] S. K. Ballas and N. Mohandas. Sickle red cell microrheology and sickle blood rheology. *Microcirculation*, 11:209–225, 2004.

[8] P. Balogh and P. Bagchi. Direct numerical simulation of cellular-scale blood flow in 3d microvascular networks. *Biophysical Journal*, 113:2815–2826, 2017.

[9] D. Barthès-Biesel. Capsule motion in flow: Deformation and membrane buckling. *Comptes Rendus Physique*, 10(8):764–774, 2009.

[10] D. Barthès-Biesel and H. Sgaier. Role of membrane viscosity in the orientation and deformation of a spherical capsule suspended in shear flow. *Journal of Fluid Mechanics*, 160:119–135, 1985.

[11] O. K. Baskurt, M. R. Hardeman, M. Uyuklu, P. Ulker, M. Cengiz, N. Nemeth, S. Sehyun, T. Alexy, and H. J. Meiselman. Comparison of three commercially available ektacytometers with different shearing geometries. *Biorheology*, 46:251–264, 2009.

[12] M. Bessis, N. Mohandas, and C. Feo. *Automation in Hematology*, chapter Automated Ektacytometry: A New Method of Measuring Red Cell Deformability and Red Cell Indices, pages 153–165. Springer Berlin Heidelberg, 1981.

[13] M. Bessis, R. I. Weed, and P. F. Leblond, editors. *RED CELL SHAPE. Physiology, Pathology, Ultrastructure*. Springer Verlag.

[14] M. Bitbol. Red blood cell orientation in orbit C=0. *Biophysical Journal*, 49:1055–1068, 1986.

[15] A. Bogdanova, L. Kaestner, G. Simionato, A. Wickrema, and A. Makhro. Heterogeneity of red blood cells: Causes and consequences. *Frontiers in Physiology*, 11(392):1–11, 2020.

[16] M. Bor-Kucukatay, R. B. Wenby, H. J. Meiselman, and O. K. Baskurt. Effects of nitric oxide on red blood cell deformability. *American Institute of Aeronautics and Astronautics Journal*, 284(5), 2003.

[17] F. H. Bosch, J. M. Werre, L. Schipper, B. Roerdinkholder-Stoelwinder, T. Huls, F. Willekens, G. Wichers, and M. R. Halie. Determinants of red blood cell deformability in relation to cell age. *European Jounal of Haematology*, 1994.

[18] K. E. Bremmell, A. Evans, and C. A. Prestidge. Deformation and nanorheology of red blood cells: An afm investigation. *Colloids and Surfaces B: Biointerfaces*, 50(1):43–48, 2006.

[19] A. Briole, T. Podgorski, and B. Abou. Molecular rotors as intracellular probes of red blood cell stiffness. *Soft Matter*, 17:4525–4537, 2021.

[20] P. B. Canham. The minimum energy of bending as a possible explanation of the biconcave shape of the human red blood cell. *Journal of Theoretical Biology*, 26:61–81, 1970.

[21] J.-M. Charrier, S. Shrivastava, and R. Wu. Free and constrained inflation of elastic membranes in relation to thermoforming non-axisymmetric problems. *The Journal of Strain Analysis for Engineering Design*, 24(2):55–74, 1989.

[22] S. Chien. Shear dependence of effective cell volume as a determinant of blood viscosity. *Science*, 168:977–979, 1970.

[23] S. Chien. Red cell deformability and its relevance to blood flow. *Annual Review of Physiology*, 49:177–192, 1987.

[24] S. Chien, K.-L. P. Sung, R. Skalak, S. Usami, and Tözeren. Red cell extensional recovery and the determination of membrane viscosity. *Biophysical Journal*, 24:463–487, 1978.

[25] S. Chien, S. Usami, and J. F. Bertles. Abnormal rheology of oxygenated blood in sickle cell anemia. *Journal of Clinical Investigation*, 49:623–634, 1970.

[26] A. Chorin. Numerical solution of the Navier–Stokes equations. *Mathematics of Computation*, 22:745–762, 1968.

[27] D. Cordasco and P. Bagchi. Orbital drift of capsules and red blood cells in shear flow. *Physics of Fluids*, 25(091902), 2013.

[28] D. Cordasco and P. Bagchi. Intermittency and synchronized motion of red blood cell dynamics in shear flow. *Journal of Fluid Mechanics*, 759:472–488, 2014.

[29] D. Cordasco and P. Bagchi. On the shape memory of red blood cells. *Physics of Fluids*, 29(041901), 2017.

[30] D. Cordasco, Yazdani, and P. Bagchi. Comparison of erythrocyte dynamics in shear flow under different stress-free configurations. *Physics of Fluids*, 26(041902), 2014.

[31] J. Czerwinska, S. M. Wolf, H. Mohammadi, and S. Jeney. Red blood cell aging during storage, studied using optical tweezers experiment. *Cellular and Molecular Bioengineering*, 8(2):258–266, 2015.

[32] L. Da Costa, J. Galimand, O. Fenneteau, and N. Mohandas. Hereditary spherocytosis, elliptocytosis, and other red cell membrane disorders. *Blood reviews*, 27(4):167–178, 2013.

[33] B. Daily, E. Elson, and G. Zahalak. Cell poking. determination of the elastic area compressibility modulus of the erythrocyte membrane. *Biophysical Journal*, 45(4):671–682, 1984.

[34] M. Dao, C. T. Lim, and S. Suresh. Mechanics of the human red blood cell deformed by optical tweezers. *Journal of the Mechanics and Physics of Solids*, 51:2259–2280, 2003.

[35] P. Dimitrakopoulos. Analysis of the variation in the determination of the shear modulus of the erythrocyte membrane: Effects of the constitutive law and membrane modeling. *Physical Review E*, 85(041917), 2012.

[36] W. R. Dodson III and P. Dimitrakopoulos. Tank-treading of erythrocytes in strong shear flows via a nonstiff cytoskeleton-based continuum computational modeling. *Biophysical Journal*, 99:2906–2916, 2010.

[37] W. R. Dodson III and P. Dimitrakopoulos. Oscillatory tank-treading motion of erythrocytes in shear flows. *Physical Review E*, 84(011913), 2011.

[38] W. R. Dodson III and P. Dimitrakopoulos. Tank-treading of swollen erythrocytes in shear flows. *Physical Review E*, 85(021922), 2012.

[39] J. Dupire, M. Abkarian, and A. Viallat. A simple model to understand the effect of membrane shear elasticity and stress-free shape on the motion of red blood cells in shear flow. *Soft Matter*, 11:8372–8382, 2015.

[40] J. Dupire, M. Socol, and A. Viallat. Full dynamics of a red blood cell in shear flow. *Proceedings of the National Academy of Sciences USA*, 109(51):20808–20813, 2012.

[41] M. L. Ellsworth, C. G. Ellis, D. Goldman, A. H. Stephenson, H. H. Dietrich, and R. S. Sprague. Erythrocytes: Oxygen sensors and modulators of vascular tone. *Physiology*, 24(2):107–116, 2009.

[42] R. Enjalbert, D. Hardman, T. Krüger, and M. O. Bernabeu. Compressed vessels bias red blood cell partitioning at bifurcations in a hematocrit-dependent manner: Implications in tumor blood flow. *Proceedings of the National Academy of Sciences USA*, 118(25), 2021.

[43] E. Evans, N. Mohandas, and A. Leung. Static and dynamic rigidities of normal and sickle erythrocytes. major influence of cell hemoglobin concentration. *Journal of Clinical Investigation*, 73:477–488, 1984.

[44] E. A. Evans. Bending elastic modulus of red blood cell membrane derived from buckling instability in micropipet aspiration tests. *Biophysical Journal*, 43:27–30, 1983.

[45] E. A. Evans and Y. C. Fung. Improved measurements of the erythrocyte geometry. *Microvascular Research*, 4:335–347, 1972.

[46] E. A. Evans and R. M. Hochmuth. Membrane viscoelasticity. *Biophysical Journal*, 16(1):1–11, 1976.

[47] M. M. Faghih and M. K. Sharp. Deformation of human red blood cells in extensional flow through a hyperbolic contraction. *Biomechanics and Modeling in Mechanobiology*, 19, 2019.

[48] A. Farutin, T. Biben, and C. Misbah. 3D numerical simulations of vesicle and inextensible capsule dynamics. *Journal of Computational Physics*, 275:539–568, 2014.

[49] D. A. Fedosov, B. Caswell, and G. Karniadakis. Systematic coarse-graining of spectrin-level red blood cell models. *Computer Methods in Applied Mechanics and Engineering*, 199:1937–1948, 2010.

[50] D. A. Fedosov, B. Caswell, and G. E. Karniadakis. A multiscale red blood cell model with accurate mechanics, rheology, and dynamics. *Biophysical Journal*, 98:2215–2225, 2010.

[51] D. A. Fedosov, B. Caswell, A. S. Popel, and G. E. Karniadakis. Blood flow and cell-free layer in microvessels. *Microcirculation*, 17:615–628, 2010.

[52] D. A. Fedosov and G. Gompper. White blood cell margination in microcirculation. *Soft Matter*, 10:2961–2970, 2014.

[53] D. A. Fedosov, W. Pan, B. Caswell, G. Gompper, and G. E. Karniadakis. Predicting human blood viscosity in silico. *Proceedings of the National Academy of Sciences USA*, 108(29):11772–11777, 2011.

[54] T. M. Fischer. On the energy dissipation in a tank-treading human red blood cell. *Biophysical Journal*, 32:863–868, 1980.

[55] T. M. Fischer. Shape memory of human red blood cells. *Biophysical Journal*, 86:3304–3313, 2004.

[56] T. M. Fischer. Tank-tread frequency of the red cell membrane: Dependence on the viscosity of the suspending medium. *Biophysical Journal*, 93:2553–2561, 2007.

[57] T. M. Fischer, C. W. M. Haest, M. Stöhr-Liesen, H. Schmid-Schönbein, and R. Skalak. The stress-free shape of the red blood cell membrane. *Biophysical Journal*, 34:409–422, 1981.

[58] T. M. Fischer and R. Korzeniewski. Threshold shear stress for the transition between tumbling and tank-treading of red blood cells in shear flow: dependence on the viscosity of the suspending medium. *Journal of Fluid Mechanics*, 736:351–365, 2013.

[59] T. M. Fischer, M. Stöhr-Liesen, and H. Schmid-Schönbein. The red cell as a fluid droplet: Tank tread-like motion of the human erythrocyte membrane in shear flow. *Science*, 202:894–896, 1978.

[60] A. M. Forsyth, J. Wan, P. D. Owrutsky, M. Abkarian, and S. H. A. Multiscale approach to link red blood cell dynamics, shear viscosity, and ATP release. *Proceedings of the National Academy of Sciences USA*, 108(27):10986–10991, 2011.

[61] J. B. Freund. The flow of red blood cells through a narrow spleen-like slit. *Physics of Fluids*, 25(110807), 2013.

[62] J. B. Freund. Numerical simulation of flowing blood cells. *Annual Review of Fluid Mechanics*, 46:67–95, 2014.

[63] F. J. Galindo-Rosales, M. S. J. Oliveira, and M. A. Alves. Optimized cross-slot microdevices for homogeneous extension. *Royal Society of Chemistry Advances*, 4:7799–7804, 2014.

[64] P. Gambhire, S. Atwell, C. Iss, F. Bedu, I. Ozerov, C. Badens, E. Helfer, A. Viallat, and A. Charrier. High aspect ratio sub-micrometer channels using wet etching: Application to the dynamics of red blood cell transiting through biomimetic splenic slits. *Small*, 13, 2017.

[65] H. L. Goldsmith and J. Marlow. Flow behaviour of erythrocytes. I. rotation and deformation in dilute suspensions. *Proceedings of the Royal Society of London. Series B*, 182:351–384, 1972.

[66] J. Gounley and Y. Peng. Computational modeling of membrane viscosity of red blood cells. *Communications in Computational Physics*, 17(4):1073–1087, 2015.

[67] X. Grandchamp, G. Coupier, A. Srivastav, C. Minetti, and T. Podgorski. Lift and down-gradient shear-induced diffusion in red blood cell suspensions. *Physical Review Letters*, 110(108101), 2013.

[68] F. Guglietta, M. Behr, L. Biferale, G. Falcucci, and M. Sbragaglia. On the effect of membrane viscositity on transient red blood cell dynamics. *Soft Matter*, 16:6191–6205, 2020.

[69] F. Guglietta, M. Behr, G. Falcucci, and M. Sbragaglia. Loading and relaxation dynamics of a red blood cell. *Soft Matter*, 17, 2021.

[70] S. Guido and G. Tomaiuolo. Microconfined flow behavior of red blood cells in vitro. *Comptes Rendus Physique*, 10:751–763, 2009.

[71] M. R. Hardeman, P. T. Goedhart, and N. H. Schut. Laser-assisted optical rotational cell analyser (l.o.r.c.a.); ii. red blood cell deformability: elongation index versus cell transit time. *Clinical Hemorheology*, 1994.

[72] S. J. Haward. Microfluidic extensional rheometry using stagnation point flow. *Biomicrofluidics*, 043401(10), 2016.

[73] V. Heinrich, K. Ritchie, N. Mohandas, and E. Evans. Elastic thickness compressibilty of the red cell membrane. *Biophysical Journal*, 81(3):1452–1463, 2001.

[74] W. Helfrich. Elastic properties of lipid bilayers: Theory and possible experiments. *Z. Naturforsch*, 28 c:693–703, 1973.

[75] S. Hénon. A new determination of the shear modulus of the human erythrocyte membrane using optical tweezers. *Biophysical Journal*, 76:1145–1151, 1999.

[76] I. Hibbitt, Karlsson & Sorensen. *ABAQUS/Standard Theory Manual*, 2002.

[77] J. M. Higgins. Red blood cell population dynamics. *Clinics in Laboratory Medicine*, 35:43–57, 2015.

[78] R. M. Hochmuth and R. E. Waugh. Erythrocyte membrane elasticity and viscosity. *Annual Review of Physiology*, 49:209–219, 1987.

[79] R. M. Hochmuth, P. R. Worthy, and E. A. Evans. Red cell extensional recovery and the determination of membrane viscosity. *Biophysical Journal*, 26:101–114, 1979.

[80] A. R. Honerkamp-Smith, F. G. Woodhouse, V. Kantsler, and R. E. Goldstein. Membrane viscosity determined from shear-driven flow in giant vesicles. *Physical Review Letters*, 111, 2013.

[81] C. Iss, D. Midou, A. Moreau, D. Held, A. Charrier, S. Mendez, A. Viallat, and E. Helfer. Self-organization of red blood cell suspensions under confined 2d flows. *Soft Matter*, 15:2971–2980, 2019.

[82] B. Kaoui, T. Krüger, and J. Harting. How does confinement affect the dynamics of viscous vesicles and red blood cells? *Soft Matter*, 8:9246–9252, 2012.

[83] C. Kelemen, S. Chien, and G. M. Artmann. Temperature transition of human hemoglobin at body temperature: Effects of calcium. *Biophysical Journal*, 80:2622–2630, 2001.

[84] S. R. Keller and R. Skalak. Motion of a tank-treading ellipsoidal particle in a shear flow. *Journal of Fluid Mechanics*, 120:27–47, 1982.

[85] J. Kim and P. Moin. Application of a fractional-step method to incompressible Navier-Stokes equations. *Journal of Computational Physics*, 59:308–323, 1985.

[86] Y. Kim, K. Kim, and Y. Park. *Blood Cell : Measurement Techniques for Red Blood Cell Deformability: Recent Advances*, chapter 10. IntechOpen, 2012.

[87] L. Lanotte, J. Mauer, S. Mendez, D. A. Fedosov, J.-M. Fromental, V. Claveria, F. Nicoud, G. Gompper, and M. Abkarian. Red cells' dynamic morphologies govern blood shear thinning under microcirculatory flow conditions.

Proceedings of the National Academy of Sciences USA, 113(47):13289–13294, 2016.

[88] G. Lenormand, S. Hénon, A. Richet, J. Siméon, and F. Gallet. Direct measurement of the area expansion and shear moduli of the human red blood cell membrane skeleton. *Biophysical Journal*, 81:43–56, 2001.

[89] J. Li, M. Dao, C. T. Lim, and S. Suresh. Spectrin-level modeling of the cytoskeleton and optical tweezers stretching of the erythrocyte. *Biophysical Journal*, 88:3707–3719, 2005.

[90] P. Li and J. Zhang. A finte difference method with subsampling for immersed boundary simulations of the capsule dynamics with viscoelastic membranes. *International Journal for Numerical Methods in Engineering*, 35(6), 2019.

[91] G. H. W. Lim, M. Wortiz, and R. Mukhopadhyay. *Red Blood Cell Shapes and Shape Transformations: Newtonian Mechanics of a Composite Membrane*, volume Lipid Bilayers and Red Blood Cells of *Soft Matter*, chapter 2, pages 94–269. WILEY-VCH Verlag GmbH & Co. KGaA, 2008.

[92] R. I. Litvinov and J. W. Weisel. Role of red blood cells in haemostasis and thrombosis. *ISBT Science Series*, 12(1):176?–183, 2017.

[93] W. K. Liu, Y. Chen, R. A. Uras, and C. T. Chang. Generalized multiple scale reproducing kernel particle methods. *Computer Methods in Applied Mechanics and Engineering*, 139:91–157, 1996.

[94] W. K. Liu, S. Jun, and Y. F. Zhang. Reproducing kernel particle methods. *International Journal for Numerical Methods in Fluids*, 20:1081–1106, 1995.

[95] X. Liu, Z.-y. Tang, Z. Zeng, X. Chen, W.-j. Yao, Z.-y. Yan, Y. Shi, H.-x. Shan, D.-g. Sun, D.-q. He, and Z.-y. Wen. The measurement of shear modulus and membrane surface viscosity of rbc membrane with ektacytometry: A new technique. *Mathematical Biosciences*, 209:190–204, 2007.

[96] Y. Liu and W. K. Liu. Rheology of red blood cell aggregation by computer simulation. *Journal of Computational Physics*, 220:139–154, 2006.

[97] Z. Liu, J. R. Clausen, R. R. Rao, and C. K. Aidun. Nanoparticle diffusion in sheared cellular blood flow. *Journal of Fluid Mechanics*, 871:636–667, 2019.

[98] J. Lyu, P. G. Chen, G. Boedec, M. Leonetti, and M. Jaeger. Hybrid continuum–coarse-grained modeling of erythrocytes. *Comptes Rendus Mécanique*, 346(6):439–448, 2018.

[99] M. Malandain, N. Maheu, and V. Moureau. Optimization of the deflated conjugate gradient algorithm for the solving of elliptic equations on massively parallel machines. *Journal of Computational Physics*, 238:32–47, 2013.

[100] J. E. Mancuso and W. D. Ristenpart. Stretching of red blood cells at high strain rates. *Physical Review Fluids*, 2017.

[101] J. J. Martinez-Vega and A. Riviere. Mesure de frottement interne. *Techniques de l'Ingénieur Analyses de surface et de matériaux*, base documentaire : TIB383DUO(ref. article : p1310), 2000.

[102] P. Matteoli, F. Nicoud, and S. Mendez. Impact of the membrane viscosity on the tank-treading behavior of red blood cells. *Physical Review Fluids*, 6, 2021.

[103] J. Mauer, S. Mendez, L. Lanotte, F. Nicoud, M. Abkarian, G. Gompper, and D. A. Fedosov. Flow-induced transitions of red blood cell shapes under shear. *Physical Review Letters*, 121(118103), 2018.

[104] S. Mendez and M. Abkarian. In-plane elasticity controls the full dynamics of red blood cells in shear flow. *Physical Review Fluids*, 3(101101(R)), 2018.

[105] S. Mendez and M. Abkarian. *Dynamics of Blood Cell Suspensions in Microflows*, chapter Single Red Blood Cell Dynamics in Shear Flow and their Role in Hemorheology. CRC Press, 2019.

[106] S. Mendez, A. Berod, C. Chnafa, M. Garreau, E. Gibaud, A. Larroque, S. Lindsey, M. Martins Afonso, P. Matteoli, R. Mendez Rojano, D. Midou, T. Puiseux, J. Sigüenza, P. Taraconat, V. Zmijanovic, and F. Nicoud. *YALES2BIO: A General Purpose Solver Dedicated to Blood Flows in Biological Flow in Large Vessels: Dialog Between Numerical Modeling and In Vitro/In Vivo Experiments ; Eds V. Deplano, J.-M. Fullana and C. Verdier ; Sciences—Mechanics—Biomechanics,*, chapter 7, pages 183–206. John Wiley & Sons, 2022.

[107] S. Mendez, E. Gibaud, and F. Nicoud. An unstructured solver for simulations of deformable particles in flows at arbitrary Reynolds numbers. *Journal of Computational Physics*, 256(1):465–483, 2014.

[108] T. Mignon and S. Mendez. A theoretical investigation of the frisbee motion of red blood cells in shear flow. *Mathematical Modelling of Natural Phenomena*, 16:23, 2021.

[109] J. P. Mills, L. Qie, M. Dao, C. T. Lim, and S. Suresh. Nonlinear elastic and viscoelastic deformation of the human red blood cell with optical tweezers. *Mechanics & Chemistry of Biosystems*, 1(3):169–180, 2004.

[110] C. Minetti, V. Audemar, T. Podgorski, and G. Coupier. Dynamics of a large population of red blood cells under shear flow. *Journal of Fluid Mechanics*, 864:408–448, 2019.

[111] N. Mohandas and P. G. Gallagher. Red cell membrane: past, present, and future. *Blood*, 112(10):3939–3948, 2008.

[112] K. Monkos. Viscometric study of human, bovine, equine and ovine haemoglobin in aqueous solution. *International Journal of Biological Macromolecules*, 16:31–35, 1994.

[113] K. Monkos and B. Turczynski. Determination of the axial ratio of globular proteins in aqueous solution using viscometric measurements. *International Journal of Biological Macromolecules*, 1991.

[114] V. Moureau, P. Domingo, and L. Vervisch. Design of a massively parallel CFD code for complex geometries. *Comptes Rendus Mécanique*, 339(2-3):141–148, 2011.

[115] M. Musielak. Red blood cell-deformability measurement: Review of techniques. *Clinical Hemorheology and Microcirculation*, 42, 2009.

[116] E. Nader, C. Nougier, C. Boisson, S. Poutrel, J. Catella, F. Martin, J. Charvet, S. Girard, S. Havard-Guibert, M. Martin, H. Rezigue, H. Desmurs-Clavel, C. Renoux, P. Joly, N. Guillot, Y. Bertrand, A. Hot, Y. Dargaud, and P. Connes. Increased blood viscosity and red blood cell aggregation in patients with covid-19. *American Journal of Hematology*, 97(3):283–292, 2022.

[117] V. Narsimhan, H. Zhao, and E. S. G. Shaqfeh. Coarse-grained theory to predict the concentration distribution of red blood cells in wall-bounded Couette flow at zero Reynolds number. *Physics of Fluids*, 25(061901), 2013.

[118] H. Noguchi and G. Gompper. Dynamics of fluid vesicles in shear flow: Effect of membrane viscosity and thermal fluctuations. *Physical Review E*, 72(011901), 2005.

[119] T. J. Ober, S. J. Haward, C. J. Pipe, J. Soulages, and G. H. Mckinley. Microfluidic extensional rheometry using a hyperbolic contraction geometry. *Rheologica Acta*, 2013.

[120] N. L. Parrow, P. C. Violet, H. Tu, J. Nichols, C. A. Pittman, C. Fitzhugh, R. E. Fleming, N. Mohandas, J. F. Tisdale, and M. Levine. Measuring deformability and red cell heterogeneity in blood by ektacytometry. *Journal of Visualized Experiments*, 2018.

[121] Z. Peng, R. J. Asaro, and Q. Zhu. Multiscale simulation of erythrocyte membranes. *Physical Review E*, 81(031904), 2010.

[122] Z. Peng, R. J. Asaro, and Q. Zhu. Multiscale modelling of erythrocytes in Stokes flow. *Journal of Fluid Mechanics*, 686:299–337, 2011.

[123] Z. Peng, X. Li, I. V. Pivkin, M. Dao, G. E. Karniadakis, and S. Suresh. Lipid bilayer and cytoskeletal interactions in a red blood cell. *Proceedings of the National Academy of Sciences USA*, 110(33):13356–13361, 2013.

[124] Z. Peng, A. Mashayekh, and Q. Zhu. Erythrocyte responses in low-shear-rate flows: effects of non-biconcave stress-free state in the cytoskeleton. *Journal of Fluid Mechanics*, 742:96–118, 2014.

[125] Z. Peng, S. Salehyar, and Q. Zhu. Stability of the tank treading modes of erythrocytes and its dependence on cytoskeleton reference states. *Journal of Fluid Mechanics*, 771:449–467, 2015.

[126] Z. Peng and Q. Zhu. Deformation of the erythrocyte cytoskeleton in tank treading motions. *Soft Matter*, 9, 2013.

[127] A. Perazzo, Z. Peng, Y. N. Young, Z. Feng, D. K. Wood, J. M. Higgins, and H. A. Stone. The effect of rigid cells on blood viscosity: linking rheology and sickle cell anemia. *Soft Matter*, 18:554–565, 2022.

[128] C. S. Peskin. Numerical analysis of blood flow in the heart. *Journal of Computational Physics*, 25:220–252, 1977.

[129] C. S. Peskin. The immersed boundary method. *Acta Numerica*, 11:479–517, 2002.

[130] C. Pfaferott, G. B. Nash, and H. J. Meiselman. Red blood cell deformation in shear flow. effects of internal and external phase viscosity and of in vivo aging. *Biophysical Journal*, 47:695–704, 1985.

[131] A. Pinelli, I. Z. Naqavi, U. Piomelli, and J. Favier. Immersed-boundary methods for general finite-difference and finite-volume Navier–Stokes solvers. *Journal of Computational Physics*, 229:9073–9091, 2010.

[132] S. Piomelli and C. Seaman. Mechanism of red blood cell aging: Relationship of cell density and cell age. *American Journal of Hematology*, 42:46–52, 1993.

[133] I. V. Pivkin and G. E. Karniadakis. Accurate coarse-grained modeling of red blood cells. *Physical Review Letters*, 101(118105), 2008.

[134] I. V. Pivkin, Z. Peng, G. E. Karniadakis, P. Buffet, M. Dao, and S. Suresh. Biomechanics of red blood cells in human spleen and consequences for physiology and disease. *Proceedings of the National Academy of Sciences USA*, 113(28):7804–7809, 2016.

[135] M. Puig-de Morales-Marinkovic, K. T. Turner, J. P. Butler, J. J. Fredberg, and S. Suresh. Viscoelasticity of the human red blood cell. *American Journal of Physiology*, 293:597–605, April 2007.

[136] D. A. Reasor, J. R. Clausen, and C. K. Aidun. Rheological characterization of cellular blood in shear. *Journal of Fluid Mechanics*, 726:497–516, 2013.

[137] D. A. Reasor, M. Mehrabadi, D. N. Ku, and C. K. Aidun. Determination of critical parameters in platelet margination. *Annals of Biomedical Engineering*, 41(2):238–249, 2013.

[138] C. Renoux, M. Faivre, A. Bessaa, L. Da Costa, P. Joly, A. Gauthier, and P. Connes. Impact of surface-area-to-volume ratio, internal viscosity and membrane viscoelasticity on red blood cell deformability measured in isotonic condition. *Scientific Reports*, 9(6771):1–7, 2019.

[139] A. M. Roma, C. S. Peskin, and M. J. Berger. An adaptive version of the immersed boundary method. *Journal of Computational Physics*, 153:509–534, 1999.

[140] S. Roman, A. Merlo, P. Duru, F. Risso, and S. Lorthois. Going beyond 20 μm-sized channels for studying red blood cell phase separation in microfluidic bifurcations. *Biomicrofluidics*, 10(034103), 2016.

[141] L. S. S., Y. Yim, K. H. Ahn, and S. J. Lee. Extensional flow-based assessment of red blood cell deformability using hyperbolic converging microchannel. *Biomedical Microdevices*, 11, 2009.

[142] A. Saadat, C. J. Guido, and E. S. G. Shaqfeh. Effect of cytoplasmic viscosity on red blood cell migration in small arteriole-level confinements. *bioRxiv*, 2019.

[143] U. Seifert. Configurations of fluid membranes and vesicles. *Advances in Physics*, 46(1):13–137, 1997.

[144] S. Shrivastava and J. Tang. Large deformation finite element analysis of non-linear viscoelastic membranes with reference to thermoforming. *The Journal of Strain Analysis for Engineering Design*, 28(1):31–51, 1993.

[145] J. Sigüenza, S. Mendez, D. Ambard, F. Dubois, F. Jourdan, R. Mozul, and F. Nicoud. Validation of an immersed thick boundary method for simulating fluid-structure interactions of deformable membranes. *Journal of Computational Physics*, 322:723–746, 2016.

[146] J. Sigüenza, S. Mendez, and F. Nicoud. How should the optical tweezers experiment be used to characterize the red blood cell membrane mechanics? *Biomechanics and Modeling in Mechanobiology*, 16:1645–1657, 2017.

[147] J. C. Simo. On a fully three-dimensional finite-strain viscoelastic damage model: Formulation and computational aspects. *Computer Methods in Applied Mechanics and Engineering*, 60:153–173, 1987.

[148] J. C. Simo and K. S. Pister. Remarks on rate constitutive equations for finite deformation problems: computational implications. *Computer Methods in Applied Mechanics and Engineering*, 46:201–215, 1984.

[149] R. Skalak, A. Tozeren, R. P. Zarda, and S. Chien. Strain energy function of red blood cell membranes. *Biophysical Journal*, 13:245–264, 1973.

[150] J. M. Skotheim and T. W. Secomb. Red blood cells and other nonspherical capsules in shear flow: Oscillatory dynamics and the tank-treading-to-tumbling transition. *Physical Review Letters*, 98(078301), 2007.

[151] G. K. Snyder and B. A. Sheafor. Red blood cells: Centerpiece in the evolution of the vertebrate circulatory system. *American Zoologist*, 39(2):189–198, 1995.

[152] A. H. Swihart, J. M. Mikrut, J. B. Ketterson, and R. C. Macdonald. Atomic force microscopy of the erythrocyte membrane skeleton. *Journal of Microscopy*, 204(3), 2001.

[153] P. Taraconat, J.-P. Gineys, D. Isèbe, F. Nicoud, and S. Mendez. Numerical simulation of deformable particles in a Coulter counter. *International Journal for Numerical Methods in Biomedical Engineering*, 35(11):e3243, 2019.

[154] P. Taraconat, S. Mendez, and F. Nicoud. *Application of numerical simulation for a better characterization of red blood cells by impedence measurement.* PhD thesis, 2020.

[155] R. Tran-Son-Tay, S. P. Sutera, and P. R. Rao. Determination of red blood cell membrane viscosity from rheoscopic observations of tank-treading motion. *Biophysical Journal*, 46:65–72, 1984.

[156] S. O. Unverdi and G. Tryggvason. A front-tracking method for viscous, incompressible, multi-fluid flows. *Journal of Computational Physics*, 100:25–37, 1992.

[157] A.-C. S. Vogt, T. Arsiwala, M. Mohsen, M. Vogel, V. Manolova, and M. F. Bachmann. On iron metabolism and its regulation. *International Journal of Molecular Sciences*, 22(9), 2021.

[158] F. L. A. Willekens. *Erythrocyte vesiculation a survival strategy.* 2010.

[159] U. Windberger, A. Bartholovitsch, R. Plasenzotti, K. J. Korak, and G. Heinze. Whole blood viscosity, plasma viscosity and erythrocyte aggre-

gation in nine mammalian species: reference values and comparison of data. *Experimental Physiology*, 88(3):431–440, 2003.

[160] A. Z. K. Yazdani and P. Bagchi. Phase diagram and breathing dynamics of a single red blood cell and a biconcave capsule in dilute shear flow. *Physical Review E*, 84(026314), 2011.

[161] A. Z. K. Yazdani and P. Bagchi. Three-dimensional numerical simulation of vesicle dynamics using a front-tracking method. *Physical Review E*, 85(056308), 2012.

[162] A. Z. K. Yazdani and P. Bagchi. Influence of membrane viscosity on capsule dynamics in shear flow. *Journal of Fluid Mechanics*, 718:569–595, 2013.

[163] A. Z. K. Yazdani, R. M. Kalluri, and P. Bagchi. Tank-treading and tumbling frequencies of capsules and red blood cells. *Physical Review E*, 83(046305), 2011.

[164] R. P. Zarda, S. Chien, and R. Skalak. Elastic deformations of red blood cells. *Journal of Biomechanics*, 10:211–221, 1977.

[165] J. Zhang, P. C. Johnson, and A. S. Popel. Effects of erythrocyte deformability and aggregation on the cell free layer and apparent viscosity of microscopic blood flows. *Microvascular Research*, 77:265–272, 2009.

[166] H. Zhao, E. S. G. Shaqfeh, and V. Narsimhan. Shear-induced particle migration and margination in a cellular suspension. *Physics of Fluids*, 24(011902):1–21, 2012.

[167] O. Y. Zhong-can and W. Helfrich. Bending energy of vesicle membranes: General expressions for the first, second, and third variation of the shape energy and applications to spheres and cylinders. *Physical Review A*, 39(10):5280–5288, 1989.

Abstract

The red blood cell (RBC) is the most common cell in vertebrates. It has many vital functions for the body, the main one being the transport of oxygen to different organs and of carbon dioxide back to the lungs. The gas exchanges taking place in the smallest vessels of the body, the way the RBCs deform plays an essential role in most of the functions they have to play. Indeed, RBCs have sometimes to undergo extreme deformations. An example is the passage of RBCs in the spleen, where cells that cannot pass through micrometric slits are eliminated by the macrophages. This deformability testing imposed by the body shows its importance for the circulation. There are also many pathologies that alter this deformability. This is the case of malaria, sickle cell disease or spherocytosis, to name a few. This motivates to understand how RBCs deform under flow and what alterations of the RBC deformability imply. Over the last years, numerical simulations has been developed to support those investigations.

Among the characteristics observed experimentally and which are not traditionally taken into account in simulations, there is the membrane viscoelasticty. Membrane viscosity is associated with internal dissipation of the membrane during its deformation. This phenomenon has however been observed since the 70s, by performing micropipette tests and noticeable differences in some simulations compared to experiments were attributed to the lack of membrane viscosity in the RBC models. These elements motivated this work. This thesis therefore aims at implementing a viscosity model in an existing inviscid RBC model as well as to study the impact of membrane viscosity on behaviors of the RBC under flow.

In this manuscript, the physical framework as well as the numerical framework are detailed. A finite-strain version of a generalized Maxwell model is used to represent the effect of membrane viscosity in the simulations. The implementation and validation of the chosen model are presented before moving on to two application cases. The first application concerns the study of the impact of viscosity on the tank-treading behavior of GRs. This work has indeed highlighted the strong impact of membrane viscosity on the tank-treading behavior of GR. It also made it possible to show a possible reproduction of the experimental results by imposing a taylored shear-thinning behavior for the membrane viscosity, a hypothesis already present in the literature. The second study concerns the design of a flow experiment dedicated to measuring the viscous behavior of the RBC membrane. This is the study of the elongation of blood cells in a cross flow device. This work highlights the significant impact of membrane viscosity on the behavior of RBCs in this type of device. This thesis demonstrates the essential role of membrane viscosity in RBC dynamics and opens new questions about the relevant modeling of membrane dissipation.

Keywords : red blood cell, Computational Fluid Dynamics, Continuum mechanics, Immersed Boundary Method, viscoelasticity, fluid-structure interactions.

Résumé

Le globule rouge (GR) est la cellule la plus présente chez les vertébrés. Elle assure de nombreuses fonctions vitales pour l'organisme, la plus essentielle étant le transport de l'oxygène jusqu'aux différents organes. Pour remplir ce rôle, les GRs doivent se déformer pour passer dans des vaisseaux plus petits que leur taille au repos. L'organisme teste même la déformabilité des GRs dans la rate, où les globules ne pouvant pas passer au travers de fentes micrométriques sont éliminés par les macrophages. Ainsi, la déformabilité des GRs est un aspect essentiel de leur fonction et de nombreuses pathologies altèrent cette déformabilité. C'est le cas de la malaria, de la drépanocytose ou encore de la sphérocytose, pour n'en nommer que quelques unes. Bien comprendre les caractéristiques de cette déformabilité et comment les pathologies peuvent l'altérer est essentiel dans l'étude de la circulation sanguine. Depuis quelques années, la simulation numérique de la dynamique des globules rouges a permis de contribuer à cet effort de recherche.

Toutefois, parmi les comportements observés expérimentalement et qui n'est généralement pas pris en compte dans les simulations, il y a la viscoélasticité de la membrane, due à la dissipation interne de la membrane lors de sa déformation. La viscoélasticité de la membrane a été montrée dès les années 70, grâce à des essais de micropipette. Des différences notables entre certaines simulations et des expériences ont été attribuées à l'absence de viscosité de membrane dans les modèles de GR. Ces éléments ont motivé ce travail : cette thèse a pour but l'implémentation d'un modèle de viscosité dans un modèle de GR non-visqueux existant ainsi que l'étude de l'impact de la viscosité de membrane sur certains comportements du GR en écoulement.

Pour ce faire, le cadre physique ainsi que le cadre numérique sont détaillés. Ensuite, l'implémentation et la validation du modèle choisi sont présentées avant de passer à deux cas d'application. La première application concerne l'étude de l'impact de la viscosité sur le comportement en tank-treading des GRs. Ce travail a permis la mise en lumière du fort impact de la viscosité de membrane sur le comportement en tank-treading du GR. Elle a également permis de montrer que la simulation peut reproduire les résultats expérimentaux en imposant un modèle de membrane rhéofluidifiante, hypothèse déjà formulée dans la littérature. La seconde étude concerne la conception d'une expérience en flux dédié à la mesure du comportement visqueux de la membrane des GRs. Il s'agit de l'étude de l'élongation des globules dans un dispositif d'écoulement en croix. Ce travail permis de mettre en lumière l'impact important de la viscosité de membrane sur le comportement des GRs dans ce type de dispositif.

Mots-clefs : Globule rouge, Mécanique des fluides numériques, Mécanique des milieux continus, Méthode des Frontières Immergées, viscoélasticité, interactions fluide-structure.